DESIGN & ANALYSIS OF A PARALLELIZED ELECTRICALLY CONTROLLED DROPLET GENERATING DEVICE

DESIGN & ANALYSIS OF A PARALLELIZED ELECTRICALLY CONTROLLED DROPLET GENERATING DEVICE

By
CHAO ZHU, B.ENG.
B. Eng. (University of Science and Technology of China, Anhui, China)

A Thesis
Submitted to the School of Graduate Studies
In Partial Fulfillment of the Requirements
For the Degree
Master of Applied Science

McMaster University

MASTER OF APPLIED SCIENCE (2013) McMaster University

(Mechanical Engineering) Hamilton, Ontario, Canada

TITLE DESIGN & ANALYSIS OF PARALLELIZED ELECTRICALLY A CONTROL DROPLET GENERATING DEVICE

AUTHOR CHAO ZHU, B.Eng.

SUPERVISOR Professor P. R. Selvaganapathy

Department of Mechanical Engineering

NUMBER OF PAGES XII, 107

Abstract

Microdroplets find use in a variety of applications ranging from chemical synthesis to biological analysis. However, commercial use of microdroplets has been stymied in many applications, as current devices lack one or more of the critical features such as precise and dynamic control of the droplet size, high throughput and easy fabrication. This work involves design, fabrication and characterization of a microdroplet generating device that uses low cost fabrication, allows dynamic control of the droplet size and achieves parallelized droplet generation for high throughput.

Dynamic droplet size control by DC electric field has been demonstrated with the device. By varying the potential from 300 V to 1000 V, the droplet size can change from 140 μm to around 40 μm. The transition of the droplet size just takes few seconds. Parallelized droplet generation has also been demonstrated. The standard deviation of the droplet size is lower than 4% for the three-capillary device and lower than 6% for the five-capillary device under different operating conditions. Highest throughput of 0.75 mL/hour is achieved on the five-capillary device. It has been show that this proposed device has a better performance than the existing PDMS based parallel droplet generating devices. A theoretical model of the droplet generating process has also been developed which is able to predict the droplet size at various potentials. The theoretical results are in good agreement with experimental ones.

Acknowledgments

Foremost, I would like to express my sincere gratitude to my supervisor, Dr. P. Ravi Selvaganapathy, for giving me the opportunity to be involved in such an interesting topic of research and studying abroad. I would like to thank him for his patience, enthusiasm and continuous support of my research. Dr. Ravi is a great mentor to me in both the research and my life and I will be benefited from what he taught me in the rest of my life. Next, I would like to thank Dr. C. Y. Ching for his critical comments and suggestion, as well as his optimism and great sense of humour that encouraged me to defeat the difficulties I had ever encountered.

I thank my fellow labmates in Center for Advanced Micro-Electro-Fluidics laboratory: Wen-I Wu, Pouya Rezai, Leo Hsu and Bo Dang for the stimulating discussions and invaluable assistances. Shehad, Ali, Peter, Siawash, Reza and Russel for inspiring me to get new ideas of research. Asma and Rana, these two ladies successfully enhance the efficiency of our lab. Thank Jun and Beichen for their great sense of humour. All these memories have already become great fortune in my life and I will never forget my two-year colourful life in Canada.

I would also like to thank my girlfriend Yujie Zhu, her love supports me to overcome many difficult times this year. Her great talent in research and sense of arts have brought me lots of brand new views of the world.

Last but not least, I would like to thank my parents for their love, support, encouragement and advice. You are always there for me, and I am forever in your debt.

Table of Contents

List of Figures

Chapter 1 Motivation & Organization

1.1 Motivation

Microdroplets have various applications ranging from biological analysis to chemical synthesis. Usually microdroplets are used in applications that require a large number of combinatorial experiments and need to be performed with small volumes of expensive reagents or samples. Alternatively, they are also used to perform reactions that are efficient but dangerous to perform in the macroscale. These applications depend on the monodisperse droplet generating ability of the droplet generating devices. Numerous techniques have been developed to generate microdroplets especially using microfabricated structures that allow precise positioning of two different phases in close proximity with each other. Many mature technologies such as flow focusing device [1], T-shape droplet generating chip [2] and Edge-Based technique [3], have already been proposed and carefully characterized. However, most of the devices gain control of the droplet size by varying the ratio between the dispersed phase flow rate and the continuous phase flow rate, resulting in a slow and imprecise control of the droplet size. Although some of the designs have demonstrated the possibility of electrically control, sufficient characterization has not been done. Moreover, electrically control has been applied only to single capillary devices and this technique has not been parallelized. The existing parallelization method for droplet generation involves complicated design of the channels and expensive fabrication process. To solve the existing problems, a device allowing electrically control of the parallelized droplet generation fabricated with inexpensive techniques, has been proposed in this research.

1.2 Organization

The organization of the thesis is outlined as follows:

Chapter 2 provides an introduction to the physics and the application of microfluidics. Theoretical principles related to the droplet generation have been introduced. Various microdroplet generating methods are also reviewed and their applications are discussed.

Chapter 3 deals with the working principles and the design of the device in our research. Several physics models related to this specific device are discussed in detail. In the design process, several iterations of the design are discussed and multiphysics simulations are used to improve the design.

Chapter 4 outlines the materials and microfabrication techniques that have been applied in our research. Moreover, the fabrication process and assembly techniques are fully introduced.

Chapter 5 details the results obtained in the experiments. Graphs and figures are presented and carefully explained by proposed theories and literatures. Experimental results are compared with the theoretical results. The influences of different parameters are characterized in detail.

Chapter 6 concludes our work and highlights the contributions that have been made. Several possible future research directions related to this device have been proposed.

Chapter 2 Introduction

2.1 Applications of Microfluidics and Microdroplets

Microfluidics is a rapidly emerging research area that deals with picoliter or nanoliter volume of liquid [4]. Although microfluidic devices have been investigated since the 1950s, it is only over the past 20 years that significant research development has been made in this field. The primary area of interest has been in the development of diagnostics devices where the entire unit operations performed in a lab is integrated onto a single chip [5][6]. These integrated systems are often referred to as 'Micro-Total-Analysis System' or 'lab on a chip' [7]. These microfluidics chips have a wide range of applications such as drug screening, chemical synthesis and biomedical diagnostics [7][8][9]. More recently, droplet based microfluidics has emerged as an alternative to continuous flow devices for handling micro/nanoscale volumes of samples and reagents [10]. Several applications of droplet are presented below.

2.1.1 Droplet Based PCR

One of the biggest applications of droplet based techniques is automating biochemical analysis by DNA amplification through Polymerase Chain Reaction (PCR) [11][12][13]. Performing PCR in droplets (**Figure 2.1**) allows compartmentalization which enables isolation and amplification of even rare sequences occurring at lower concentrations than others [14]. Droplet digital PCR (ddPCR) is already a mature technique that has been commercialized by Bio-Rad Inc. In this system, the droplets are generated in a microfluidic device to obtain thousands of monodispersed microdroplets each containing a small amount of the sample along with the amplification reagents, as shown in **Figure 2.1**. Then the PCR thermo-cycling and the

imaging are performed in a separate device. Alternatively, in other methods such as the slide chip and SD chip, the microdroplets of the sample and reagents are formed in small compartments on two different chips that are physically placed or slid together to mix the contents. Then the thermo-cycling and the imaging are performed in-situ [15].

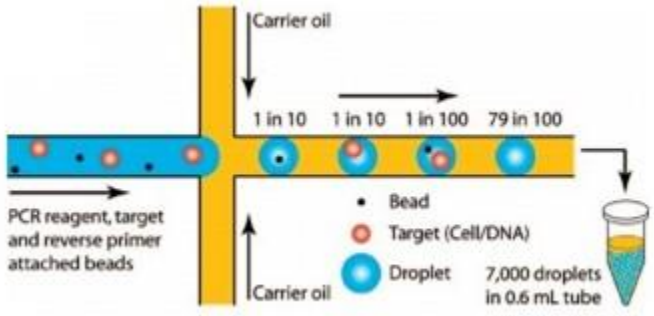

Figure 2.1: *Schematic of Droplet Based PCR* [13]

2.1.2 Chemical Synthesis

One of the defining features of the droplet is the internal flow circulation due to the surface tension effects. This internal circulation can cause effective and fast mixing at the microscale that has been exploited to perform fast and homogenous chemical synthesis. Droplet-based microfluidic techniques are ideal for chemical synthesis, particularly in situations where mixing has to happen fast (~ ms time frame) such as when the reaction time is fast or a precise residence time is required [16]. In addition, droplet methods also allow precise control of the reactant volume. For instance, Kesselman et al. [17] demonstrated the usefulness of applying microdroplet generating method to generate monodispersed homogeneous microgels from Carboxymethyl Cellulose (CMC A) & Aldehyde-Functionalized Dextran (DEX B). By varying the flow rate ratio, they showed that the size of microgels can change from 150 μm to 40 μm. The highest throughput of 0.08 mL/hour was achieved. Moreover, long-term (24 hours)

functioning of the device was demonstrated to collect sufficient amount of microgels for an experimental study on drug release.

2.1.3 Protein Crystallization

Determining the right conditions and solvent compositions for crystallization of a new protein is difficult and is typically a trial and error process. Numerous parameters such as pH, salt concentration, protein concentration and temperature all can influence the crystallization of that particular protein. Currently, a multi-well array integrated with large expensive robotic liquid handling machine is used to screen thousands of unique conditions combinatorial to determine the right condition for crystallization. More recently, droplet-based techniques have been investigated for combinatorial analysis of protein crystallization conditions due to their low volume consumption, fast dynamic response and low cost. Zheng et al. [18][19] (**Figure 2.2**) were able to use just a few nanoliters of protein solution to screen thousands of conditions by using microdroplet platform. The condition of crystallization can be changed combinatorially by continuously changing the solution's flow rate. Long-term storage could be achieved by transferring droplets from PDMS channel into a glass capillary.

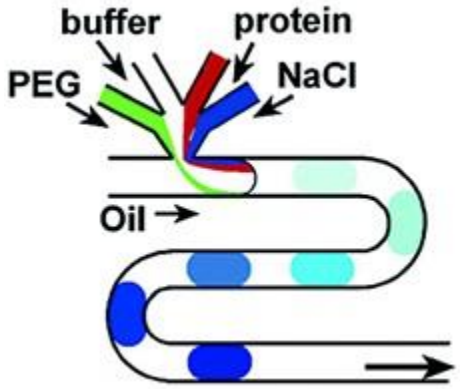

Figure 2.2: *Droplet based protein crystallization* [20]

2.2 Formation of Microdroplets

All these applications require the formation of monodispersed microdroplets and the control of their size/volume in a precise manner. The formation of droplets can be explained by a simple everyday example. When a stream of fluid falls down from a faucet, it would finally break into droplets instead of maintaining a stream shape.

Why would it break into droplets rather than remain as a stream? This question is not an easy one to answer. More than 100 years ago, Lord Rayleigh [21] addressed this problem by performing a series of experiments and arriving at a theoretical understanding of the phenomena. He posited that the droplet formation is the result of instability of the stream. Initially, the surface tension holds the liquid and a stream forms. As the liquid stream is elongated by other external forces (e.g. gravity, shearing force), the surface energy increases, resulting in the increasing instability of the liquid stream which is now known as "Plateau-Rayleigh Instability". Any tiny perturbations will cause a resultant pressure gradient inside the stream due to the effect of surface tension forces. The pressure, in return, provides a positive feedback and enlarges the perturbation which leads to droplet formation. Detailed mathematical and dimensionless analysis [22] gives the following relationship:

$$\frac{L_c}{R} \sim U\left(\frac{\rho R}{\gamma}\right)^{\frac{1}{2}} \tag{2-1}$$

This equation shows that the critical length L_c is related to the jet radius R, jet velocity U, liquid density ρ and surface tensionγ.

Rayleigh's theory successfully describes the droplet generation mechanism in macro scale under the influence of gravity. Microscale droplets are usually generated by non-gravitational methods, in which the two immiscible fluids such as water and oil are brought

together to form an interface in microfluidic device, thus artificially introducing perturbations in it.

To further investigate the physics involved in microscale droplet generation, several dimensionless numbers are introduced and analyzed.

The Reynolds number [23] is a frequently used dimensionless number in fluid mechanics which compares the inertial force and viscous force. It is defined as

$$Re = \frac{\rho V L}{\mu} \tag{2-2}$$

Where ρ represents the density of fluid; V is fluid velocity; L is the characteristic length of the channel and μ is the dynamic viscosity of the fluid. Equation 2-2 indicates that as the scale decreases, *Re* also decreases. In microfluidic devices, *Re* is much smaller than 1, indicating that the inertial force is as influential as in the macroscale. Moreover, low *Re* also indicates that the flow is laminar in the microfluidic devices.

The ratio between the two dominant forces in the microscale (viscous force and surface tension) is represented by the Capillary number [24]:

$$Ca = \frac{\mu V}{\gamma} \tag{2-3}$$

Where μ represents the dynamic viscosity of the more viscous fluid in two phase flow system; V is the fluid velocity and γ is the interfacial tension. Since it includes the two dominant forces, *Ca* is an important dimensionless number in microdroplet generating devices. The interfacial tension dominates the flow at low *Ca* ($Ca < 1$) and the viscous force dominates at high *Ca* ($Ca >> 1$). When interfacial tension dominates, the spherical droplets form while when viscous force dominates, the droplet deforms according to the profile of the viscous forces. Although droplets

are generated in both the regimes, the mode of the droplet generating process and the sizes of the droplets vary according to the *Ca* [25].

The Bond number [26], is defined as:

$$Bo = \frac{\Delta\rho g L^2}{\gamma} \tag{2-4}$$

Where $\Delta\rho$ represents the difference between density of two fluids; g is the gravity acceleration; L is the characteristic length and γ is the interfacial tension. *Bo* compares the gravitational force and surface tension. A small Bond number (*Bo* << 1) indicates that the gravitational force is as compared to the gravitational forces in determining the state of the flow.

The Weber number, which is the ratio between inertia and surface tension, is defined as:

$$We = \frac{\rho V^2 L}{\gamma} \tag{2-5}$$

Where $\Delta\rho$ represents the density of the fluids; V is the fluid velocity; L is the characteristic length and γ is the interfacial tension.

Similar to *Re, We* also decreases with the decrease of the dimension, indicating that surface tension dominates inertial force in these situations [23].

2.3 Droplet Generating Techniques

Numerous droplet generating techniques have been developed. In this section, several frequently used methods are discussed in detail and their comparison with our device is presented.

2.3.1 Flow Focusing

One of the most frequently used methods is called flow focusing droplet generation [15]. It is typically observed in a microfluidic device with a co-flow geometry (**Figure 2.3A**). In this

geometry, an interface is created between two (dispersed and continuous) phases when they flowed together. The velocity difference between the two phases introduces viscous drag forces parallel to the interface. The net drag force carries the droplet away from the nozzle while the surface tension force holds it back. When the drag force becomes large enough, the droplet can be ejected. In flow focusing, an orifice is placed ahead of the region where the liquids co-flow, which squeezes the continuous flow along with the dispersed flow forming a stream (**Figure 2.3B**). This nozzle geometry produces an instability that leads to breakup of the stream into droplets (**Figure 2.4**). By adjusting the ratio between the flow rates of two phases, the effective control over droplet size can be achieved in flow focusing geometry. However, due to the fluidic capacitances in the system and the extremely low flow rates, it takes long time for flow focusing devices to respond to the change of flow rate ratio, making this method unsuitable for dynamic control of droplet sizes [17].

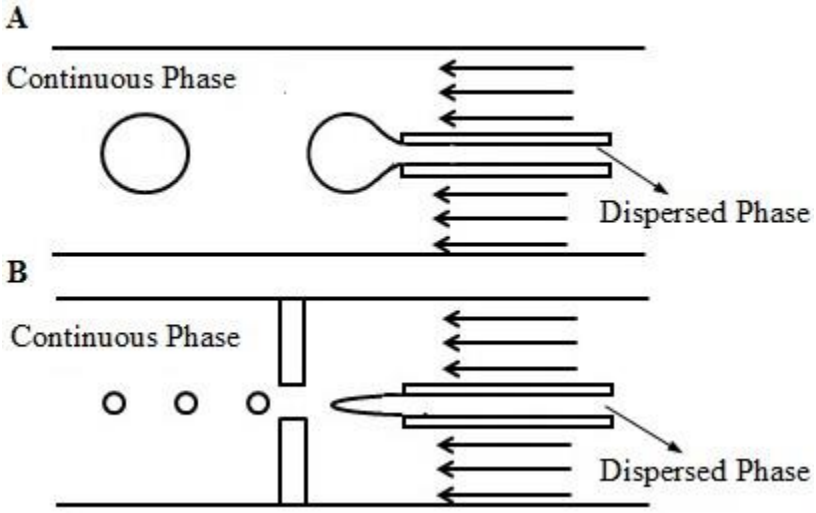

Figure 2.3: *Schematic of A) Co-flow; B) Flow focusing*

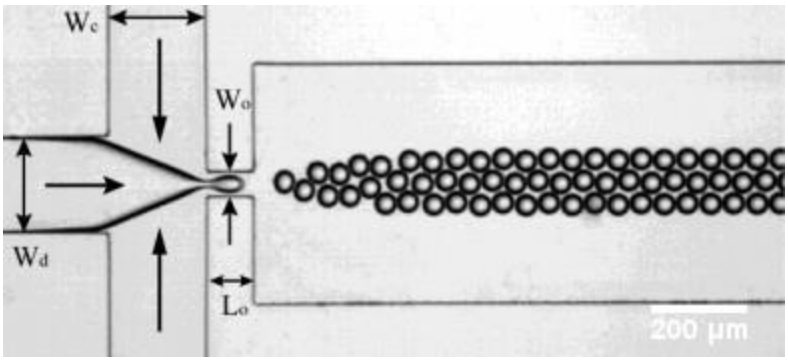

Figure 2.4: *Flow focusing droplet generation* [10]

The first microfluidic flow focusing device was developed by Anna et al. [1]. It is a simple 2D planar structure with the central channel for dispersed phase and two opposing side channels for continuous phase. She was able to generate droplet size of ~ 100s nm using an orifice width of 10 μm, although with large polydispersity. The throughput of this device is ~ 0.1 mL/hour.

As illustrated in **Figure 2.5**, three distinct droplet generating regimes have been identified on flow focusing devices, which are squeezing, dripping and jetting. In the squeezing regime showed in **Figure 2.5A**, the droplet blocks the orifice and it is pinched off by the buildup pressure from the upstream. In the dripping regime (**Figure 2.5B**), the orifice is partially blocked and the droplet generating process depends on both the buildup pressure and the shearing from the continuous flow. The jetting regime occurs only at a high continuous flow rate. As the interface between two phases being elongated through the orifice (**Figure 2.5C**), the droplets pinch off at the tip of the stream far from the orifice, of which the sizes are the smallest among three regimes. The increase of the flow rate ratio between the continuous and the dispersed phase, leads to change in the generation mode changes from squeezing to jetting [27]. Besides flow rate ratio, a number of parameters can influence the droplet generating regimes in flow focusing devices. Previous research found that *Ca* number, *We* number and diameter of the orifice [28]

has a great influence in the transition between squeezing and jetting modes. Moreover, the surface wettability of the channel [29], the effect of fluid viscosity [30] and the difference of pressure in two phases [31] also shown to have some influence. Due to the complexity of droplet generating process, the mechanism in flow focusing device is still not fully understood.

In order to improve the control over the droplet size, more sophisticated fabrication methods have been applied to fabricate 3D nozzles with circular orifice. In this case, the droplet size becomes more sensitive to the flow parameters since a larger surface of the dispersed flow was exposed to the shearing force in such 3D geometry [32][33]. The droplet size as low as 20 μm can be obtained with high monodispersity and the throughput of the device is ~ 0.1 mL/hour [32]. Flow focusing devices have also been parallelized to obtain higher throughput. However, parallelization makes the devices more expensive to produce and increases the coefficient of variation on the droplet sizes due to reduced controllability [34][35][36].

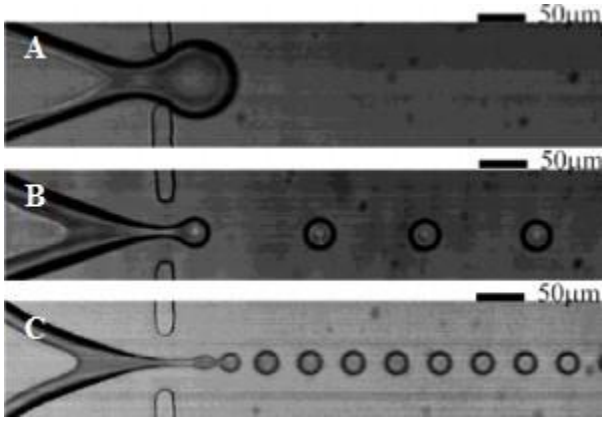

Figure 2.5: *Working regime of flow focusing device* [27]*: A) Squeezing; B) Dripping; C) Jetting*

2.3.2 T-junction Droplet Generation

T-junction is another popular geometry to generate droplets between two immiscible fluids. It was first demonstrated by Thorsen et al. [37] in 2001. In this geometry, the dispersed

phase channel intersects with the continuous phase channel at 90^{o}, and the structure of the channel has the shape similar to the letter "T" (**Figure 2.6**). Similar to co-flow device, the shearing force (asymmetric in this case) and the subsequent pressure gradient will elongate the dispersed phase and break it into droplets.

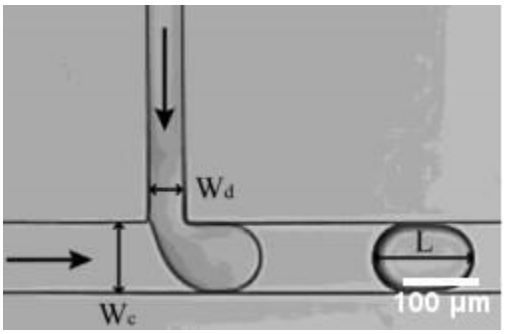

Figure 2.6: *T-junction droplet generation* [10]

The droplet size control can be achieved by varying the flow rate ratio of two phases [38]. Similar to flow-focusing devices, the droplet generation can be classified as squeezing regime, dripping regime and jetting regime [39]. In squeezing regime, the droplet generating process relies on the buildup pressure caused by the emerging droplet of dispersed phase blocking the continuous phase channel. Once the force caused by the buildup pressure becomes greater than that caused by surface tension, a droplet pinches off. In the dripping regime, the droplet generating process relies on both of buildup pressure and the shearing force from the continuous phases. Jetting occurs at a very high flow rate of continuous flow that is not common in the T-junction droplet generating device. Liu and Zhang [40] investigated the influence of *Ca* on the transition of flow regime, revealing that the droplet generation would transit from squeezing mode to dripping mode as *Ca* increases. The dispersed flow plugs the full width of main channel when $Ca = 0.006$ (squeezing), while it plugs only part of the main channel when *Ca* increases to 0.056 (dripping). Garstecki et al. [41] proposed the scaling law of droplet size in squeezing

regime, indicating that the droplet size depends increases with the increase of dispersed flow rate of as well as the increase of dispersed channel width. Besides, numerous research has been done to theoretically and experimentally characterize the influence of the channel wettability [42], the channel dimension [43], the viscosity of the fluid [38], the surface tension [44] and the concentration of the surfactants [45] on the droplet generation in T-junctions. Parallelization has been achieved to produce droplets up to 7.4 kHz frequency via more sophisticated fabrication techniques [34][46].

2.3.3 Edge Based Droplet Generation

Edge based droplet generation is a novel method for droplet generation with high throughput which combines a T-Junction and a geometric plateau (**Figure 2.7A**). The dispersed phase (oil) is squeezed through a very shallow plateau (~ 2 μm) and then flowed into the deep continuous phase (water) channel (~ 200 μm) at 90^{o}. The droplets are generated at the edge of the plateau due to the difference in pressure encountered as the droplet emerges [3] (**Figure 2.7B**). This technique was first demonstrated by K.C.Dijke [47]. The major advantage for EDGE based droplet generation is that the droplets will be generated all along the edge of the plateau. By increasing the length of the plateau or adding more droplet formation units (DFU) into the device, the droplet generating frequency of 10 kHz was reached. However, the droplet size of the edge based device is fixed and only depends on the depth of shallow plateau. Empirical relation of $d = 6h$ was obtained where d is the diameter of droplet and h is the depth of the plateau. Therefore, it is impossible to have dynamic control the droplet size. Moreover, the fabrication cost is high due to the material (silicon) and the fabrication method (DRIE) used.

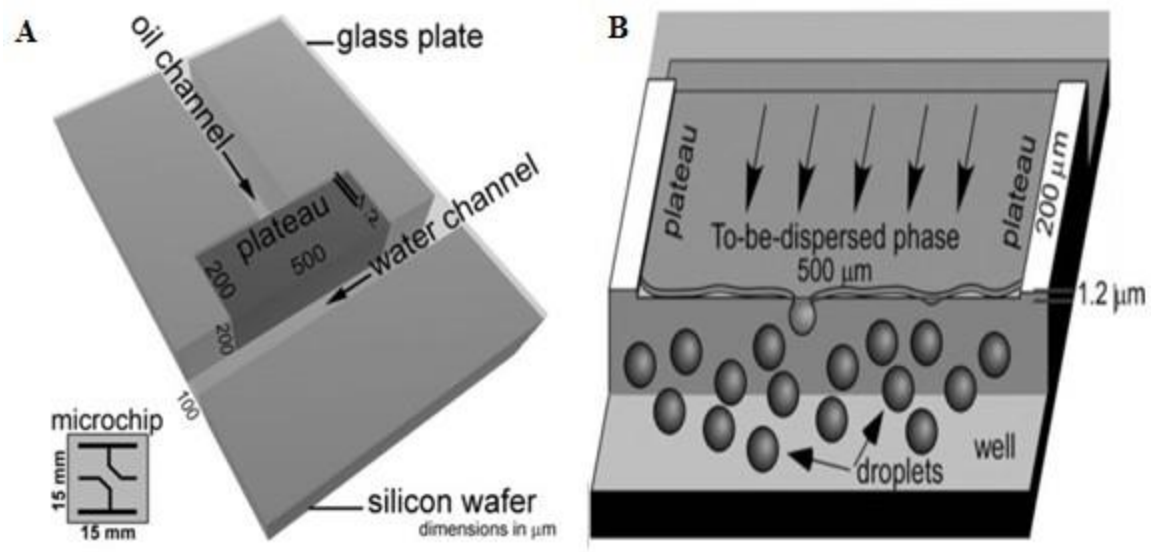

Figure 2.7: *A) Geometry of edge based droplet generating device; B) Schematic of single DFU of edge based droplet generation* [3][48]

2.3.4 Dynamic Control of Droplet Size

To increase the controllability in droplet generating devices, external active elements were introduced, including: electric field, thermal control and pneumatic valves.

The electric field is a commonly used method for dynamic droplet size control in the microdroplet generating devices. By integrating dielectric coated electrodes underneath the channel of flow focusing device at the nozzle region, Gu et al. [49][50] demonstrated electro-wetting based droplet size control. In this method, the contact angle between Oil/Water interface and the channel at the nozzle region can be adjusted by changing the applied potential of the electrode. The transition of droplet generating regime from dripping to jetting is achieved by increasing the potential at the same flow rate. It can also decrease the generated droplet size down to few microns in flow focusing device.

Alternatively, Kim et al. [51], Say et al. [52] and Siawash et al. [53] introduced the use of electrostatic force as a method for dynamic control of droplet size. With one electrode installed in the dispersed phase and the other electrode placed in the continuous phase, a potential applied

to the device generates an electric field on the dielectric phases and introduces an electrostatic force at the interface of two fluids. The electrostatic force assists the drag force to pull the droplet away from the tip of the nozzle, reducing the droplet size at the same flow rate. If the potential is increased further, the Taylor-Cone forms at the tip of nozzle and electro-spray is observed, generating extremely fine droplets (~ 1 μm). Kim et al. [51] characterized the relation between DC potential, flow rate ratio and droplet size in detail. With a flow rate ratio of 5/350, the droplet size decrease from 12 μm to less than 1 μm as the potential increased to 2000 V. However, with a higher flow ratio of 80/350, the increase of the potential has little influence on droplet size. This device is functioned by using DC potential. Siawash et al. [53] improved Kim's et al. [51] design by investigating the relation between droplet size and DC pulses. By adjusting the potential, frequency and the duration of the pulse, the droplet size decreased down to few microns. Moreover, he characterized the steady working regime of the device. Say et al. [52] investigated the droplet generation in AC potential. The droplet size decreased from 80 μm to 30 μm as potential increased to 1000 V while the frequency has little effect on droplet size. The controllability of electric field decreases as flow rate ratio increases.

Membrane valves were also used in a flow focusing device to change the orifice size in order to achieve the control of droplet size. This technique was first demonstrated by Abate et al. [54]. The droplet size decreases from 40 μm to 24 μm and the frequency increases from 1 kHz to 3 kHz as the valve being gradually actuated.

Heat has also been used as a variable in the dynamic control of droplet size. The surface tension and viscosity of the liquid vary with the temperature. Therefore, the control of the droplet can be achieved by changing the temperature of fluid. It has been demonstrated by Murshed et al. [55] that a micro-heater and micro-sensor integrated with the T-junction can dynamically control

droplet generation by adjusting the temperature. With the increase of the temperature from 25 ℃ to 38 ℃, the droplet size increased by 86%. The controllability was dependent on the depth of the channel. The droplet size increases 86% in the device with the channel height of 30 μm while only increases 14% in the device with the channel height of 300 μm. Temperature control can also be applied to flow-focusing device. The increase of temperature changes the droplet generating mechanism from dripping to squeezing. This can be explained by the decrease of *Ca* due to the dependency of viscosity and surface tension to the temperature.

2.3.5 Summary of Droplet Generating Techniques

Table 2.1: Summary of droplet generating techniques

Method	Droplet Size Range	Productivity/Frequency	Control Method	Fabrication Expense
Flow Focusing [1][27][32]	~ 300 nm – 50 μm	~ 0.1 mL/hour	Flow Rate Ratio (Slow Response)	Low
T Junction Droplet Generation [2][56]	> 50 μm	0.1-1 mL/hour	Flow Rate Ratio (Slow Response)	Low
PDMS Based Parallelized Flow Focusing [35][36]	> 40 μm	0.3 – 0.5 mL/hour	Flow Rate Ratio (Slow Response)	Low
Electrically Controlled Droplet Generation [51][52][53]	10 μm – 150 μm	~ 0.1 mL/hour	Electric Field (Fast Response)	Low
Temperature Controlled Droplet Generation [55]	> 80 μm	~ 0.1 mL/hour	Temperature (Fast Response)	High
Membrane Controlled Droplet Generation [54]	24 μm – 40 μm	0.2 – 0.5 mL/hour	Orifice Width (Fast Response)	Low
EDGE Based Droplet Generation [48][57]	7 μm – 15 μm	~ 1 kHz/Unit	Height of the Plateau (No control)	High

A summary of the various droplet generating devices and the techniques for dynamic control of droplet sizes is shown in **Table 2.1**. Based on this summary, none of these devices can achieve active control of parallelized droplet generation with low fabrication cost. High throughput parallelized droplet generating device that is also dynamically controllable is needed to significantly extend the use of microfuidic devices in the applications outlined. Design and development of such a device made using simple fabrication process is the focus of this research.

2.4 Summary

This chapter introduced the principles of droplet formation in microfluidic devices. Applications of microfluidics and microdroplets were discussed. Dimensionless numbers that are important in droplet generating process were carefully explained. Furthermore, several droplet generating methods were presented and their characteristics were discussed in detail. Control techniques for dynamic control of droplet size, including electrically control, temperature control and membrane control were illustrated and discussed. The comparisons among existing techniques from several perspectives were made.

Chapter 3 Device Design and Working Principle

3.1 Introduction

In the previous chapter, various kinds of droplet generating techniques were introduced and their working characteristics were discussed in detail. The objective of the research was also determined, which is to design and fabricate a high throughput device that can achieve dynamic control of droplet size. In this chapter the working principle of such a device and its design process are detailed. A physical model the droplet ejection dynamics is developed and various forces acting on the droplet are evaluated. Characterization using multi-physics simulation software is also performed to optimize the design of the device.

3.2 Working Principle

3.2.1 Overview

The working principle of co-flow droplet generating devices was discussed in previous chapter. Briefly, the interface between the dispersed and continuous phase was elongated by shear force between the dispersed and continuous flow. When the Rayleigh instability criterion was met, the interface broke up and formed droplets. Droplet size was controlled by varying the ratio between the dispersed flow rate and the continuous flow rate in such devices. However, due to the slow response of the device to the change of flow rate, a long time was required for the droplets to transition from one size to another, leading to lower productivity and a waste of large

amount of both fluids. Several methods [51][54][55] were proposed to address this issue, of which the use of electric field for dynamical control of droplet size was found to be the most reliable. By introducing electro-static force into the co-flow droplet generating process, the dynamic control of the droplet size can be achieved taking advantage of the fast response of the electrostatic force to changes in the electric field. Typically in the absence of the electric field, the drag force due to the flow of the continuous phase has to overcome the surface tension force of the dispersed phase at the capillary for a droplet to be generated. When an electric field is applied, the electrostatic force aids the drag force and enables the droplets to form faster. For a better illustration of this phenomena, consider a device consisting of a microcapillary in a larger fluid channel. The dispersed phase (DI water + dye) is flowed in the microcapillary and the continuous phase (Oil) is flowed in the larger channel (**Figure 3.1**) so that the droplets can be produced. Also consider the scenario when the dispersed phase is connected to the positive potential and another microelectrode embedded in the channel downstream of the capillary tip is grounded. This potential generates an electric field that will impose an electrostatic force, pulling the polarized charges on the droplet away from the capillary and thus aiding droplet formation. In the next few sections, the forces that influence the droplet formation processed are discussed.

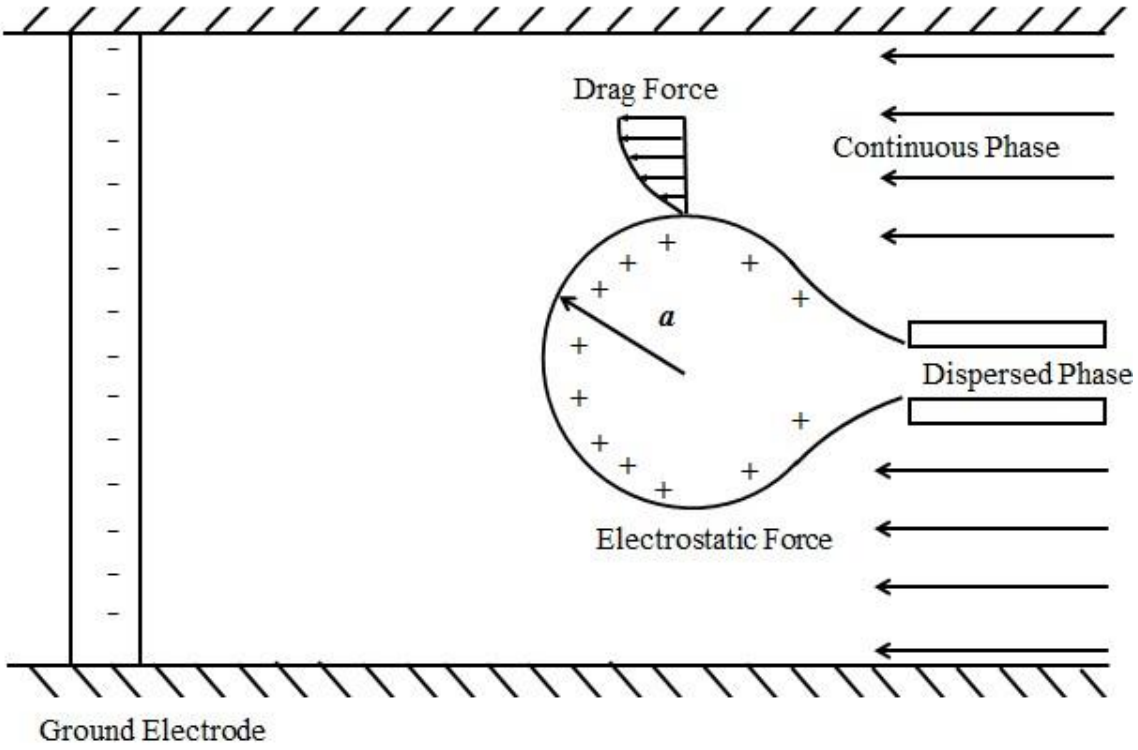

Figure 3.1: *lustration of droplet generation under the influence of both viscous and electrostatic forces*

3.2.2 Capillary Force & Interfacial Tension

In the droplet generating process, capillary force is the only force that prevents the droplet from detaching from the capillary. It is the overall effect of interfacial tension around the capillary tip. The interfacial tension is due the uneven cohesion of molecules at the interface of two phases and becomes a significant influence at the micro/nanoscale over other forces such as gravity. As illustrated in **Figure 3.2**, the neck of the dispersed phase is almost in the horizontal direction and the capillary force can be therefore calculated as [15] :

$$F_c = \gamma \pi D \tag{3-1}$$

Where γ represents the interfacial tension between DI water and oil, D is the inner diameter of the capillary tubing. As observed in Equation 3-1, F_c is proportional to both the interfacial tension and inner diameter of the capillary tubing but independent of the droplet size.

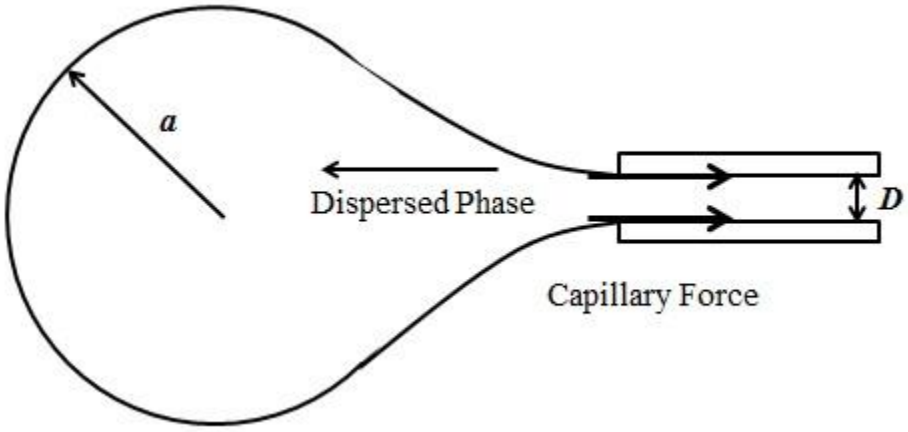

Figure 3.2: *Schematic of resultant capillary force*

3.2.3 Drag Force

In fluid dynamics, drag force refers to the resistance force that acts on the static object in a moving fluid or vice versa, and is in the opposite direction to relative velocity. Due to the velocity difference, a steep velocity gradient is established at the interface resulting in friction and interfacial momentum transfer that causes the drag force. In the droplet generating process in a co-flow device, the droplet can be considered as a sphere when it is close to detachment from the tip of capillary (**Figure 3.3**). In this scenario, approximate solution of Stokes-Flow model can be applied if the *Re* << 1which is the case of microfluidic devices.

In the approximate solution [58], the drag force acting on a unit area of droplet surface can be calculated using::

$$\sigma = \frac{3\mu U}{2a} \tag{3-2}$$

Therefore, the total drag force acting on the droplet is:

$$F_d = A\sigma = 4\pi a^2 \frac{3\mu U}{2a} = 6\pi a\mu V \quad (3\text{-}3)$$

Where "a" is the radius of droplet, μ is the dynamic viscosity and V is the velocity of continuous flow. A linear relation exists between the drag force and the flow velocity of continuous flow. To increase the drag force, velocity of the continuous flow has to be increased accordingly.

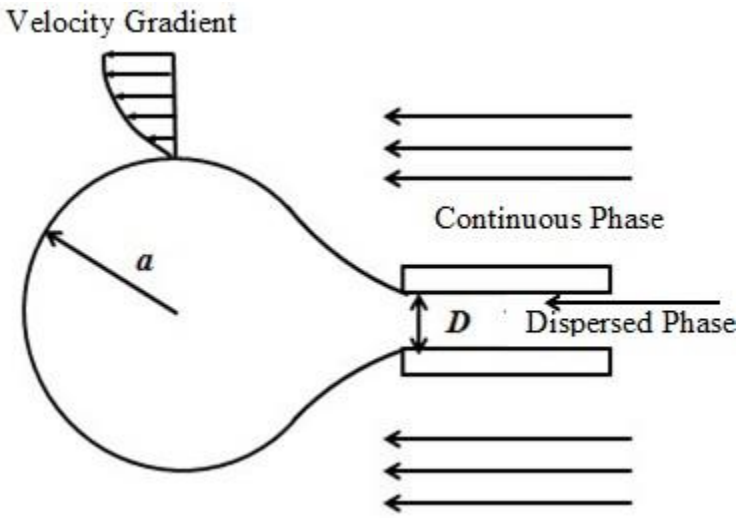

Figure 3.3: *Schematic of the cause of the drag force*

3.2.4 Electrostatic Force

When the electric field is applied to the device, the fluid at the tip of the capillary becomes charged and the concentration of charges is the highest at the very extreme of the droplet that is in close proximity to the other electrode as shown (**Figure 3.4**). The rest of the droplet surface is also charged but in a charging much lower density.

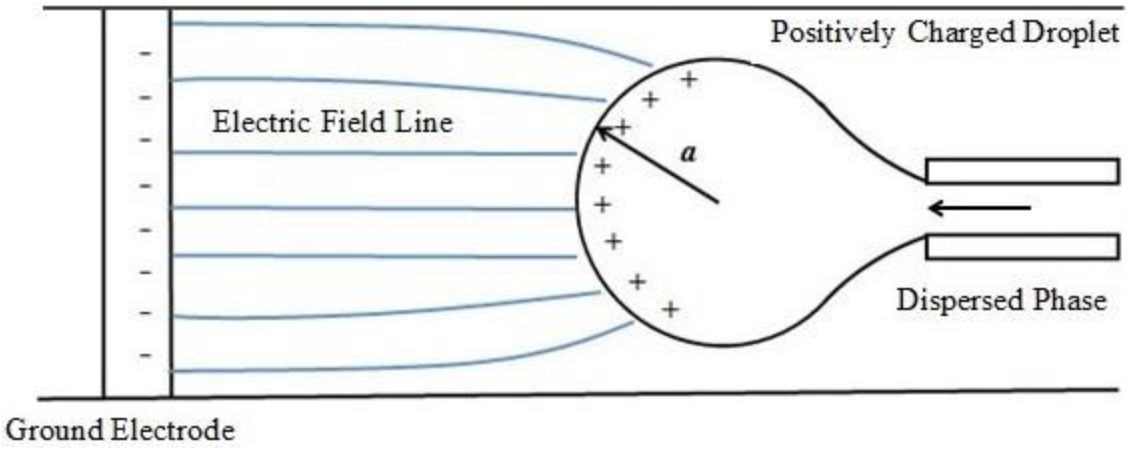

Figure 3.4: *Illustration of electric field distribution between a droplet at higher potential and ground*

The electrostatic pressure can be determined by the following equation proposed by Wright et al. [59]:

$$P_e = \frac{\varepsilon E_n^2}{2} \tag{3-4}$$

Where P_e is the electrostatic pressure, ε is the permittivity of the continuous flow, and E_n is the electric field normal to the meniscus surface. Assuming the uniform electric field intensity at the front surface of the droplet, the electrostatic force can be obtained by:

$$F_e = P_e S = \frac{\varepsilon E_n^2}{2} \pi a^2 \tag{3-5}$$

Where F_e is electrostatic force and a is the radius of droplet. The electrostatic force has a quadratic dependence on the intensity of electric field. Compared to the flow velocity, the droplet generating process is more sensitive to the intensity of electric field.

Based on above discussions, the droplet radius a in an electrically controlled co-flow droplet generating device can be predicted by the following equation:

$$\frac{\varepsilon E_n^2}{2} \pi a^2 + 6\pi a \mu V = \gamma \pi D \tag{3-6}$$

The droplet size obtained from this equation will be compared with experimental results in Chapter 5.

3.3 Device Design & Iteration

3.3.1 Schematic of Design

In this section, the design of a microfluidic device to achieve electrically controlled parallel W/O (Water in Oil) droplet generation is detailed. The basic design of the device is shown in **Figure 3.5** and consists of three main parts: the channel for continuous (oil) phase, the channel for dispersed (water) phase and the substrate with electrode. The microcapillaries, which are selected as the channels for dispersed phase, are inserted into the continuous (oil) channel through the grooves fabricated in it. In this design, the dispersed phase channels (microcapillaries) are suspended in the center of the continuous (oil) phase channel. Therefore, the droplets do not come in contact with the walls of the continuous (oil) phase channel when they are being generated. This is unique compared to other microfabrication designs and will improve the stability of the droplet generating process [32]. Moreover, the fabrication process needed for this design is simpler compared to other parallel microfluidic droplet generating devices [34][57]. The parallelization here is easily achieved by simply inserting and aligning more microcapillaries into the oil channel. Two linear electrodes are fabricated on the glass substrates to ensure the uniformity of the electric field. The detailed design process for each of the components will be described in following sections.

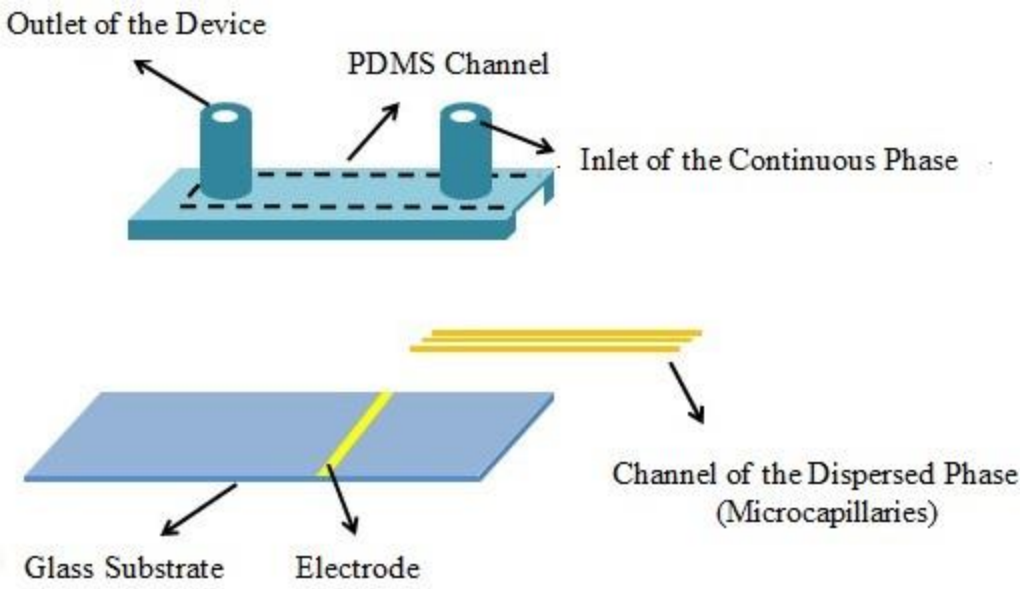

Figure 3.5: *Schematic of the design*

3.3.2 Design of the Channels

As previously discussed, the design involving the insertion of microcapillaries into the oil channel was selected, due to its simplicity as well as the ease of parallelization. Moreover, Siawash et al. [53] has already demonstrated that it is a suitable design for electrical droplet generation using pulsed electric field. A commercial microcapillary with a 150 μm outer diameter (OD) and a 20 μm inner diameter (ID) was selected as the channel for water phase. Previous research [17] showed that the size of the generated droplets has the same order of magnitude with the nozzle dimension. Therefore, in order to produce droplets with diameters from 40 μm to 150 μm, capillary with 20 μm ID was selected out of all the commercially available sizes. The OD of 150 μm was selected because it was the most suitable size for manual installation and alignment.

The oil channel (**Figure 3.6A**) is designed as a straight PDMS channel with grooves (**Figure 3.6B**) on one end. The cross section of the grooves is $150\ \mu m \times 150\ \mu m$ which allows easy insertion and fixation of microcapillaries (**Figure 3.6C**).

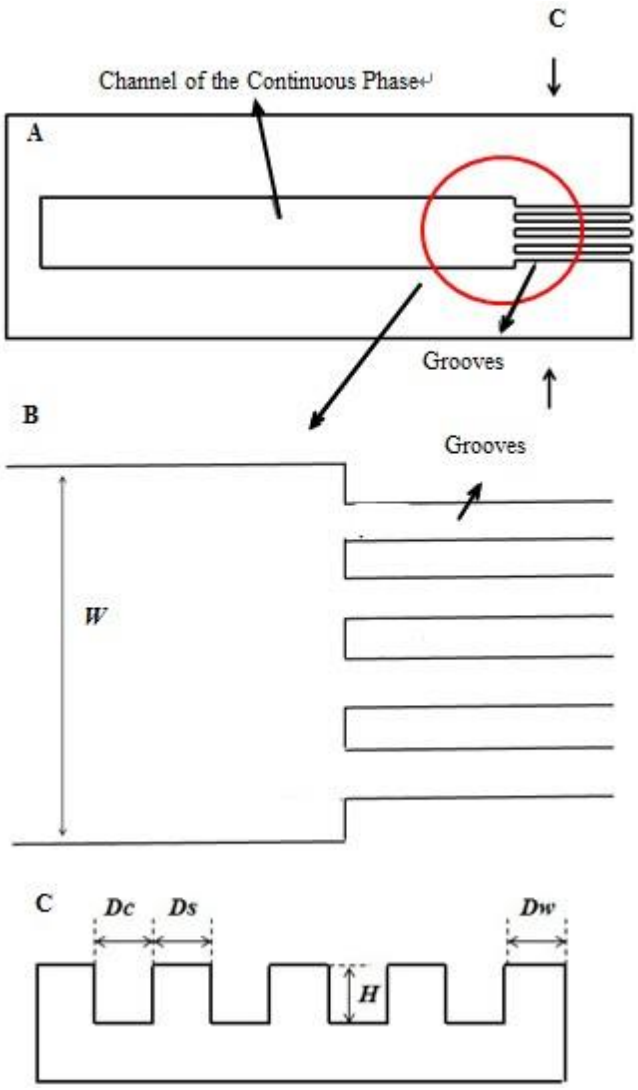

Figure 3.6: *Schematic of PDMS channel with groove: A) Top view; B) View of the grooves; C) Cross-section view*

Once inserted into the oil channel, the microcapillaries should be equally spaced to ensure the uniformity of the flow field around the tip of the capillaries, for producing monodispersed droplets. Since the positions of the capillaries are fixed by the grooves, the width of the continuous (oil) phase channel is dependent on following relation:

$$W = N * D_c + (N - 1) * D_s + 2 * D_w \quad (3\text{-}7)$$

Where N is the number of grooves replicated on the channel, D_c is the width of grooves, D_s is the space between adjacent grooves and D_w is the distance between side grooves and the edge of the channel.

A channel with N grooves can accommodate no more than N capillaries, and the separation distance between adjacent capillaries is set as D_s. When fabricating the device, if D_s < 100 μm, the alignment becomes difficult and the adjacent capillaries interact with each other. When D_s > 200 μm, the device becomes less compact and will cause a waste of continuous (oil) phase. To optimize these two aspects, D_s and D_w are set as 150 μm. In case of a device with 5 grooves, the width of the channel is then calculated as 1650 μm .

The silicone tubing with an inner diameter of 1.6 mm is used as the inlet of the continuous phase since it has similar dimension to the microchannel with 5 grooves (1.65 mm). This will ensure the more uniform inflow of the oil. In addition, the inlet was placed at a distance of ~ 1.6 cm from the tip of the capillaries to prevent the entrance effects of the flow from influencing the droplet generating process. Previous research [60] showed the flow with low *Re* number, the relation between entrance distance and inlet dimension is L/D ~ 10 (**Figure 3.7**).

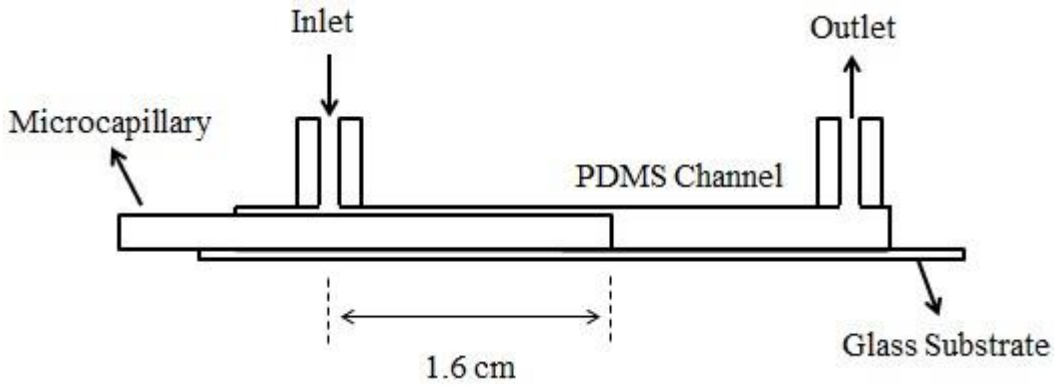

Figure 3.7: *Side view of the design*

3.3.3 Configurations of the Electrodes

Ensuring the uniformity of the electric field at various capillary tips is an important criterion in an electrically controlled parallelized droplet generating device. In this section, several configurations of the electrodes will be evaluated by multi-physics simulation, in order to select the optimal design.

In previous research, Kim et al. [51] and Siawash et al. [53] connected conductive dispersed phase liquid to the positive, and inserted the ground electrode manually into the channel of continuous flow close to the nozzle. Although it is simple to fabricate, this design is not appropriate for parallelization due to the lack of precision in both the geometry and the positioning of the electrode. Gu et al. [50] and Say et al. [52] adopted a microfabrication approach to fabricate the electrode, which improved the precision of electrode placement and consequently the electric field distribution. Here we use microfabricated gold electrodes on glass slide for its easy fabrication and high accuracy. Designs include two different electrode configurations as shown in **Figure 3.8**.

In the first electrode configuration, the microfabricated linear electrode is set as ground while the capillary with the conductive dispersed phase (DI Water + 1% Methylene Blue) is connected to the positive electrode. Once potential is applied, a diverging electric field profile is formed between the tip of capillary and the ground. This geometry is called "point to plane electrode configuration" (**Figure 3.8A**). In the second electrode configuration, another linear microfabricated electrode is introduced beneath the capillaries, and is also set as positive. The modification in the second electrode configuration ensures a more uniform electric field distribution in the continuous phase and was used to study its influence on the droplet size in the generating process. This geometry is called "parallel electrode configuration" (**Figure 3.8B**).

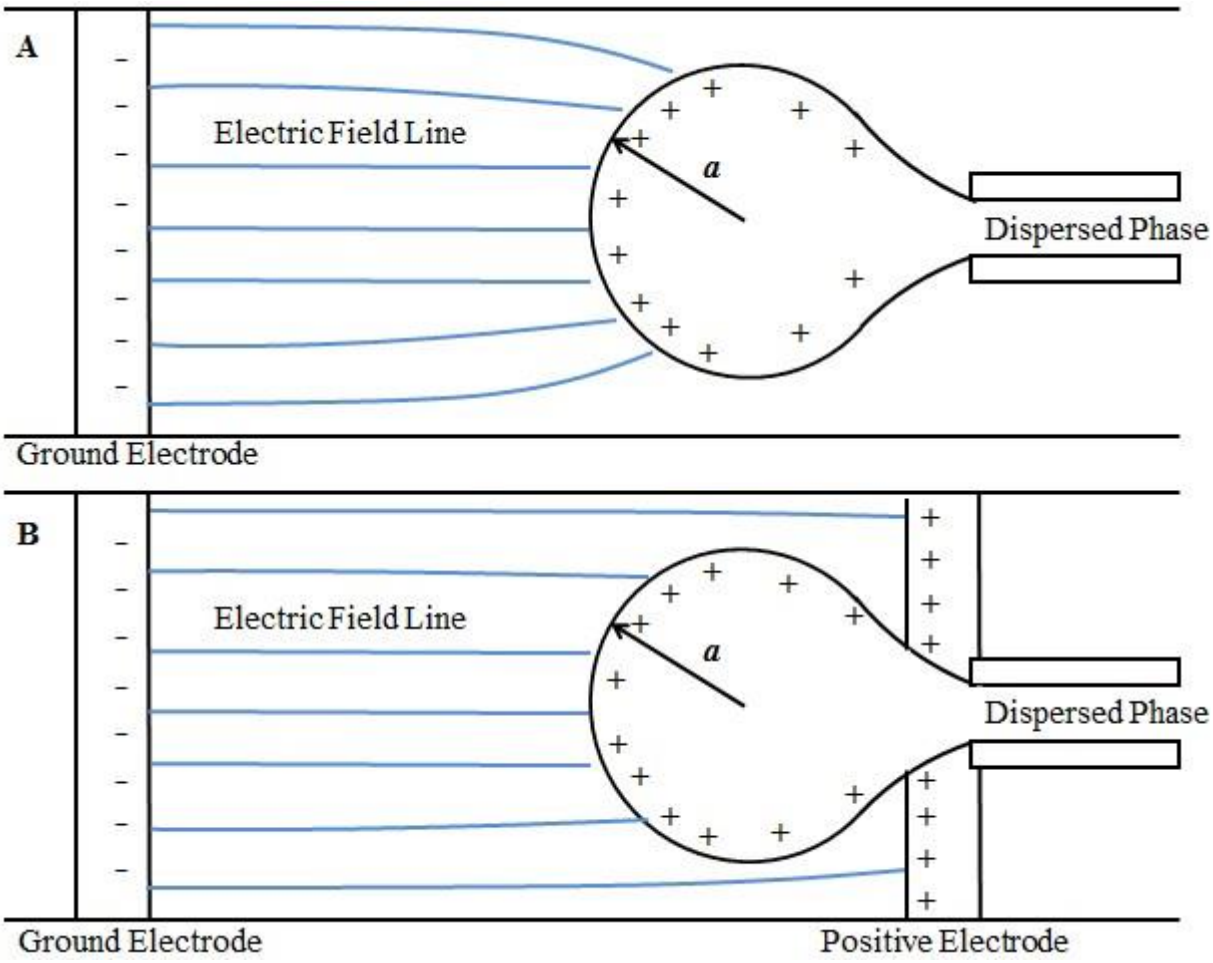

Figure 3.8: *A) Point to plane electrode configuration; B) Parallel electrode configuration*

Considering the electric field distribution close to the ground electrode in the dielectric oil medium, the regions adjacent to the edge of electrodes have a higher density of electric field lines than on its top surface. Consequently, the width of the ground electrode is not a crucial factor in determining the electric field distribution in the continuous phase. The width of electrode is then set as 250 μm for the ease of fabrication. The electric field distribution is more uniform in the second design. In previous work [51][53], the distance between the ground electrode and the interface of the fluid ranged from 0.375 mm to 2 mm. Considering the dimension of our channel, the distance between the electrodes is set as 1 mm.

3.3.3.1 Numerical Simulation

To evaluate the performance of the two designs of electrode configuration, multi-physics simulation was performed to determine the electric field distribution in the continuous phase. Devices with three and five parallel capillaries were simulated for two electrode configurations. The simulated geometries are illustrated in **Figure 3.9**.

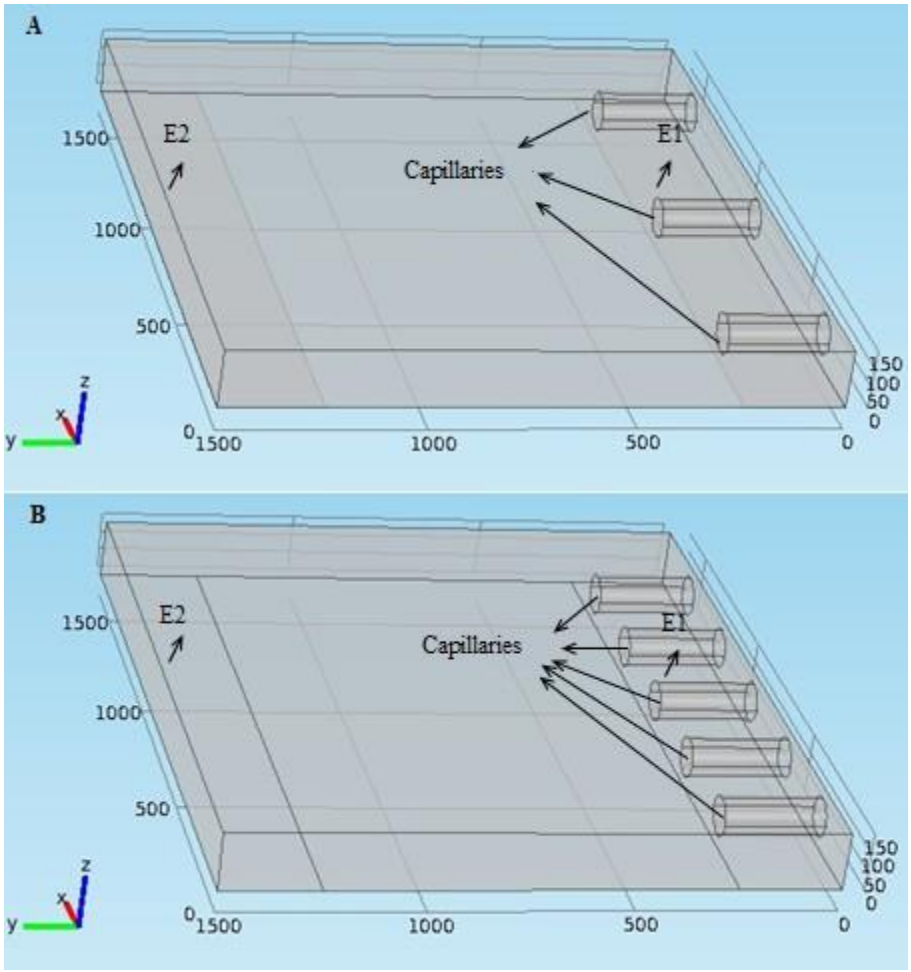

Figure 3.9: *Simulating geometry for: A) Three-capillary device; B) Five-capillary device*

The boundary conditions are set as follows. For the parallel electrode configuration, the Dirichlet boundary conditions are set to the surface E1 (planar electrode), the surface E2 (planar electrode) and the cross section of the capillaries, with the potential at E2 being set to 0 V (U = 0

V) and the potentials at E1 and capillary cross sections being set to 300 V, 600 V and 900 V. All the other surfaces are set to the Neumann boundary conditions and the potential gradient is zero ($\frac{\partial U}{\partial n} = 0$). Moreover, the charge on all boundaries is set to zero ($\rho = 0$). For the point to plane electrode configuration, the Dirichlet boundary conditions are just set to the surface E2 (planar electrode) and the cross section of the capillaries. All the other surfaces are set to the Neumann boundary conditions and the potential gradient is zero ($\frac{\partial U}{\partial n} = 0$), which is similar to the parallel electrode configuration. The charge conservation assumption is made for the whole domain. The governing equations of the simulation are illustrated:

$$\mathrm{E} = -\nabla \mathrm{U} \tag{3-8}$$

$$\nabla \cdot \mathrm{D} = \rho \tag{3-9}$$

$$\mathrm{D} = \varepsilon_0 \varepsilon_e E \tag{3-10}$$

Where E is the electric field; D is the electric displacement field; U is the potential; ε_0 is the absolute permittivity (8.85×10^{-12} F/m) and ε_e is the relative permittivity (2.2 for paraffin oil). More details about the simulation are presented in Appendix B. The simulation is proven to be mesh independence in Appendix C and demonstrated to be geometry independence in Appendix D.

The overall electric field distribution at the central plane (illustrated in **Figure 3.10**, z = 75 μm) of the device is illustrated in **Figure 3.11**. In case of the point to plane electrode configuration, the electric field diverges from the capillary into the continuous phase. The effect of this divergence is stark in the regions in between the capillaries as can be seen in **Figure 3.11A**. In case of the parallel electrode configuration, the uniformity of the electric field

direction has been significantly improved as a consequence of the introduction of microfabricated electrodes underneath the capillaries which renders the electric field in the bulk of the fluid more uniform (**Figure 3.11B**).

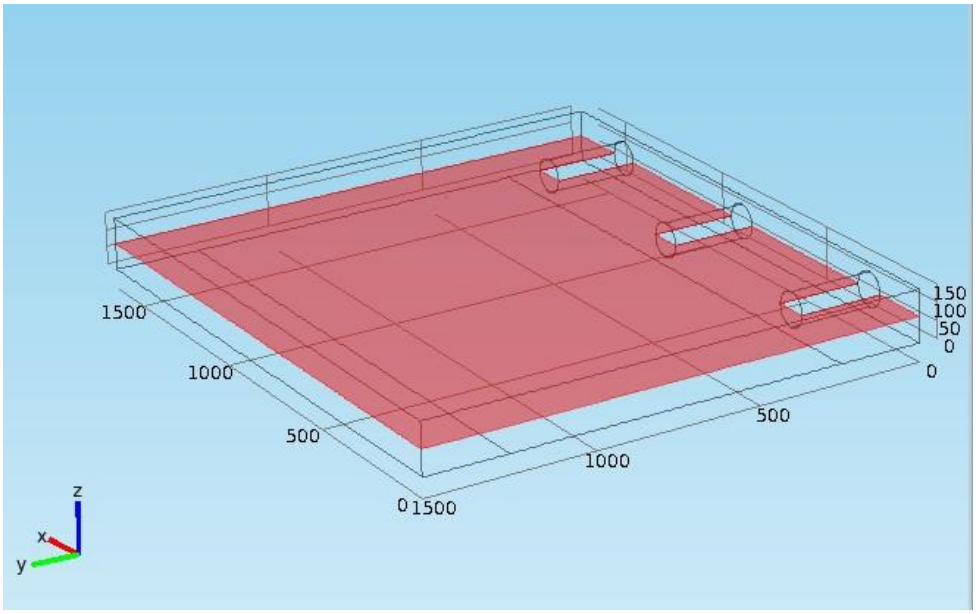

Figure 3.10: *Central plane of the three-capillary device*

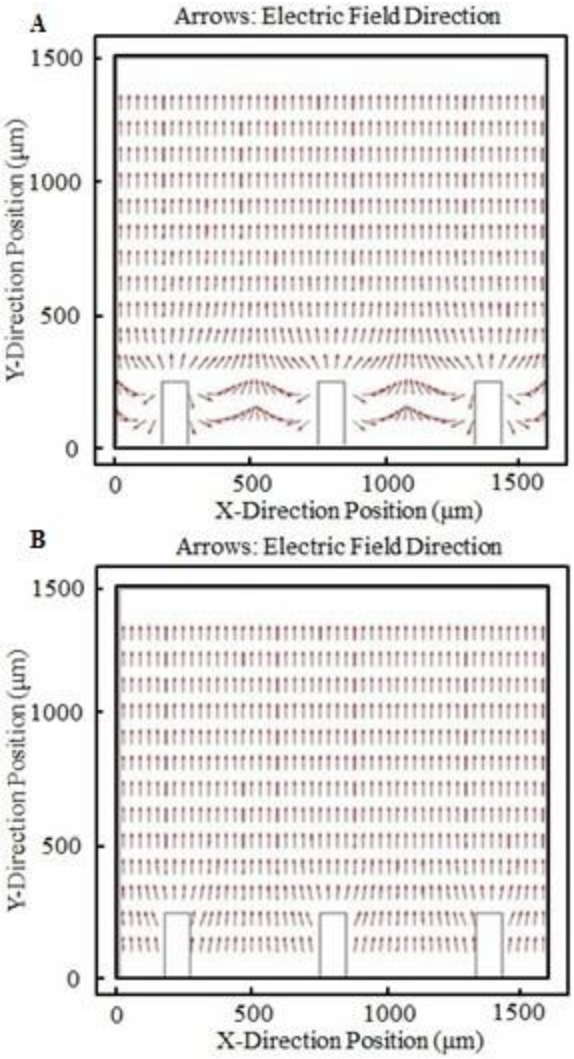

Figure 3.11: *Electric field direction at central plane of the three-capillary device for: A) Point to plane electrode configuration; B) Parallel electrode configuration;*

The uniformity of electric field intensity is a critical factor in ensuring the monodispersity of the droplets generated. The electric field intensity is calculated as:

$$E_n = \sqrt{{E_x}^2 + {E_y}^2 + {E_z}^2} \tag{3-11}$$

Where y axis is the direction along the axis of the capillary and is perpendicular to the nozzle cross section. In both the configurations the X and Z components of the electric field is not

significant since they are less than 1% of the Y component of the electric field. Therefore $E_n \approx E_y$ is obtained.

The electric field intensity at the central point of the three capillaries obtained from simulation is shown in **Figure 3.12**. It can be seen that the electric field intensity in the point to plane electrode configuration is higher than that in the parallel electrode configuration for the same applied potential. As illustrated in **Figure 3.13**, the parallel electrode configuration (**Figure 3.13C**) can be considered as a combination of the point to plane (**Figure 3.13A**) and parallel plane electrode configurations (**Figure 3.13B**), which results in higher uniformity of electric field along the axis of the channel. Instead of converging into the tip of the capillaries, in the second design, the electric field lines are more uniformly distributed along the positive microelectrode, which results in the decrease of electric field intensity at the capillary tips. Also, it can be seen from **Figure 3.12** that the electric field intensity of the tips of the various nozzles are not the same but are dependent on their positions. For instance, the electric field at the tip of the central capillary is higher than that at the side of the capillaries. The amount of variation also depends on the number of capillaries in the configurations as can be seen from **Figure 3.12**. The higher electric field intensity at the center electrode can be explained based on the illustration in **Figure 3.14**. Because of the configuration of the channel, the central electrode is exposed to a greater proportion of the ground electrode compared to the side electrodes. Therefore, a higher number of electric field lines converges onto the central capillary and contributes to the higher electric field intensity. This difference in electric field intensity is obviously lower in the second design, which can be attributed to the introduction of the linear positive electrode.

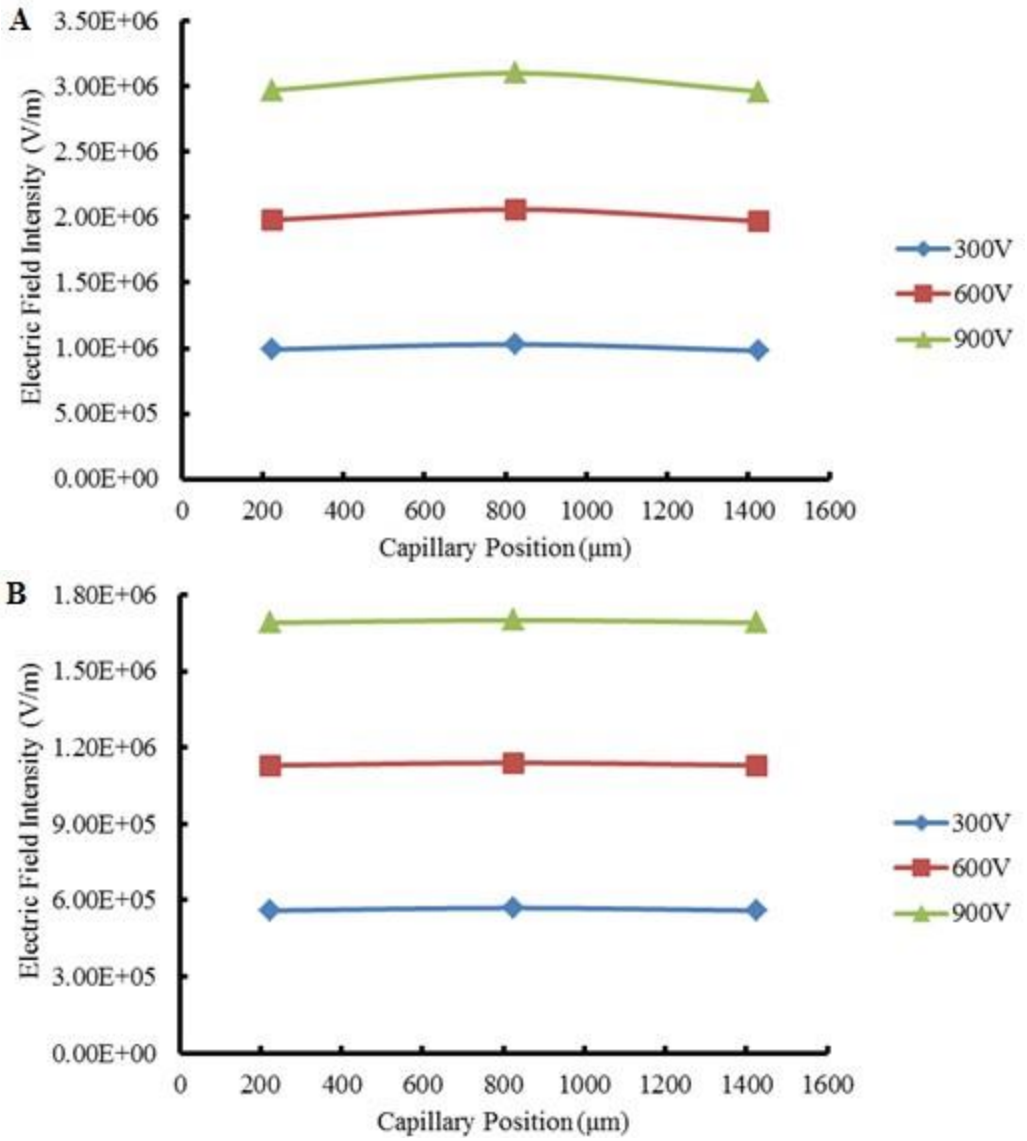

Figure 3.12: *Electric field intensity at the center of each capillary of the three-capillary device in: A) Point to plane electrode configuration; B) Parallel electrode configuration;*

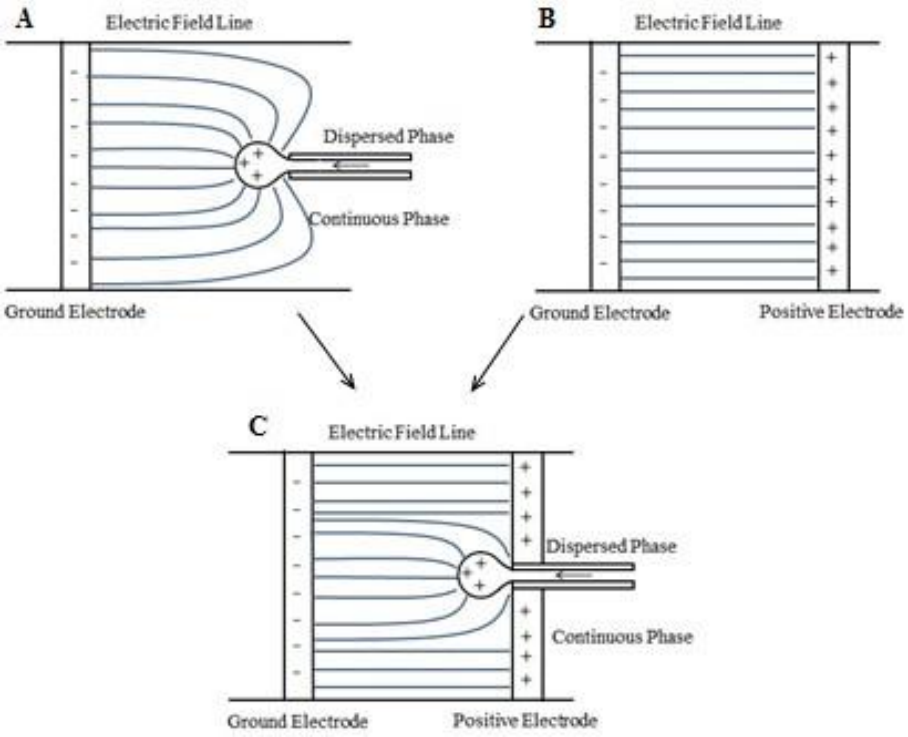

Figure 3.13: *Schematic illustration of electric field distribution in various electrode configurations: A) Point to plane electrode configuration; B) Parallel plate electrode configuration; C) The combination (Named as parallel electrode configuration in this research)*

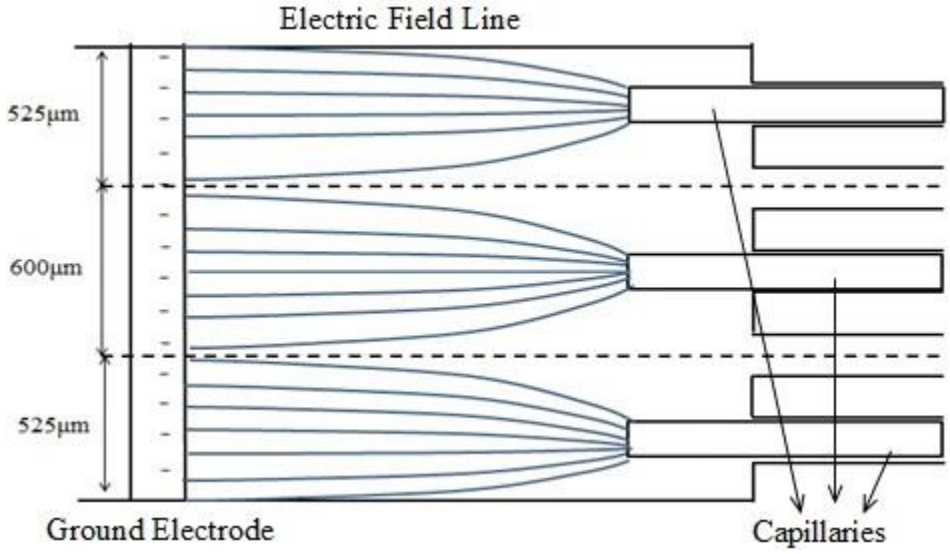

Figure 3.14: *Schematic of electric field distribution of the three-capillary device*

To further investigate the uniformity of electric field intensity in both designs, the normalized electric field is defined as:

$$\text{Normalized Electric Field} = \frac{Electric\ Field\ Intensity\ at\ Local\ Capillary}{Electric\ Field\ Intensity\ at\ the\ Central\ Capillary} \quad (3\text{-}12)$$

Figure 3.15 shows the normalized electric field in both electrode configurations. The maximum difference between electric field intensity at different capillaries is 4% in the point to plane electrode configuration and 1% in the parallel electrode configuration. The simulation results show that the electric field intensity is more uniform in the parallel electrode configuration.

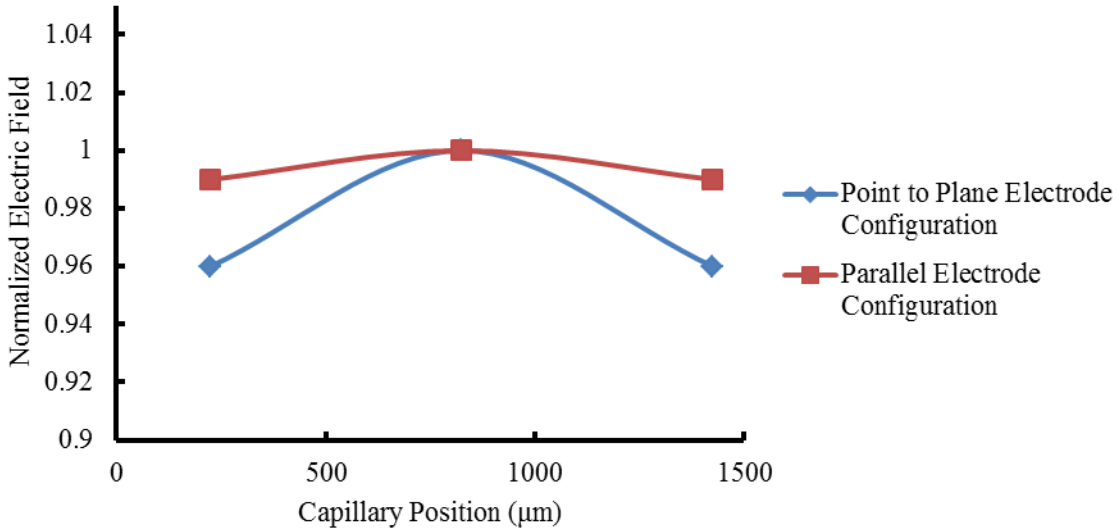

Figure 3.15: *Normalized electric field in the three-capillary device in the point to plane electrode configuration and the parallel electrode configuration*

In the device with five capillaries, similar simulations were performed. The electric field direction at the central plane (**Figure 3.16**, z = 75 μm) of the device is illustrated in **Figure 3.17**. Similar to the three capillaries situation, higher uniformity of electric field direction is observed in the parallel electrode configuration. This can also be attributed to the introduction of linear positive electrode.

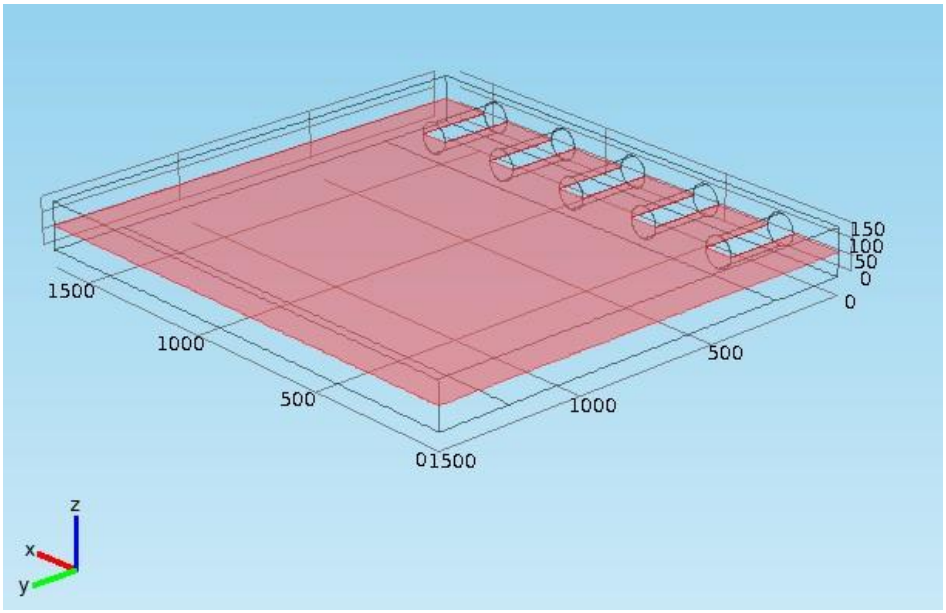

Figure 3.16: *Central plane of the five-capillary device*

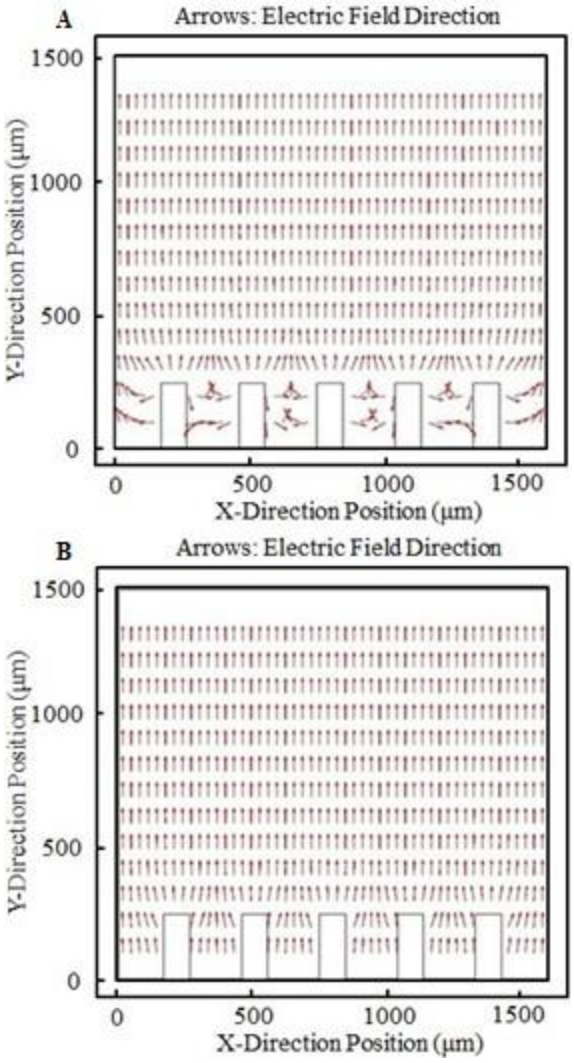

Figure 3.17: *Electric field direction at central plane of the five-capillary device for: A) Point to plane electrode configuration; B) Parallel electrode configuration*

Figure 3.18 shows the electric field intensity at the central points of each capillary for the point to plane electrode configuration. The variation in electric field between the capillary tips was different compared to the three capillaries situation; electric field intensity is the smallest at central capillary and is the largest at the side capillaries. This is due to the different geometric arrangements of capillaries in two situations as illustrated in **Figure 3.19**. In this particular geometry, the largest segment of ground electrode is in close proximity to the side capillaries while the smallest segments are close to the central capillaries. Similar to the three

capillaries situation, the parallel electrode configuration provides a more uniform electric field distribution. The normalized electric field is shown in **Figure 3.20**. Compared to maximum difference of up to 10% in electric field intensity in the point to plane electrode configuration, the parallel electrode configuration reduces the maximum difference to less than 4%.

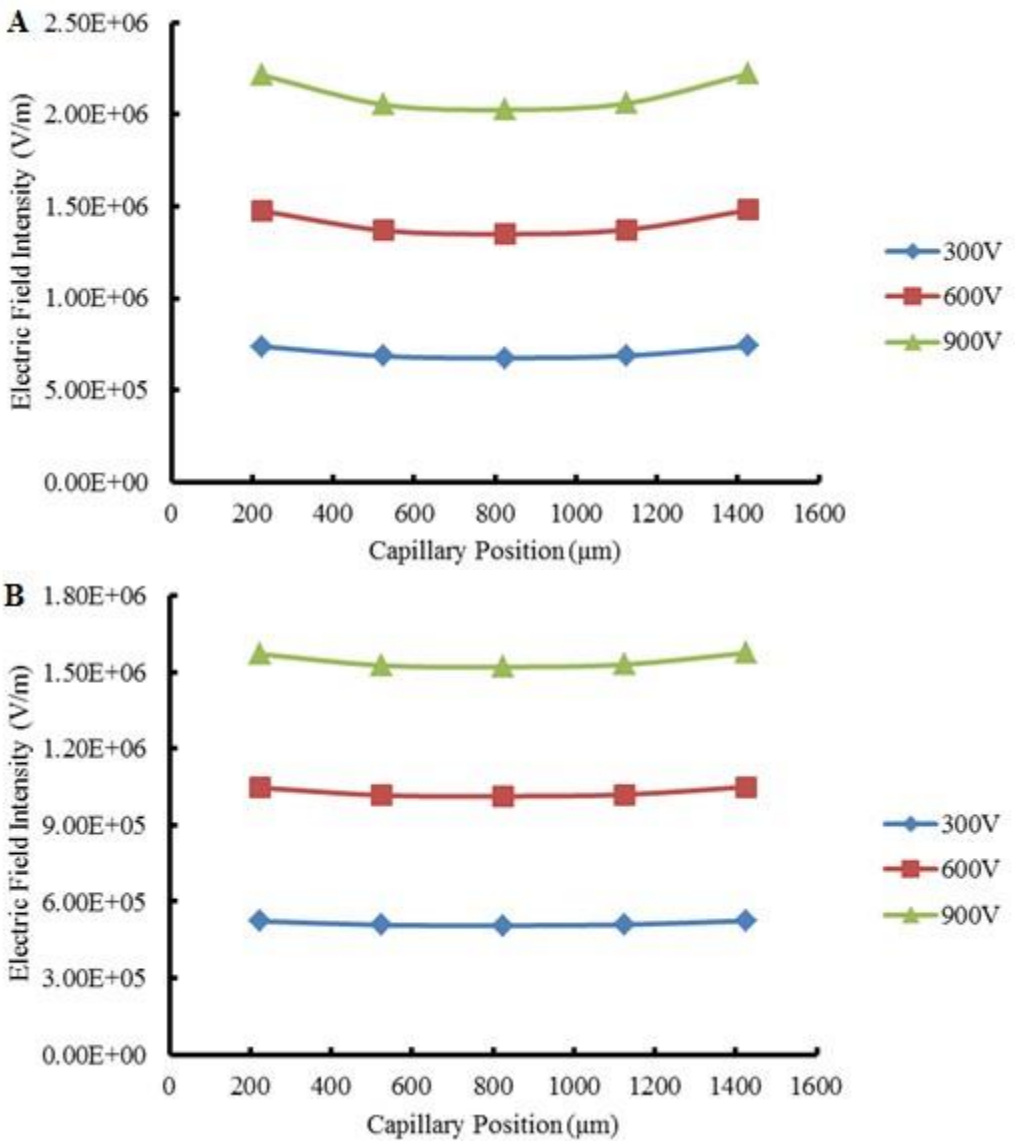

Figure 3.18: *Electric field intensity at the center of each capillary of the five-capillary device in: A) Point to plane electrode configuration; B) Parallel electrode configuration;*

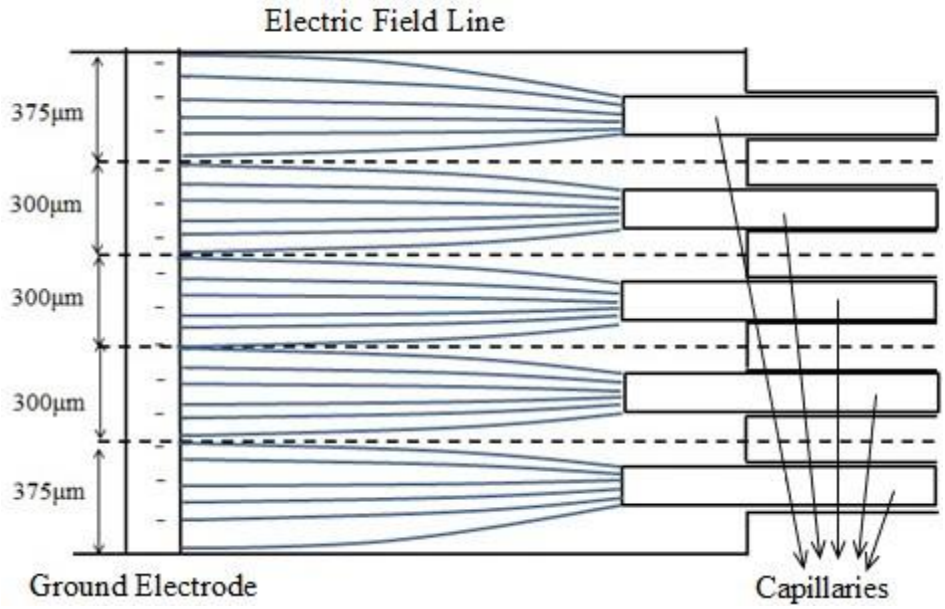

Figure 3.19: *Schematic of electric field distribution of the five-capillary device*

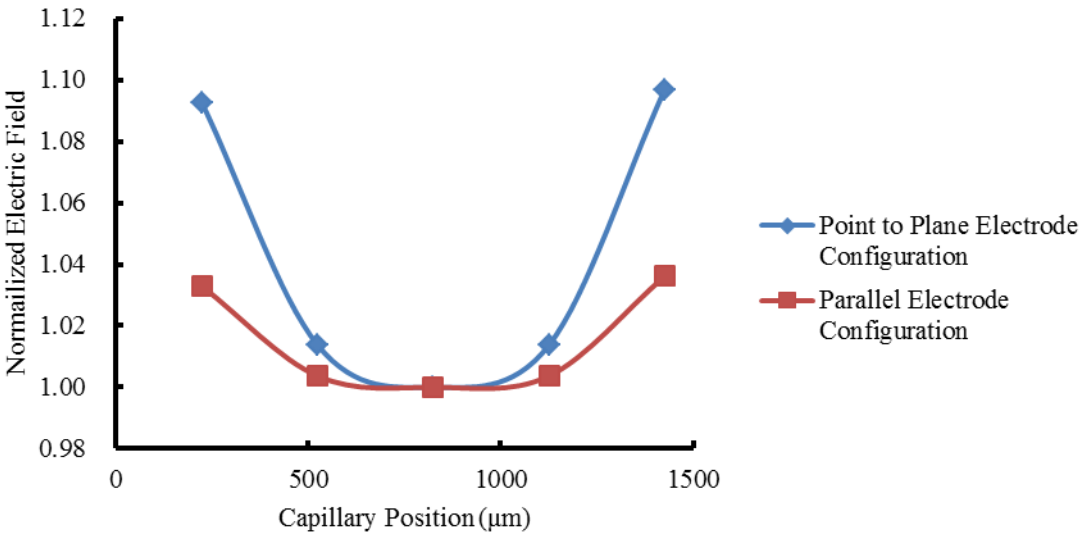

Figure 3.20: *Normalized electric field in the five-capillary device in the point to plane electrode configuration and the parallel electrode configuration*

3.3.3.2 Experimental Validation

Figure 3.21 shows the experimental results in both designs. All the flow rates of continuous phase are 15 mL/hour while the dispersed flow rate is 0.01 mL/hour per capillary.

The potential applied to the devices in **Figure 3.21B** and **C** is 800 V while the potential applied to the devices in **Figure 3.21A** and **D** is 1000 V. In the point to plane electrode configuration, large variations in droplet sizes (from ~ 1 μm to ~ 20 μm) between different capillaries are observed in both **Figure 3.21A** and **B**. Moreover, instead of moving horizontally along with the flow towards the ground electrode, the droplet stream at each capillary diverged from each other. The reason is that the electric field lines diverged and droplets therefore followed the path in the local vicinity, when the electric field was high and then the flow took over.

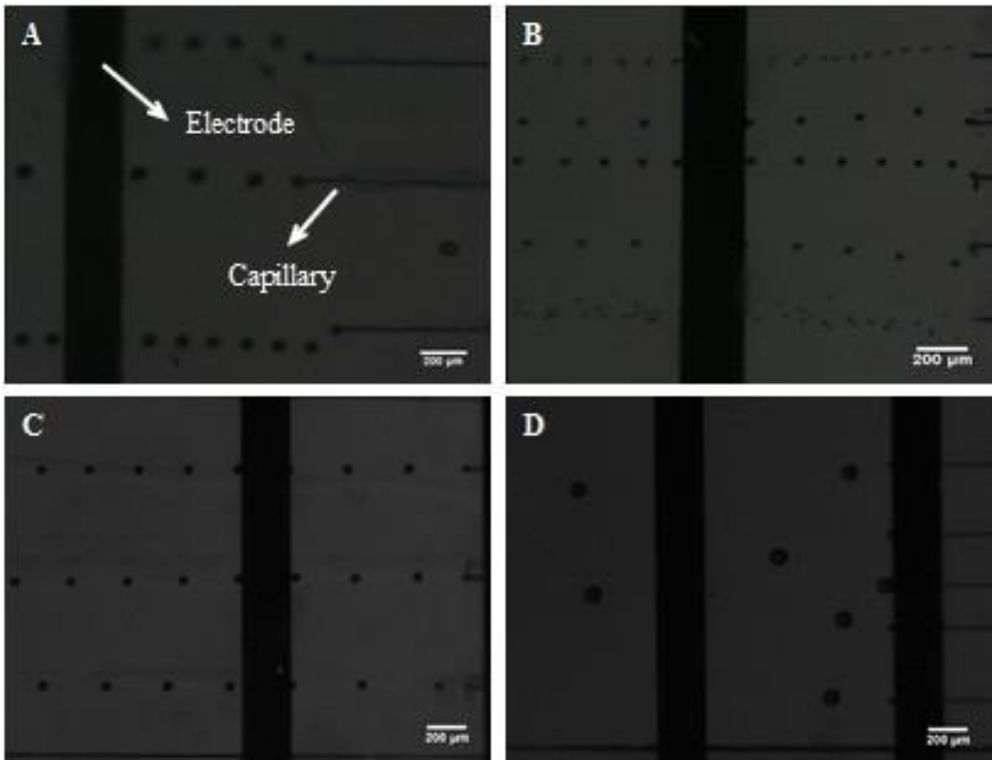

Figure 3.21: *Experimental results for: A) the three-capillary device in the point to plane electrode configuration; B) the five-capillary device in the point to plane electrode configuration; C) the three-capillary device in the parallel electrode configuration; D) the five-capillary device in the parallel electrode configuration*

In the parallel electrode configuration, monodispersed droplets with standard deviation less than 6% of the diameter of the droplets generated through various nozzles in the multi-capillary configuration were generated. Also, the flow paths of the droplets were along the axis

of the flow channel and parallel to each other. This is because the electric field lines in the parallel electrode configuration were more uniform.

Both the simulation and experimental results demonstrate that the parallel electrode configuration provides more uniform electric field distribution and it is therefore selected as the electrode configuration for the designed device.

3.4 Summary

In this chapter, the design of the parallelized, electrically controlled droplet generation device is presented in detail. A simple fabrication process was devised by assembling microcapillaries into PDMS channel with appropriate grooves in it and used as the channels for different phases of flow. Two electrode configurations are proposed. These configurations were evaluated by Comsol multi-physics simulation as well as preliminary experiments, to determine the design that would be suitable for generating monodisperse droplets. The parallel electrode configuration was shown to generate more uniform electric field than the point to plane electrode configuration, so it is selected for subsequent investigation.

Chapter 4 Materials & Device Fabrication

4.1 Introduction

In previous chapter, the working principle of the device was discussed and the design of the device was optimized. According to the design, the microfabrication process flow has to be developed. The choice of a suitable fabrication method and materials depends on a number of factors such as ease of fabrication and cost. In this chapter, the fabrication process is detailed and the materials used are described.

4.2 Materials

4.2.1 PDMS

Polydimethylsiloxane (PDMS) (SYLGARD® 184, Dow Corning, Midland, MI), with the chemical formula of $CH_3[Si(CH_3)_2O]_nSi(CH_3)_3$, is the most widely used silicone material for microfabrication and rapid prototyping. Due to its characteristics such as optically clarity, inertness and biocompatibility, PDMS has been used to fabricate microfluidic chips with the feature sizes that could be as small as a few micrometers. The PDMS polymer (base) is mixed with a cross linker and the mixture is cured at 80℃ for 2 hours to form the PDMS elastomer. Different mixing ratios will result in different elasticity of the PDMS chips. Usually, a ratio of 10 base to 1 curing agent is used to fabricate microchannels.

4.2.2 Mineral Oil

A mineral oil is a colorless, odorless and light mixtures of alkanes in the C15 to C40 range from a non-vegetable (mineral) source, in particular distilled from petroleum, with the chemical formula of $C_nH_{2n+2.}$ It is widely used as food additive, lubricant and cosmetics. Its non-conductive and non-polar nature makes it an ideal continuous phase in micro-electro-fluidic systems for emulsification. The mineral oil (paraffin oil) with a density of 0.845 kg/L is used as the continuous phase in this research.

4.2.3 Sorbitan monooleate (Span80)

Sorbitan monooleate (Span80) is an oil soluble surfactant. Surfactants are compounds used to lower the interfacial tension between two phases. They are usually organic compounds with both hydrophobic and hydrophilic parts. The structure of span 80 is illustrated in **Figure 4.1** in which both water soluble end (-OH) and the oil soluble end ($–CH_3$) can be observed. When water is mixed with oil, the span-80 forms a layer around the water droplet with the –OH side in the water and the $–CH_3$ side in the oil, which reduces the interfacial tension between the oil and the water. It helps to stabilize the droplet by reducing the possibility of droplet merging.

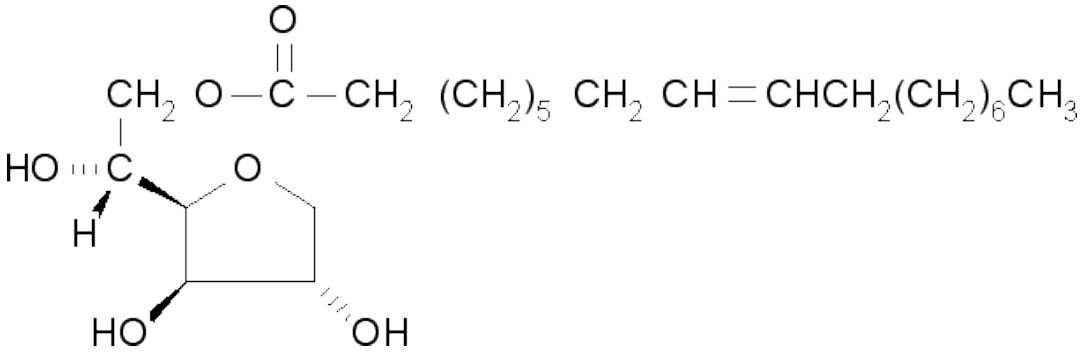

Figure 4.1: *Structure of span80 [Sigma Aldrich]*

4.2.4 Methylene Blue

Methylene blue (MB) is a polar water soluble chemical compound with the chemical formula of $C_{16}H_{18}N_3SCl$ (**Figure 4.2**). It is a dye that has been widely used in chemical and biological experiment due to its distinct blue color. MB solution increases the conductivity of DI water, resulting in higher sensitivity of droplet size to potential changes. 1% MB solution is used in this research referring to previous research [61].

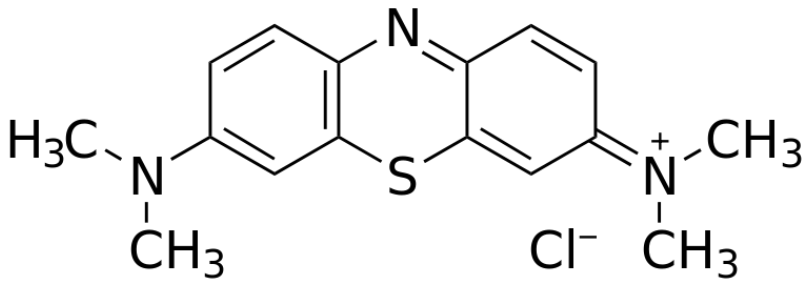

Figure 4.2: *Chemical structure of methylene blue [Sigma Aldrich]*

4.2.5 Rain-X

Rain-X® (SOPUS Products Inc. Houston, TX) is a surfactant like chemical for surface treatment with water repellent property. When Rain-X is deposited onto a surface, it can form a thin layer on the surfaces and the exposed hydrophobic groups can effectively convert the surface into one hydrophobic surface (**Figure 4.3**).

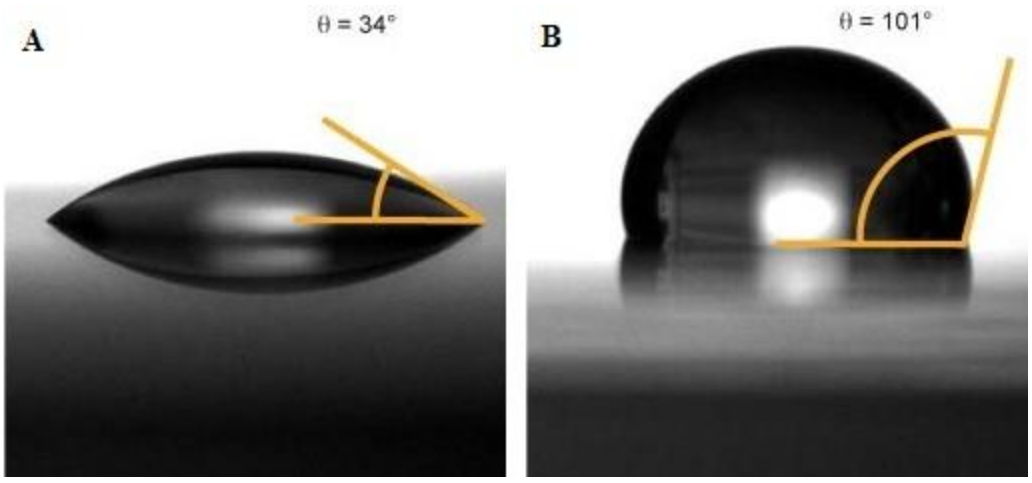

Figure 4.3: *Contact angle between water and glass slide: A) before the treatment of Rain-X; B) after the treatment of Rain-X* [62]

4.2.5 Capillary Tubing

Polymicro Capillary (Molex Inc. Phoenix, AZ) is a capillary tubing with inner & outer diameters in the order of a few tens to hundreds of micrometer. It is coated by a layer of polymer to prevent the outer surface from abrasion. Its superior properties such as smooth inner surface and high purity make it an ideal material for the channels of dispersed flow. The outer diameter of the commercialized capillary ranges from 100 μm to 850 μm and the inner diameter ranges from 2 μm to 700 μm.

4.3 Fabrication Techniques

4.3.1 Soft Lithography

Soft lithography was used to fabricate the microchannel for this device. Initially introduced by Xia et al. [63], it has already become the most common technique to prototype microchannels due to its low cost and high accuracy. Soft lithography refers to a method that

transfers the patterns from a mold onto an elastic material, using a three step process flow: 1. Mould fabrication, 2. Pattern transfer, 3.Bonding with another substrate.

For the mould fabrication, the photolithography method is well established and widely used. The exposure of photoresist to UV through a photomask transfers the mask patterns on to the photoresist by producing a physical relief in the exposed areas. These patterns can achieve an accuracy of several hundred nanometers. The liquid PDMS pre-polymer is then cast on the mould to replicate the feature. After curing at 80℃ for 2 hours, the PDMS with the patterns can be easily peeled off from the mould. Finally, the PDMS piece and another substrate (PDMS or glass) are treated with Oxygen Plasma and bonded together, forming a microfluidic chip.

4.3.2 Metal Deposition

Metal deposition is widely used to fabricate electrodes in MEMS devices. There are a number of methods to deposit metal films, such as electric arc, e-beam, plasma spray, ion plating and sputtering deposition [64]. In this work, sputter deposition was used. Sputtering is a physical vapor deposition process in which a gas plasma discharge is set up between two electrodes: a cathode source material and an anode substrate. Positively charged gas ions are attracted to and accelerated into the cathode. The plasma knocks atoms off the cathode, which impact the anode and coat the substrate.

4.4 Device Fabrication & Assembly

4.4.1 Overview of Fabrication Process

The whole fabrication process involves 4 parts: 1. The fabrication of the channel for continuous flow; 2. The fabrication of the substrate electrode; 3. The preparation of the

capillaries for dispersed flow; 4. The assembly of the device. In this section, the fabrication steps are discussed in detail.

4.4.2 Fabrication of the Main Channel for Continuous Phase

As discussed in last section, photolithography can be used to fabricate the mould for the main channel as its feature size is 150 micrometers. First, the mask with the feature of main channel was designed using AutoCAD. This feature was then transferred onto the 150 μm thick SU8-2075 photoresist layer on a 3-inch silicon wafer (University Wafers, MA, USA) by photolithography (**Figure 4.4**). The detailed recipe is provided in Appendix A.

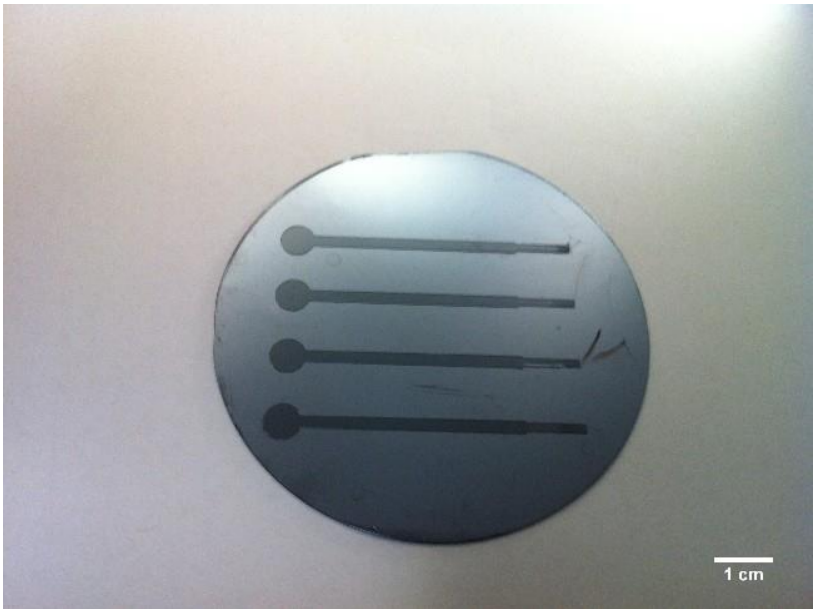

Figure 4.4*: *Patterns on the silicon wafer

Figure 4.5 illustrates the fabrication process of the main channel. Before casting PDMS pre-polymer on the mould, two 1cm long MasterFlex 1.6 mm ID silicone tubing (Cole Palmer, Ontario, Canada) were placed photolithographic pattern to serve as the inlet and outlet. The PDMS pre-polymer is cast on the mould and cured at 80 ℃ for 2 hours forming an elastomer with

an imprint of the channel and also attached to the interconnects. The PDMS elastomer with the microchannel was then cut and peeled off from the wafer (**Figure 4.5**). A 1.5 mm diameter tissue-punch was used to clean the inlet and outlet interconnects.

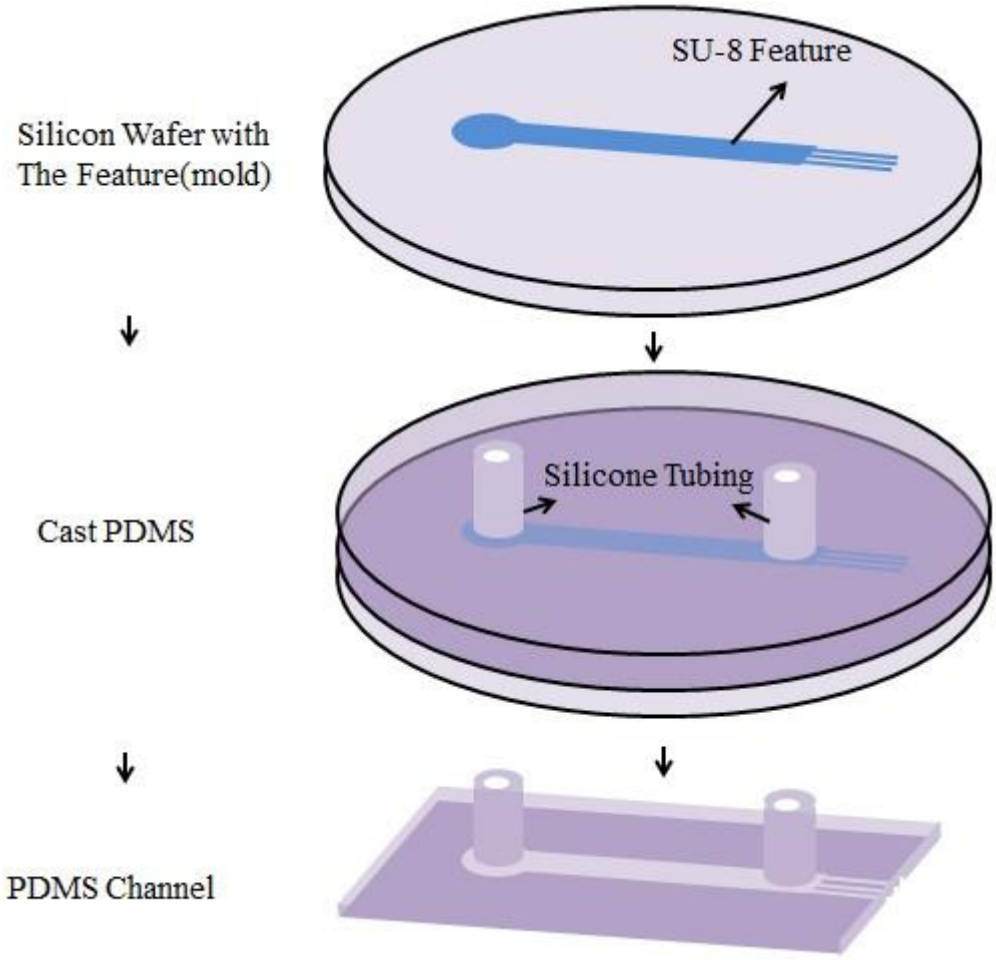

Figure 4.5: *Process of fabricating main channel*

4.4.3 Fabrication of the Substrate with Electrodes

The fabrication process of the electrodes is illustrated in **Figure 4.6**. Photolithography was used to create the negative relief of the electrode pattern on the glass slide. A S1818 photoresist layer with 20 μm thickness is coated on the glass slide after Photolithography. Then 5 nm of Cr and 200 nm Au were deposited on the glass slide by sputtering. Chromium serves as the adhesive layer between gold and the glass substrate. After deposition, the substrate was

immersed in acetone to dissolve the photoresist and remove the metal deposited on top of it, leaving behind a pattern of gold electrodes on the glass substrate (**Figure 4.7**). Finally, two sections of silver wires (0.2 mm diameter, Warner Instruments, Haden, CT, USA) were soldered on the electrode pads.

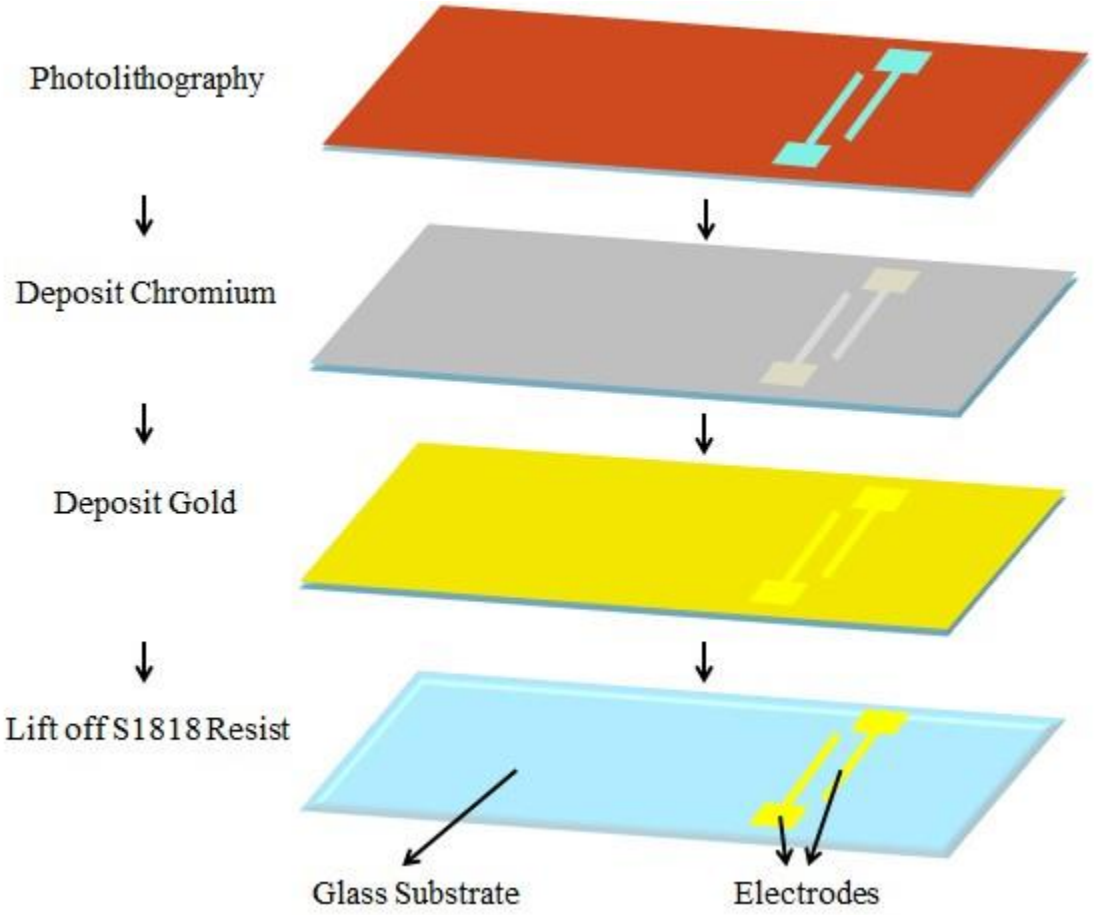

Figure 4.6: *Fabrication process of electrodes*

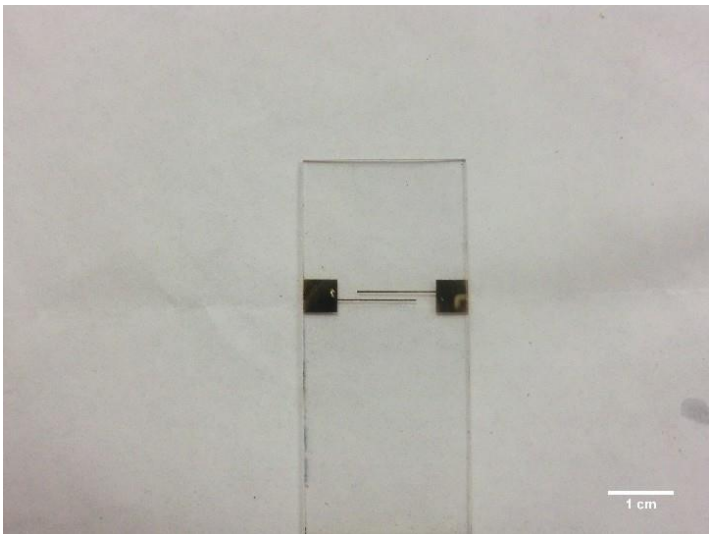

Figure 4.7: *Electrodes on the glass substrate*

4.4.4 Fabrication of the capillaries

In this device, capillaries are used to form the channels and nozzles for the dispersed flow. The shape of the tip of the capillaries is critical for the functioning of the device. Traditional tools, such as scissors and scalpels, will cut an uneven surface at the tip (**Figure 4.8A**). To make a planar and smooth tip surface, capillary column cutter (SGT, Netherland) was used to cut the capillaries. A diamond blade is installed inside the cutter. By rotating the wheel on the cutter, the blade inside will rotate around the capillary and finally cut it. This cutting process will ensure a planar and smooth surface of the capillary tip that is perpendicular to the axis of the capillary (**Figure 4.8B**). The capillaries were cut into 4.5 cm segments, after which the coating polymer on both ends was removed. The capillaries were treated in Rain-X for 30min to make the cross-sectional surface of the tip hydrophobic.

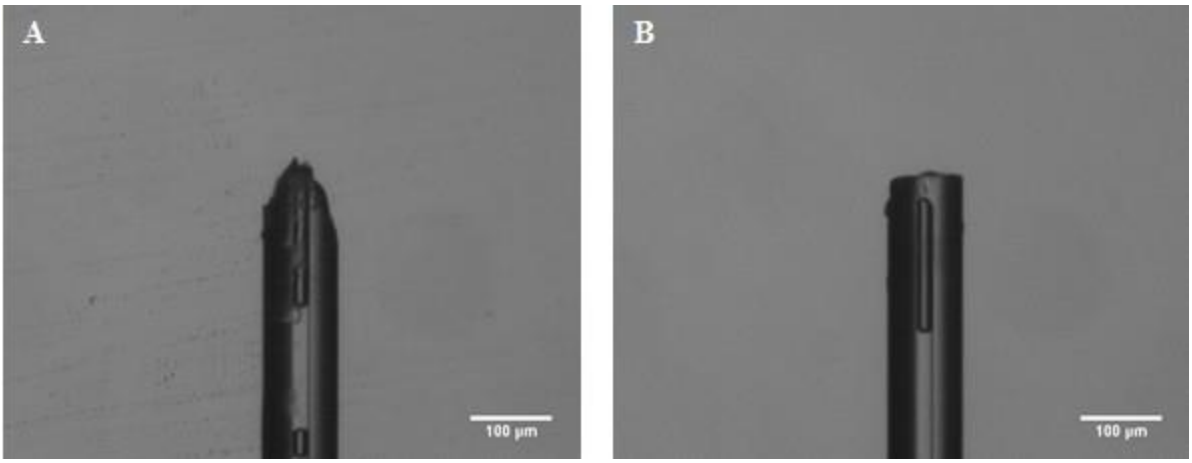

Figure 4.8: *A) Capillary cut by scissors; B) Capillary cut by SGT capillary cutter*

4.4.5 Assembly of the device

Figure 4.9 shows the assembly of the device. The main channel and the glass substrate were treated with oxygen plasma for 1 minute at a power of 60W. After the surfaces were activated by the plasma, they were brought into contact and left for 24 hours to improve bonding strength. Then, the Rain-X was injected into the channel and the device was heated on a hot plate at 80℃ for 30 min, resulting in a conformal coating of the Rain-X on the glass substrate and PDMS channel. This coating makes all the surfaces of the channel hydrophobic, which prevents surface attachment of the formed droplets.

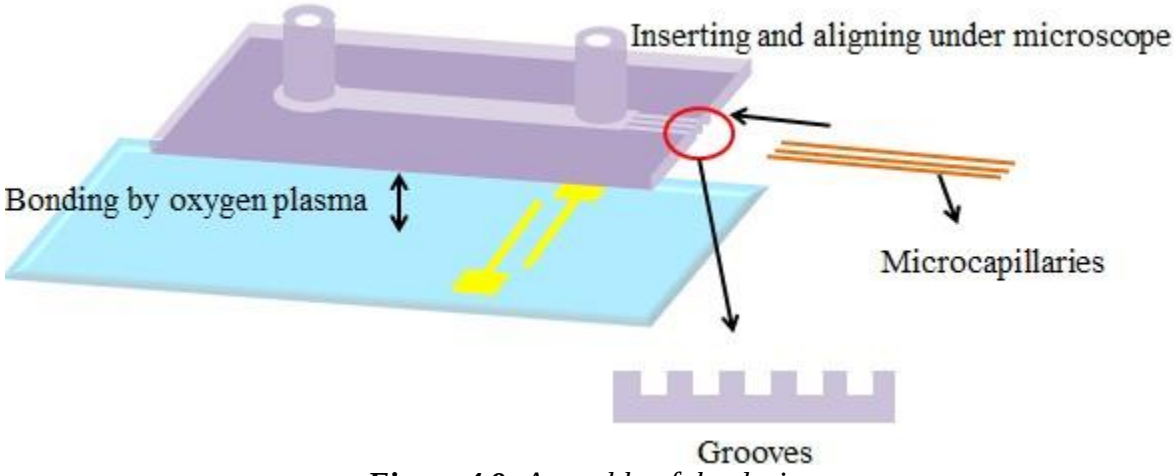

Figure 4.9: *Assembly of the device*

The capillaries were carefully inserted into the main channel through the grooves on PDMS pieces. The alignment was done under the microscope (**Figure 4.10**). Once all the capillaries were put into the right position, PDMS pre-polymer was used to seal the inlet of the grooves and fix the position of capillaries. Then, the other ends of the capillaries were put into a glass capillary and sealed with epoxy glue. The device is illustrated in **Figure 4.11**.

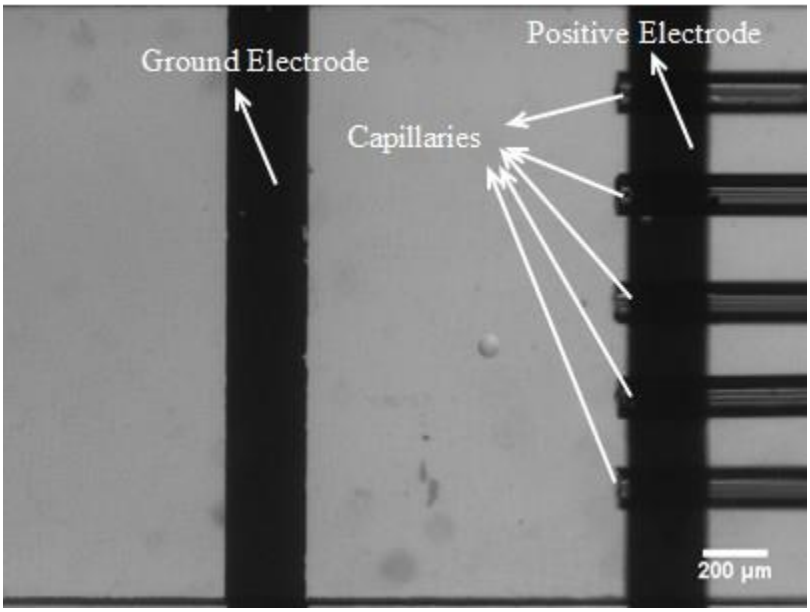

Figure 4.10: *Alignment of capillaries under microscope*

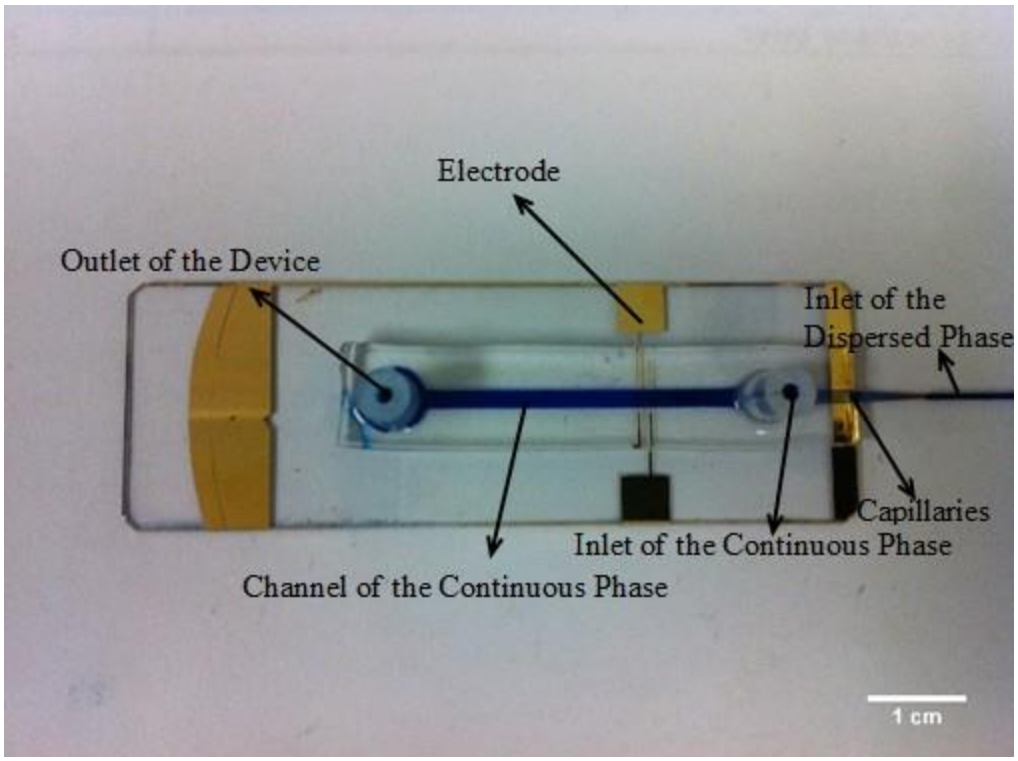

Figure 4.11: *Multi-Capillary droplet generating device*

4.5 Summary

In this chapter, the materials used in the device as well as fabrication process were discussed in detail. Due to the inexpensive fabrication process adopted in this work, the device is fairly low cost compared to other parallelized droplet generating devices [34][57]. In addition to the low cost of fabricating the device, this fabrication process was found to be repeatable and can be performed in a non-clean room environment.

Chapter 5 Results & Discussion

5.1 Introduction

In the previous chapter, details of the fabrication process and materials used in the fabrication were presented. In this chapter, the droplet generating process in the device is systematically characterized, mainly the influence of the potential and the continuous flow rate is fully studied, and the experimental results are compared with the theoretical analysis. The influence of the dispersed flow rate as well as the electric field distribution is also analyzed. The parallelization of droplet generation has been demonstrated.

5.2 Experimental Setup

The experimental setup is illustrated in **Figure 5.1.** It consists three parts: 1) the power supply which was used to apply DC potentials; 2) the imaging setup with a camera and a microscope was used to record the experiment video and 3) the fluidic setup consisted of syringe pumps that were used to provide both the continuous flow and the dispersed flow.

Keithley 2810 (Keithley Inc.) was used to provide DC potential for the device. As illustrated in **Figure 5.2**, the positive electrode was connected to the microfabricated planar electrode on the device as well as the dispersed phase (DI water + 1% methylene blue) syringe. The ground was connected to another microfabricated planar electrode on the glass substrate.

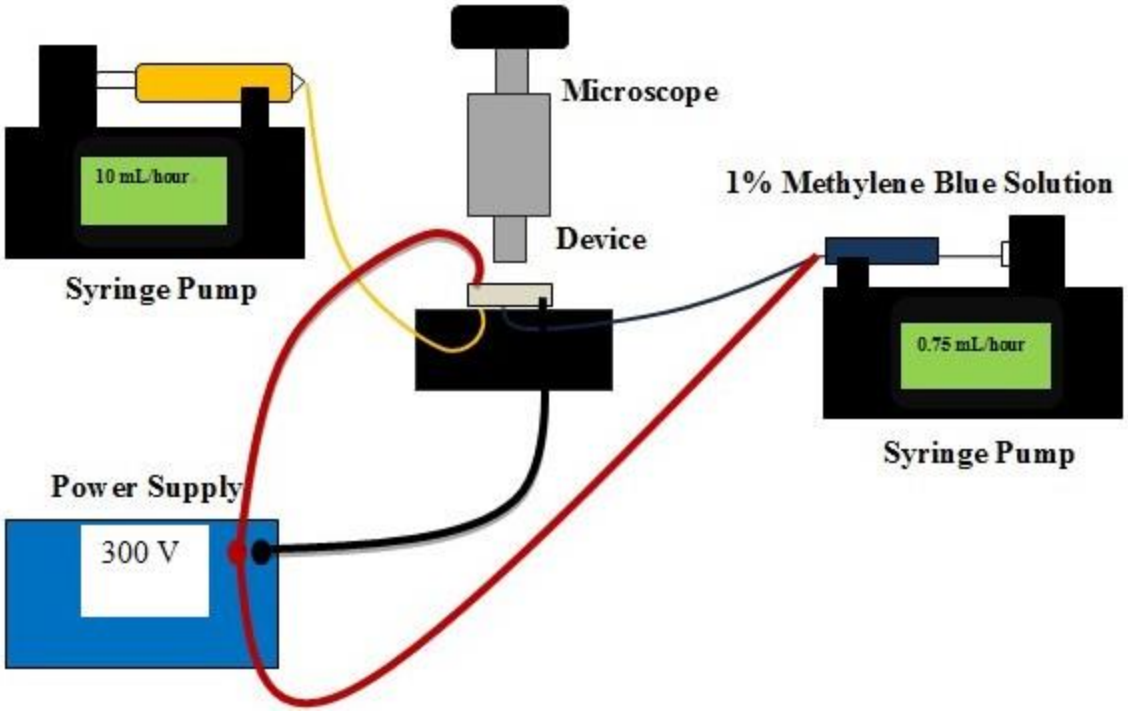

Figure 5.1: *Schematic of the experimental setup*

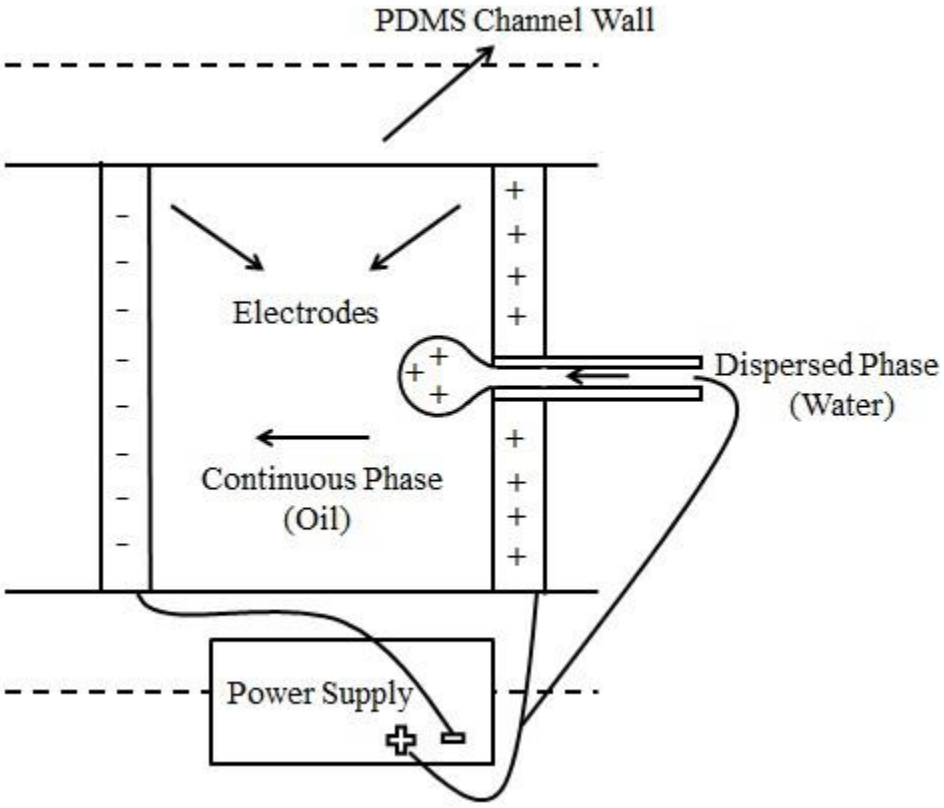

Figure 5.2: *Schematic of the connection between the power supply and the device*

The microscope and camera were used to record the experimental video. Particle Analysis Module of ImageJ was utilized to obtain the droplet area, from which the diameter of droplet was extracted. When processing the videos, one droplet appearing in two adjacent frames might influence the calculation of average droplet size due to double counting of the droplet. A specific recording frame rate correlated with the generating rate should be set to avoid the double counting. The time between two frames should be enough for a droplet to moving out of the frame from the generating position (the tip of the capillary). Assuming that the distance between the tip of the capillary and the boundary of the frame is L; the velocity of the droplet is V (same with continuous flow's velocity) and the recording frame rate is N/s, the relation should be as follows:

$$\frac{1}{N} \cdot V > L \tag{5-1}$$

$$\mathrm{N} < \frac{V}{L} \tag{5-2}$$

In our experiments, L = 0.0024 m, $V \geq 0.011$ m/s, N is therefore smaller than 0.011/0.0024 = 4.58. The frame rate was then set to 4 frames per second to record the videos with 50 frames. We measured 5 droplets at each capillary in two identical devices to obtain the droplet size and its standard deviation for all videos.

Two solutions were used in the experiment. The first one is Paraffin oil solution (Caledone Inc.) mixed with 1 % of Span80 surfactant (Fluka Inc.). This oil solution was mixed by manually agitating the medium for several minutes. The second is DI water solution mixed with 1% methylene blue (Sigma Aldrich Inc.). The oil solution (in a 10ml syringe) was infused to the device by KDS Legato 270 positive displacement syringe pumps. The methylene blue solution (in a 3ml syringe) was injected by a Harvard Apparatus 22 infusion pump which can

ensure precise infusion of the liquid. The density, viscosity, interfacial tension and relative dielectric constant of the paraffin oil are 845 kg/m^3, 12.2 cSt, 0.003 N/m and 2.2, respectively [61].

5.3 Characterization of the Single-Capillary Device

The single-capillary device was first characterized. The tip of the microcapillary is in the configuration as depicted in **Figure 5.3** and tested under various potentials, continuous flow rates, dispersed flow rates and electric field distributions. Theoretical and conceptual explanations are presented.

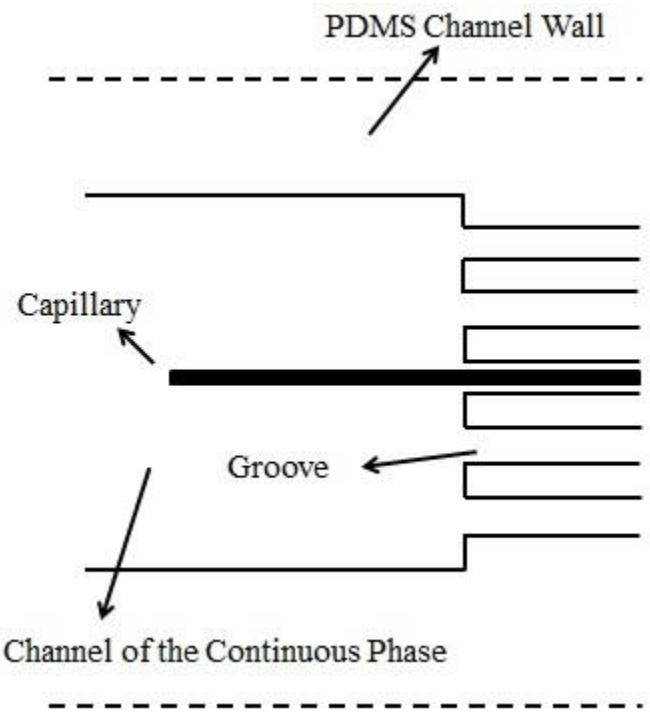

Figure 5.3: *Schematic of the single-capillary device*

5.3.1 Effect of the Potential

As illustrated in **Figure 5.4,** the droplet size decreases as the applied potential is increased. Moreover, it is a consistent trend for various continuous flow rates (10 mL/hour, 12.5 mL/hour, 15 mL/hour). As discussed in theoretical analysis in chapter 3, electrostatic force has a

quadratic dependence on the electric field intensity E_n (Equation 3-5). As E_n increases, the electrostatic force therefore becomes increasingly significant in the droplet generating process, reducing the droplet size.

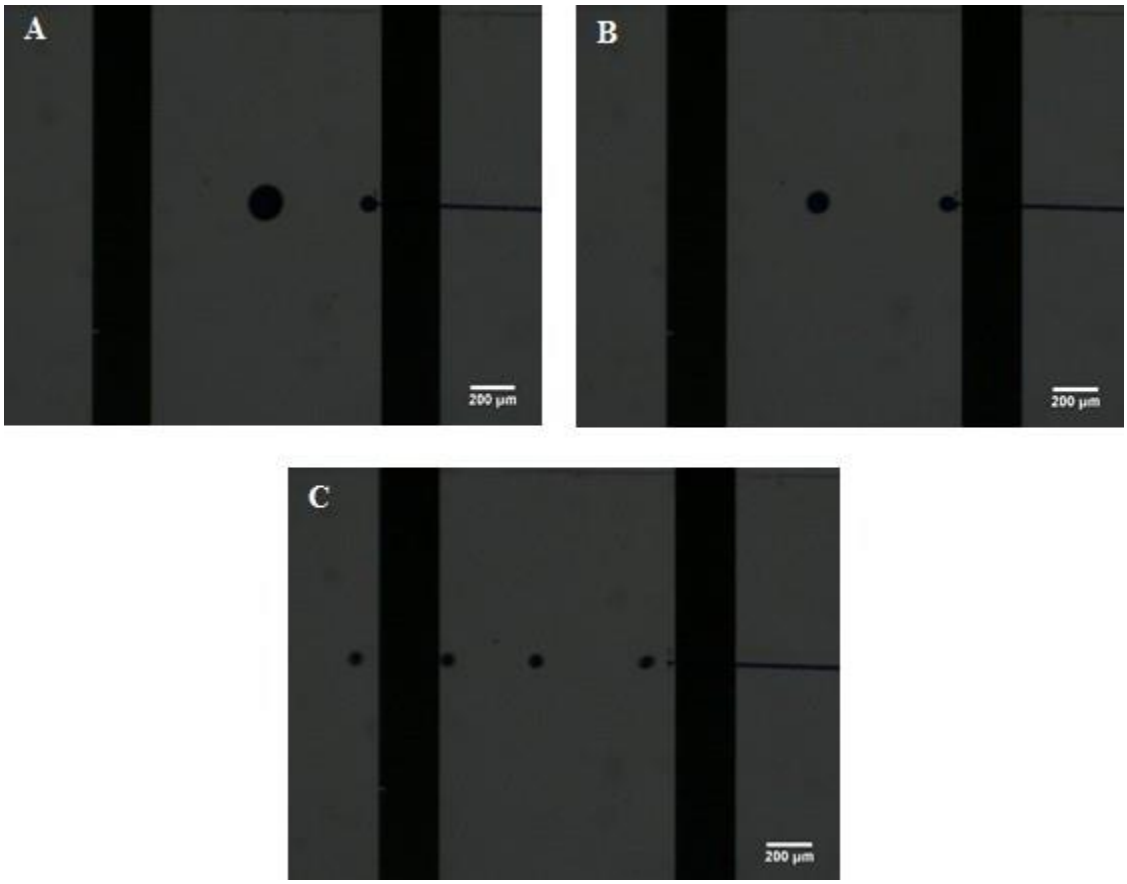

Figure 5.4: *Droplet generation under potential of: A) 400 V; B) 600 V; C) 1000 V (0.01 mL/hour dispersed flow rate, 10 mL/hour continuous flow rate) in the single-capillary device*

Equation 3-6 mathematically depicts the droplet generating process in a uniform electric field. By solving this equation, the droplet size under various working conditions of the device can be easily derived. However, due to the complexity of the electric field (**Figure 3.5**) in the present setup and the influence of the emerging droplets' shape, the relation between the applied potential and the electric field intensity at the surface of droplets needs to be determined carefully. Previous research showed that, in addition to the applied potential (U) and the distance

between two electrodes (D), the electric field intensity around the curved surface also relies on the diameter of the formed droplets (d) [65]:

$$E_n = f(U, D, d) \tag{5-3}$$

Comsol multiphysics simulation was used to derive the relation. The simulated geometry is illustrated in **Figure 5.5**. One cylinder was setup to mimic the capillary and a sphere at the tip of the capillary was setup to mimic the droplet. With varied droplet diameters from 20 μm to 100 μm, the electric field intensity at the tip of the droplet was obtained under various potentials (200 V, 400 V, 600 V, 800 V and 1000 V). To simplify the model, electric field intensity at the surface of the droplet is assumed to be uniform [65] and this assumption is further demonstrated by the simulation results in which shows that the average electric field intensity is ~ 80% of the electric field intensity at the tip of the droplet. All other assumptions, dimensions and governing equations are the same with those in the simulation discussed in chapter 3, which are presented in detail in Appendix B.

The simulation results were displayed in a plot of local electric field intensity at the surface of the droplet (E_n) vs. nominal electric field (potential divided by distance between droplet and ground electrode ($\frac{U}{D}, D \approx 0.001m$) as shown in **Figure 5.6**.

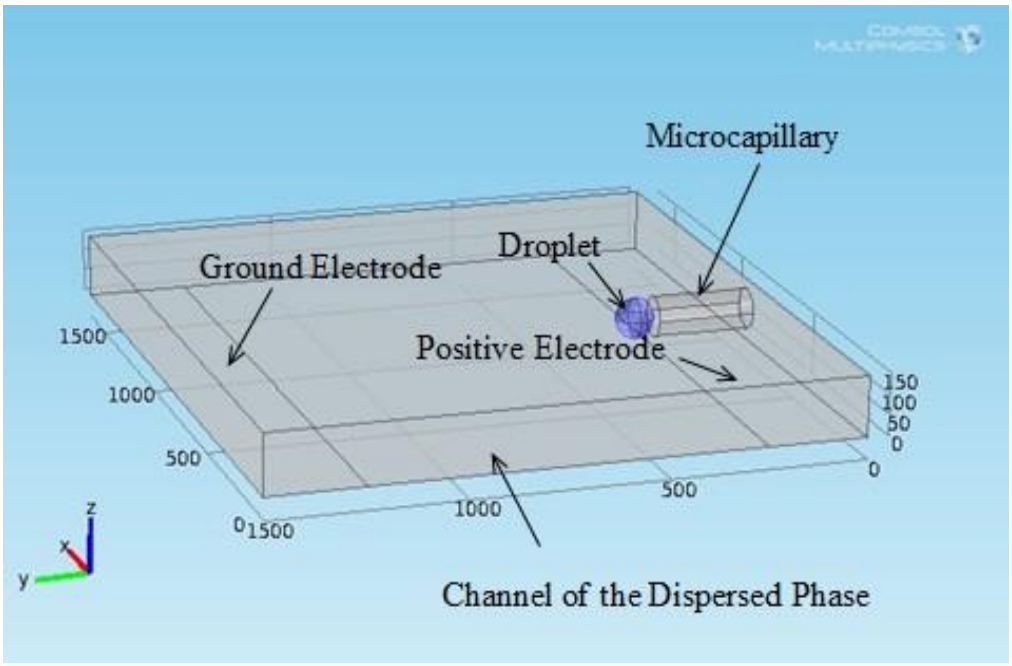

Figure 5.5: *Simulated geometry*

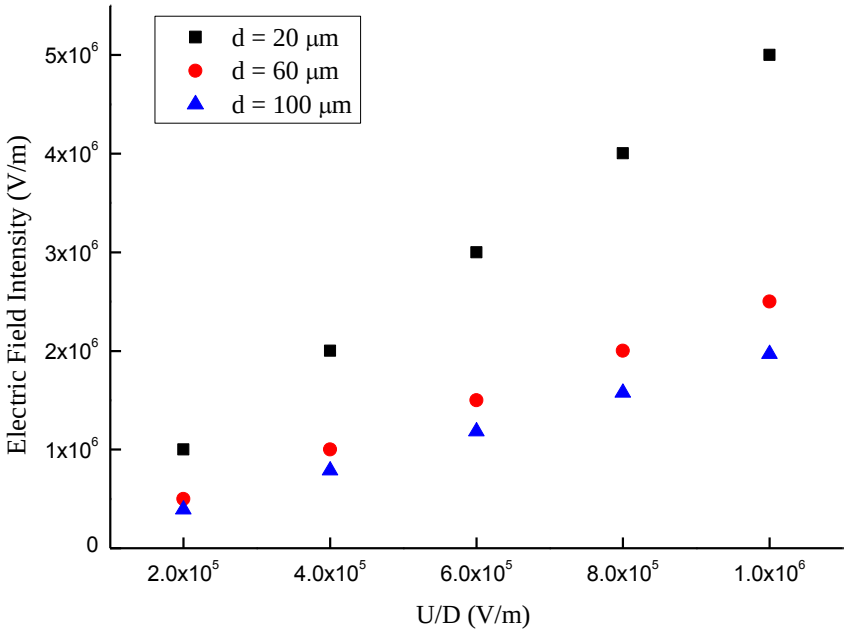

Figure 5.6: *Electric field intensity at droplet surface vs. U/D under three droplet diameters*

Linear relation between E_n and $\frac{U}{D}$ can be observed. The E_n can therefore be expressed as:

$$E_n = \frac{U}{D} * g(d) \tag{5-4}$$

To obtain g(d), the data were plotted in the form of $\frac{E_n D}{U}$ vs $\frac{1}{d}$ in **Figure 5.7**.

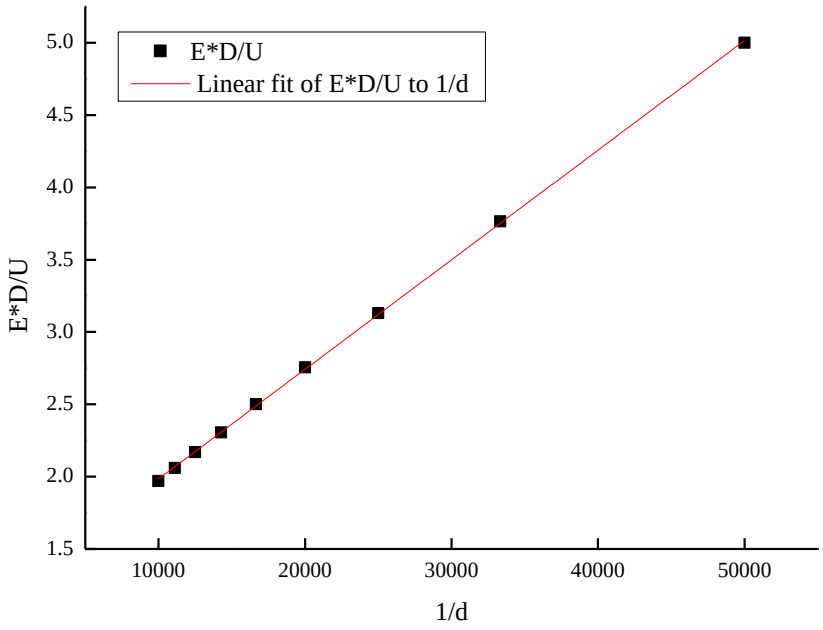

Figure 5.7: *Linear fitting of E*D/U to 1/d in the single-capillary device*

The function is further derived as:

$$\frac{E_n D}{U} = \frac{7.58*10^{-5}}{d} + 1.23 \quad R^2 = 0.9999 \tag{5-5}$$

In our experiments, the continuous flow velocities were: 0.011 m/s, 0.01375 m/s and 0.0165 m/s based on the device geometries and the applied flow rates. The applied potentials ranged from 300 V to 1000 V in steps of 100 V. The density, viscosity, interfacial tension and relative dielectric constant of the paraffin oil are 845 kg/m^3, 12.2 cSt, 0.003 N/m and 2.2,

respectively. By substituting Equation 5-5 into Equation 3-6, the Equation 5-6 is then derived and it can be solved by further substituting the parameters.

$$\frac{\varepsilon\left[\left(\frac{7.58*10^{-5}}{d}+1.23\right)*\frac{U}{D}\right]^2}{8}\pi d^2 + 3\pi\mu V d = \gamma\pi d_c \qquad (5\text{-}6)$$

Figure 5.8 shows the comparison between the experimental results and theoretical results. Three series of data points represent the experimental results. From top to bottom, they represent 10 mL/hour, 12.5 mL/hour and 15 mL/hour. For instance, for the flow rate of 12.5 mL/hour, the droplet size decreases from 140 μm to 55 μm as the potential increase from 0 V to 1000 V. Each data point is the average of 10 droplet samples in this case and the largest standard deviation is lower than 6%. The transition of droplet size is instantaneous with the change in potential and only takes few seconds. The expected droplet diameters from theoretical analysis are also shown. Experimental results are in good agreement with theoretical analysis for all the three flow rates with a maximum difference of 20%.

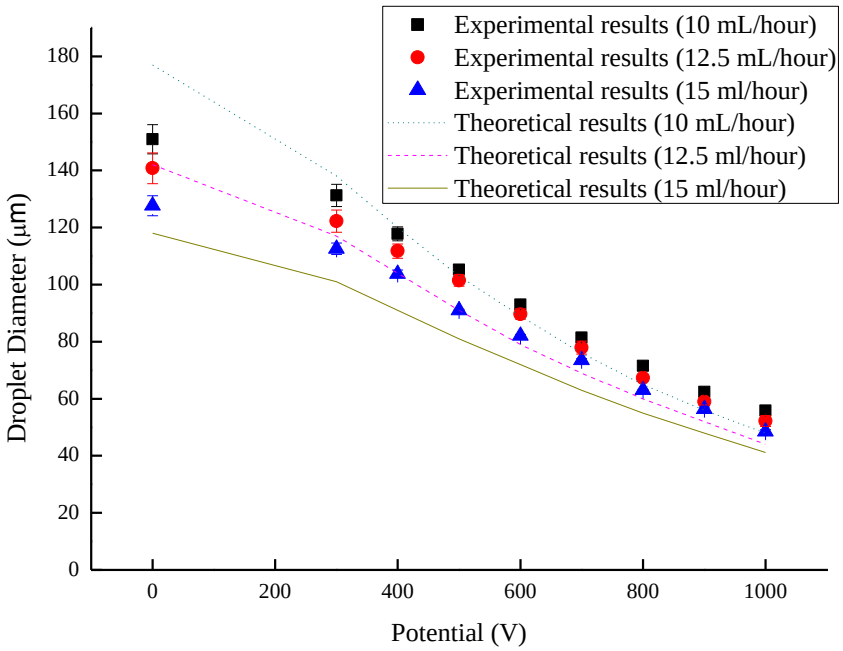

Figure 5.8: *Experimental and theoretical results of droplet size vs. potential (0.01 mL/hour dispersed flow rate) in the single-capillary device*

To further investigate the influence of electrostatic force, the dimensionless number, termed as electric viscous number, is defined and calculated based on the theoretical analysis. It is a ratio between electrostatic force and viscous force is defined as:

$$Ev = \frac{Electrostatic\ force}{Viscous\ force} = \frac{\varepsilon_e \varepsilon_0 {E_n}^2 d}{24 \mu V} \tag{5-7}$$

Where ε_e is the dielectric constant of paraffin oil, ε_0 is the permittivity of vacuum, E_n is the electric field at the surface of droplet, μ is the viscosity of paraffin oil, V is the velocity of paraffin oil and d is the diameter of droplet.

Figure 5.9 illustrates the relation between E_v and the potential at three different continuous flow rates. E_v increases from around 0.2 to around 2 as the potential increases from 300 V to 1000 V. It clearly indicates the dominant force in droplet generating process changes

from viscous force to electro static force as the potential is increased. This result also supports the observation that at low potentials it is the influence of the drag force that determines the droplet size while at high potential it is the electric field that controls the droplet size.

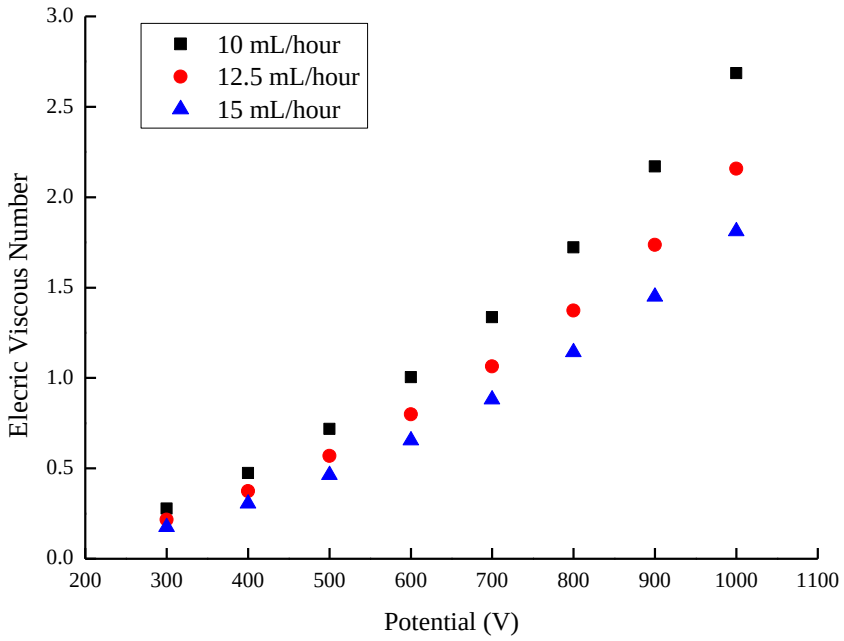

Figure 5.9: *Electric viscous number in the single-capillary device (0.01 mL/hour dispersed flow rate)*

5.3.2 Effect of the Continous Phase Flow Rate

The experimental results are illustrated in **Figure 5.10**. The droplet size decreases with the increase of continuous flow rate. As the flow rate increases from 10 mL/hour to 12.5 mL/hour, the droplet size decreases from 150 μm to 130 μm at 0 V while it decreases only from 55 μm to 52 μm at 1000 V. Each data point is the average of 10 droplet samples in this case and the largest standard deviation is lower than 6%. The change of the droplet size is more prominent at low voltage then at high voltage. In the theoretical model proposed in chapter 3, the increase in the continuous flow rate causes a corresponding increase in the viscous force (drag force)

(Equation 3-3) between the continuous phase and dispersed phase, which would ultimately affect the droplet generating process. Theoretical analysis plotted in **Figure 5.10** shows a similar trend with experimental results, that the droplet size changes more significantly at high voltage. This trend could be attributed to the greater dominance of electrostatic force as the voltage increases. However, there is a notable difference between experimental and theoretical results at 0 V. Theoretically the size changes more significantly than observed in experiments. This is possibly because we assumed a homogenous flow velocity of the continuous phase in the vicinity of the capillary and complexity of flow field near the capillary was ignored. Typically, a boundary layer would form near the capillary and reduce the relative velocity difference locally which would affect the drag forces.

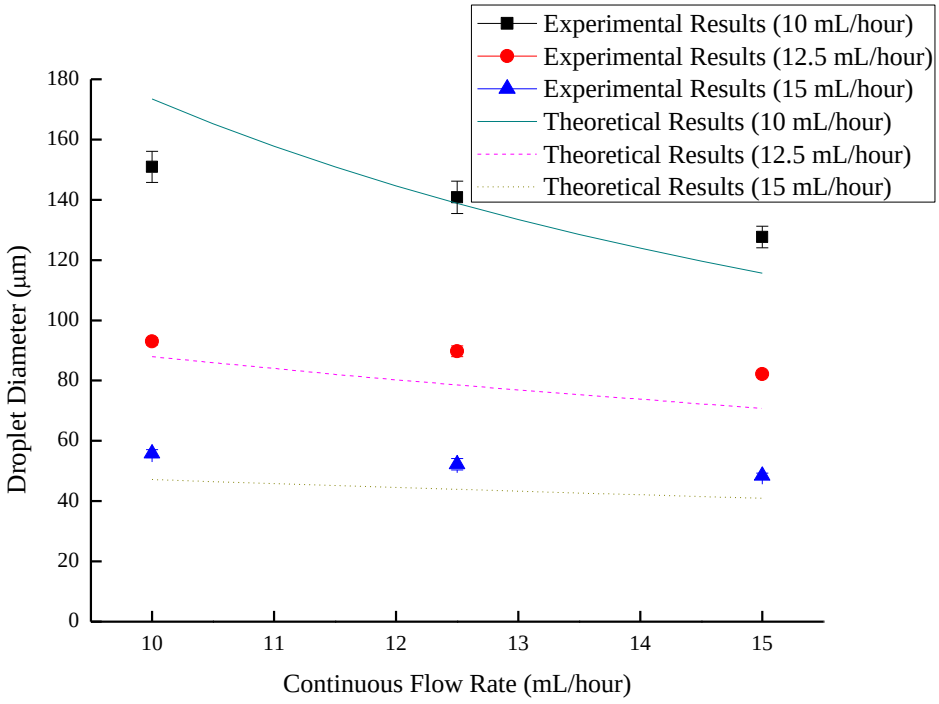

Figure 5.10: *Droplet size vs. continuous flow rate in the single-capillary device (0.01 mL/hour dispersed flow rate)*

To further understand the effect of the continuous phase flow rate on the droplet generation, the capillary number which describes the relation between interfacial tension and viscous force is calculated as:

$$Ca = \frac{\mu V}{\gamma} \tag{5-8}$$

Where μ is the viscosity of paraffin oil, V is the velocity of paraffin oil and γ is the inter tension between two phases. Substituting all parameters into Equation 5-8, *Ca* is ~ 0.01 in our experiments, which falls in the region of dripping mode of droplet generation [10]. In the dripping droplet generation, the formed droplet is spherical and the generation process is mainly determined by the capillary force.

5.3.3 Effect of the Dispersed Phase Flow Rate

Figure 5.11 shows the relation between dispersed flow rate and droplet size at 15 mL/hour continuous flow rate. The three lines represent the droplet size under three different potentials (0 V, 600 V and 1000 V). Little variance of droplet size to the dispersed flow was observed in this figure. For instance, at 0 V, the droplet size slight increases from 128 μm to 133 μm as the dispersed flow rate increases from 0.01 mL/hour to 0.05 mL/hour. Each data point is the average of 10 droplet samples in this case and the largest standard deviation is lower than 6%. In our simplified droplet generating model (Equation 3-6) a droplet is generated when the electrostatic and the viscous forces overcome the surface tension forces at the capillary tip. Since the dispersed flow velocity is low compared to the continuous flow when the droplet is about to detach, the dispersed flow rate does not have much effect on the drag force, which therefore results in the slight change of droplet size.

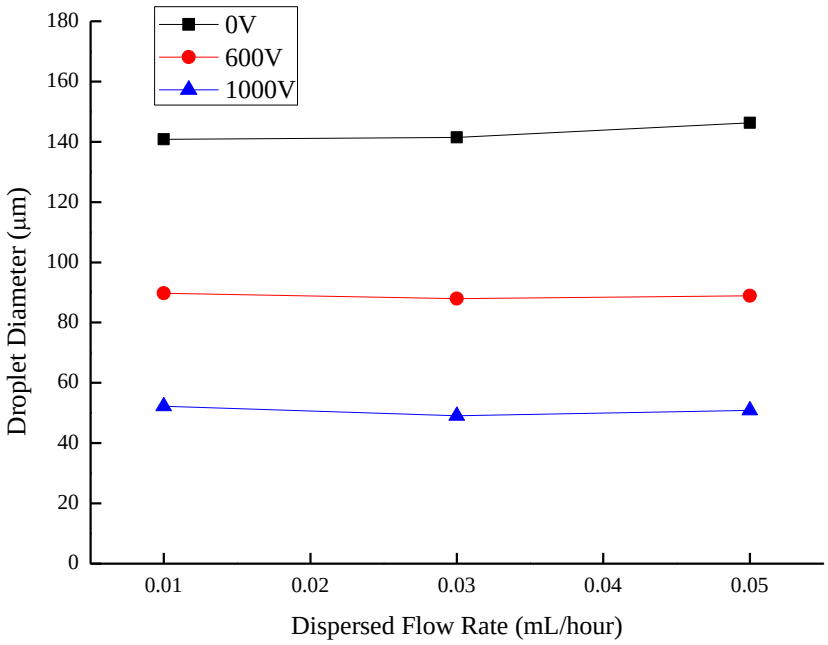

Figure 5.11: *Droplet size vs. dispersed flow rate in the single-capillary device (15 mL/hour continuous flow rate)*

5.3.4 Effect of the Electric Field Distribution

In addition to the parallel electrode configuration proposed in section 5.3.1, the point and plane electro configuration is evaluated in this section. The point to plane electrode configuration was considered to produce non uniform electric field and was not favoured for the configuration containing multiple parallel nozzles. However, the uniformity of the electric field is not important in the single-capillary device and therefore this distribution is characterized here further.

Similar to section 5.3.1, the theoretical solution of droplet size of this electric field can be derived from Equation 3-6. Instead of using the multi-physics simulation, the electric field intensity at the surface of droplet E_n can be empirically derived as [65]:

$$\mathrm{E}_n = \frac{\sqrt{2}U}{r'\ln(\frac{4D'}{r'})} \tag{5-9}$$

$$r' = 1.2r - 0.2R \tag{5-10}$$

$$D' = D - 2r \tag{5-11}$$

Where D is the distance between two electrodes, r is the radius of droplet and R is the inner diameter of the capillary tubing. Substituting Equation 5-9 – 5-11 into Equation 3-6, the Equation 5-12 is derived, and then analysis solution can be obtained by solving Equation 5-12.

$$\frac{\varepsilon\left[\left(\frac{\sqrt{2}U}{(1.2r-0.2R)\ln(\frac{4(D-2r)}{1.2r-0.2R})}\right)\right]^2}{8}\pi d^2 + 3\pi\mu V d = \gamma\pi d_c \tag{5-12}$$

Figure 5.12 illustrates both experimental and theoretical results in the point to plane electrode configuration. The droplet size decreases gradually from 140 μm to 110 μm as the potential increases from 0 V to 200 V while decreases more sharply from 110 μm to 50 μm as potential increases from 200 V to 280 V. Each data point is the average of 10 droplet samples in this case and the largest standard deviation is lower than 6%. The theoretical results show a similar trend. Although both geometries can generate the droplet ranging from 50 μm to 140 μm, the potential required to generate droplets of a particular size is lower in the point and plane electrode configuration than in the parallel electrode configuration. Moreover, the droplet size is more sensitive to the potential in the point to plane electrode configuration than in the parallel electrode configuration. As explained in chapter 3, the point to plane electrode configuration is able to produce higher electric field intensity than the parallel electrode configuration when the same potential is applied. This property makes it an ideal choice for the single-capillary device.

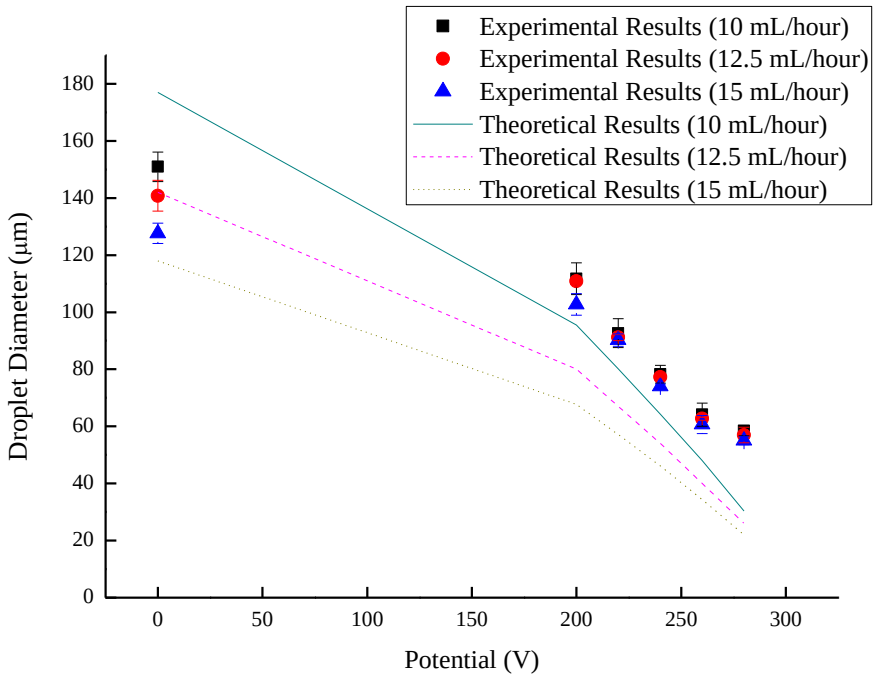

Figure 5.12: *Experimental and theoretical results of the point to plane electrode configuration in the single-capillary device (0.01 mL/hour dispersed flow rate)*

5.4 Characterization of Parallel Droplet Generating Device

Parallelization of the droplet generating process is performed by inserting more capillaries into the grooves of the PDMS microchannels. In this research, three and five capillary devices are characterized to test the function of the parallelization of the device. Successful functioning of these devices can ensure larger scale parallelization in the future.

5.4.1 Characterization of the Three-Capillary Device

The three-capillary device was characterized, with one capillary installed in the central groove and two capillaries installed in the side grooves (**Figure 5.13**). Similar to one capillary device, electrically control of droplet size can also be achieved for the three-capillary device (**Figure 5.14**). The droplet size decreases as potential increases and there is a consistent trend for

various continuous flow rates (10 mL/hour, 12.5 mL/hour, 15 mL/hour) and dispersed flow rates (0.03 mL/hour, 0.09 mL/hour, 0.15 mL/hour).

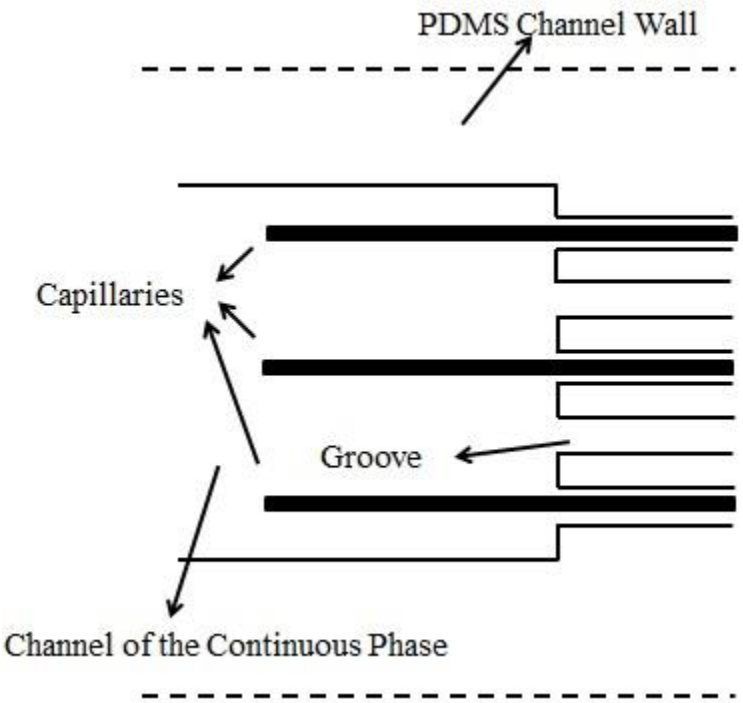

Figure 5.13: *Schematic of the three-capillary device*

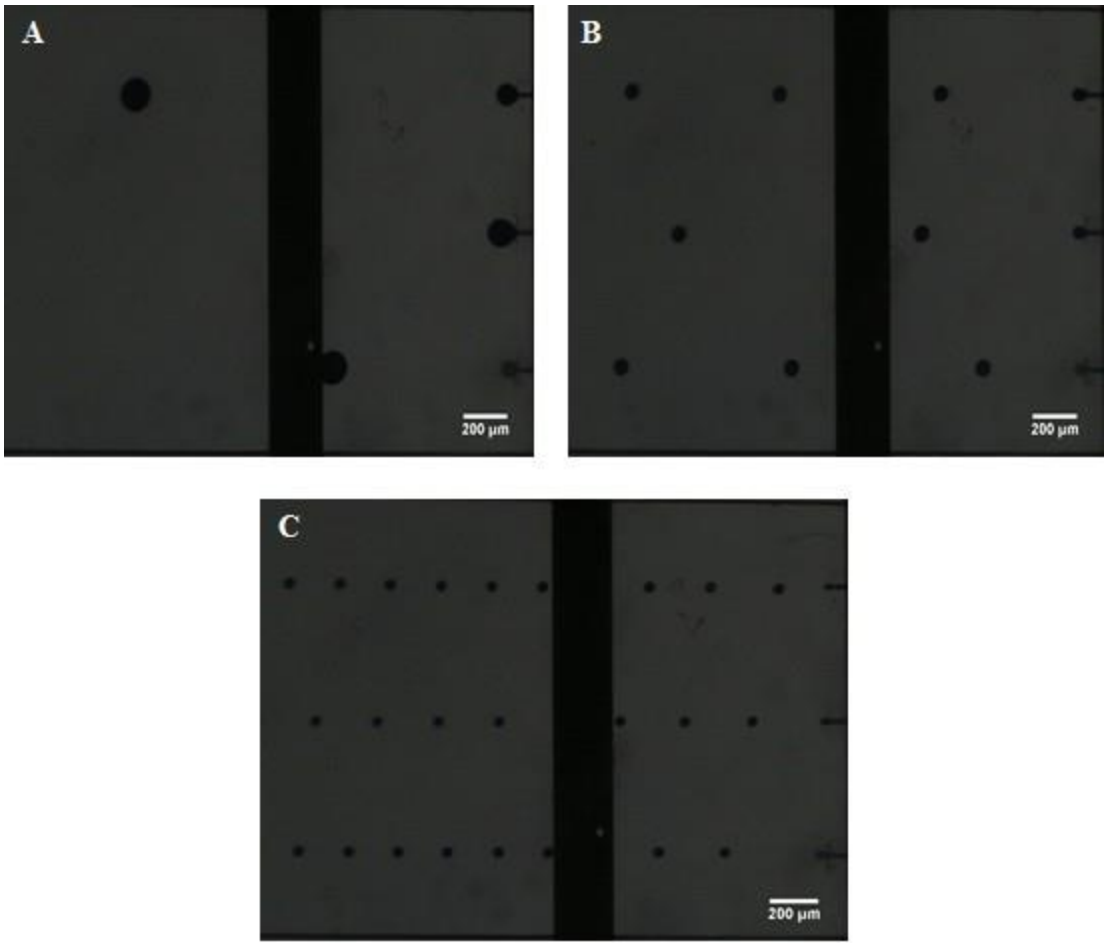

Figure 5.14: *Droplet generation under potential of: A) 400 V; B) 600 V; C) 1000 V (0.03 mL/hour dispersed flow rate, 10 mL/hour continues flow rate) in the three-capillary device*

Applying the same analysis as in section 5.3, the relation between the potential and the electric field intensity at droplet surface (Equation 5-13) was obtained by multi-physics simulation and linear fitting:

$$\frac{E_n D}{U} = \frac{8.22*10^{-5}}{d} + 1.01 \quad R^2 = 0.9995 \tag{5-13}$$

By substituting Equation 5-13 into Equation 3-6, Equation 5-14 was derived and the theoretical solutions were obtained.

$$\frac{\varepsilon\left[\left(\frac{8.22*10^{-5}}{d}+1.01\right)*\frac{U}{D}\right]^2}{8}\pi d^2 + 3\pi\mu V d = \gamma\pi d_c \tag{5-14}$$

Figure 5.15 shows both the experimental results and theoretical calculations. The three lines represent the theoretical results for three different continuous flow rates which are 10 mL/hour, 12.5 mL/hour and 15 mL/hour from top to bottom. Three series of data points represent the experimental results for three different continuous flow rates and they are in the same descending order with theoretical solutions. For instance, at the flow rate of 12.5 mL/hour, the droplet size decreases from 123 μm to 38 μm as the potential increases from 0 V to 1000 V. Each data point is the average of 30 droplet samples in this case and the largest standard deviation is lower than 4%. Experimental results appear to be similar with the theoretical solutions for all the three flow rates, and the maximum difference is lower than 30%.

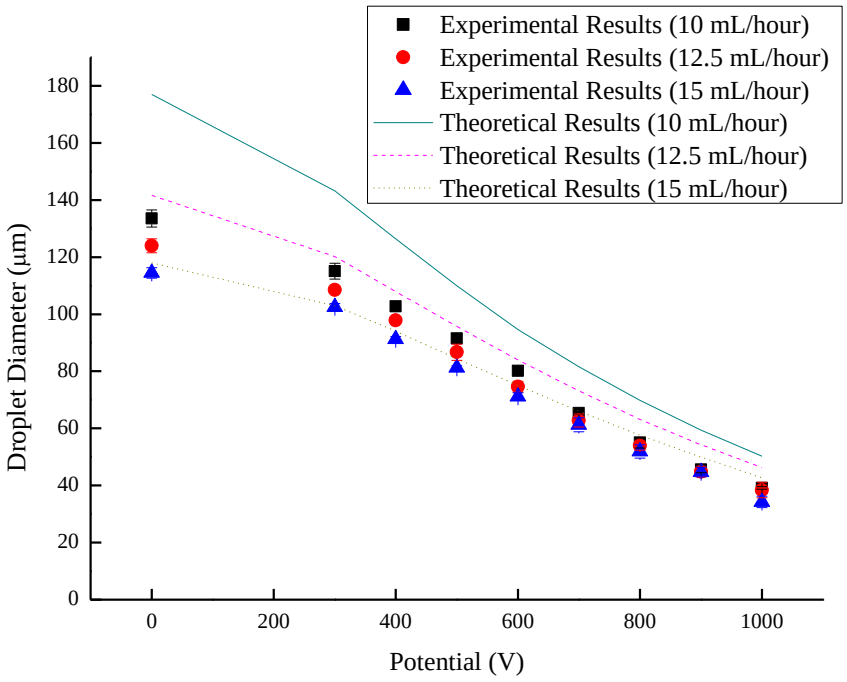

Figure 5.15: *Experimental and theoretical results of droplet size vs. potential (0.03 mL/hour dispersed flow rate) in the three-capillary device*

The *Ev* number is presented in **Figure 5.16**. Similar to the single-capillary device, *Ev* is ~ 0.2 when potential is 300 V and it is ~ 2 when potential is 1000 V, which further confirms the

conclusion. Difference between the theoretical and experimental results could be attributed to the non-uniformity of flow filed distribution as well as the geometry of the capillaries tips.

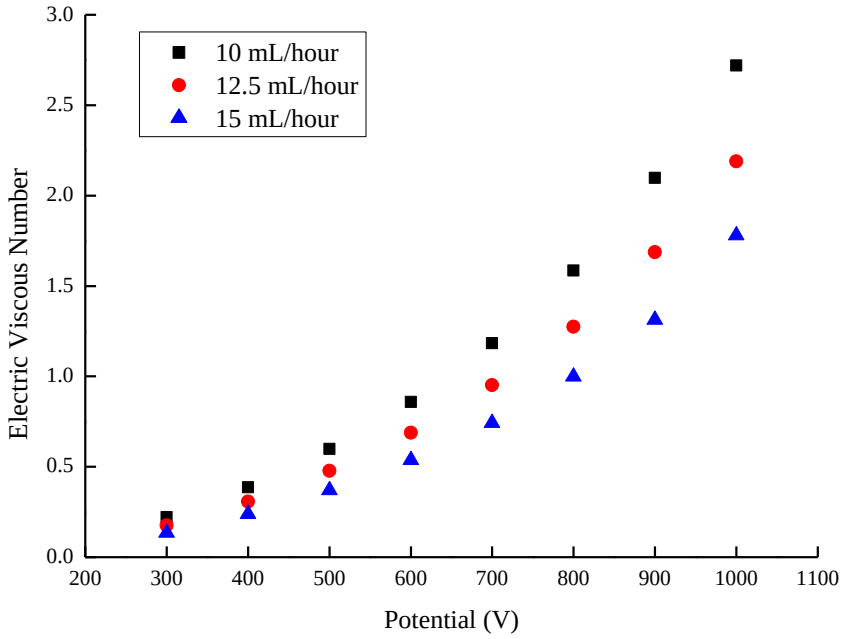

Figure 5.16: *Electric viscous number in three-capillary device (0.03 mL/hour dispersed flow rate)*

Figure 5.17 and **Figure 5.18** show both the influence of the continuous flow rate and the dispersed flow rate. Each data point is the average of 30 droplet samples in this case and the largest standard deviation is lower than 4%. The dispersed flow rates of the three-capillary device was set as 0.03 mL/hour (0.01 mL/hour per capillary), 0.09 mL/hour (0.03 mL/hour per capillary) and 0.15 mL/hour (0.05 mL/hour per capillary) in accordance to the dispersed flow rate of the single-capillary device. The continuous flow rates were also the same as that in the single-capillary device. It should be noted here that the experimental results obtained here are nearly the same with the single-capillary device due to the similarity of the flow field and the electric field distribution. This is important as it suggests that scaling to more capillaries will not

affect the droplet generation in term of its dynamic control. The change of the droplet size is more prominent at lower voltage than high voltage. The droplet size decreases from 140 µm to 120 µm at 0 V but almost remains unchanged at 40 µm at 1000 V. The increase of the continuous flow rate reduces the droplet size due to the increase of the drag force. This effect diminishes as the potential increases, which could be attributed to the dominance of the electrostatic force at higher potentials. As the dispersed flow rate increases, the droplet size increases slightly. One reason could be the reduction in the relative velocity at the interface with the continuous phase. However, since the dispersed phase velocity is much smaller than the continuous phase velocity, the change in dispersed phase velocity is not expected to have much effect.

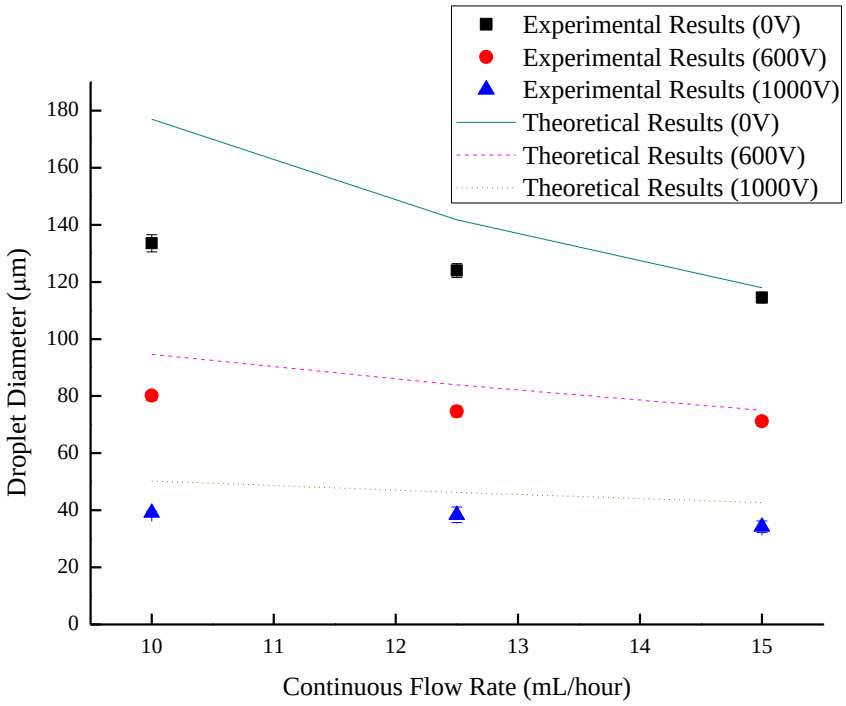

Figure 5.17: *Droplet size vs. continuous flow rate in the three-capillary device (0.03 mL/hour dispersed flow rate)*

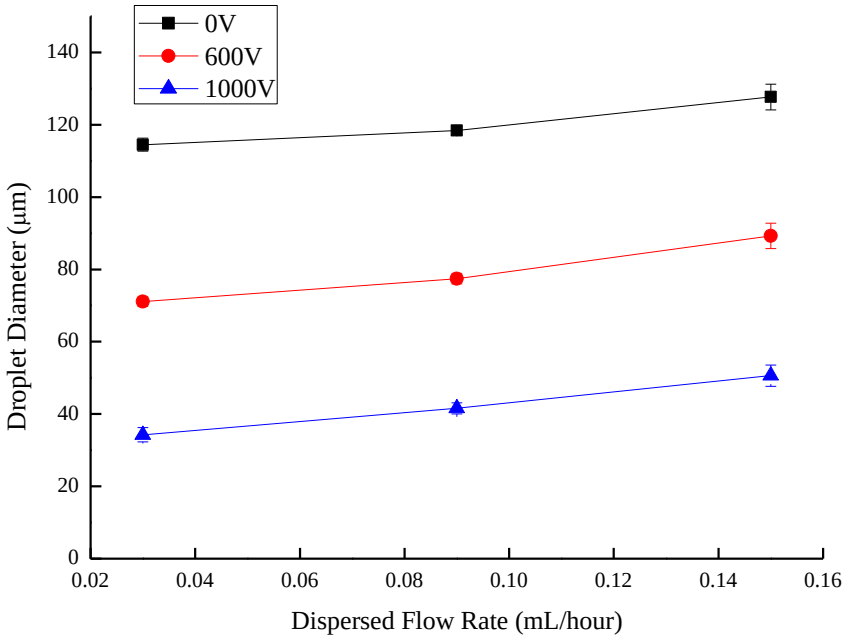

Figure 5.18: *Droplet size vs. dispersed flow rate in the three-capillary device (15 mL/hour continuous flow rate)*

The largest difference between the droplet sizes in different capillaries is lower than 10% and the standard deviation of the droplet size is lower than 4% based on the measuring of 30 droplet samples, validating the monodispersed droplet generating of the three-capillary devices.

5.4.2 Characterization of the Five-Capillary Device

The five-capillary device is also characterized in this section, with capillaries installed in every groove of the device (**Figure 5.19**).

As illustrated in **Figure 5.20,** the droplet size decreases as potential increases and there is a consistent trend for various continuous flow rates (10 mL/hour, 12.5 mL/hour, 15 mL/hour) and dispersed flow rates (0.01 mL/hour, 0.03 mL/hour, 0.05 mL/hour).

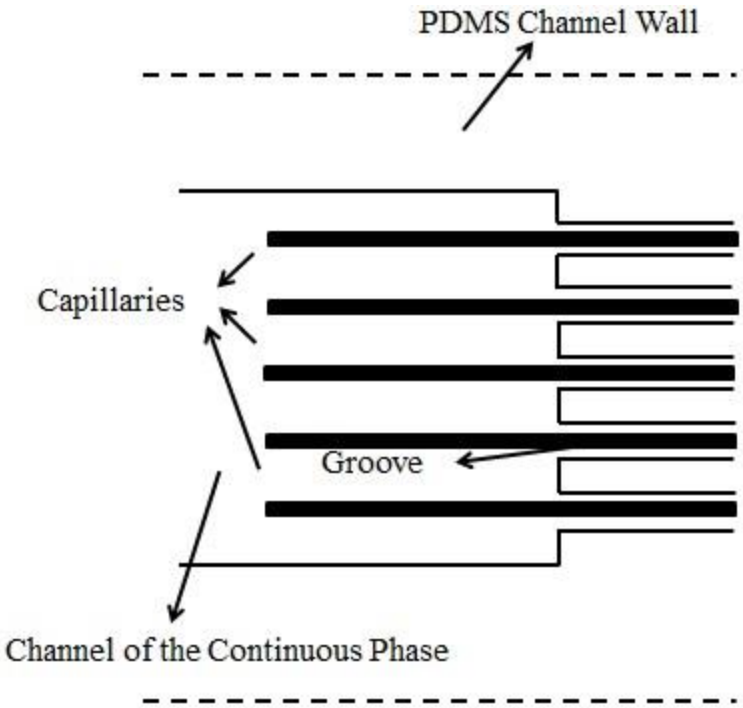

Figure 5.19: *Schematic of the five-capillary device*

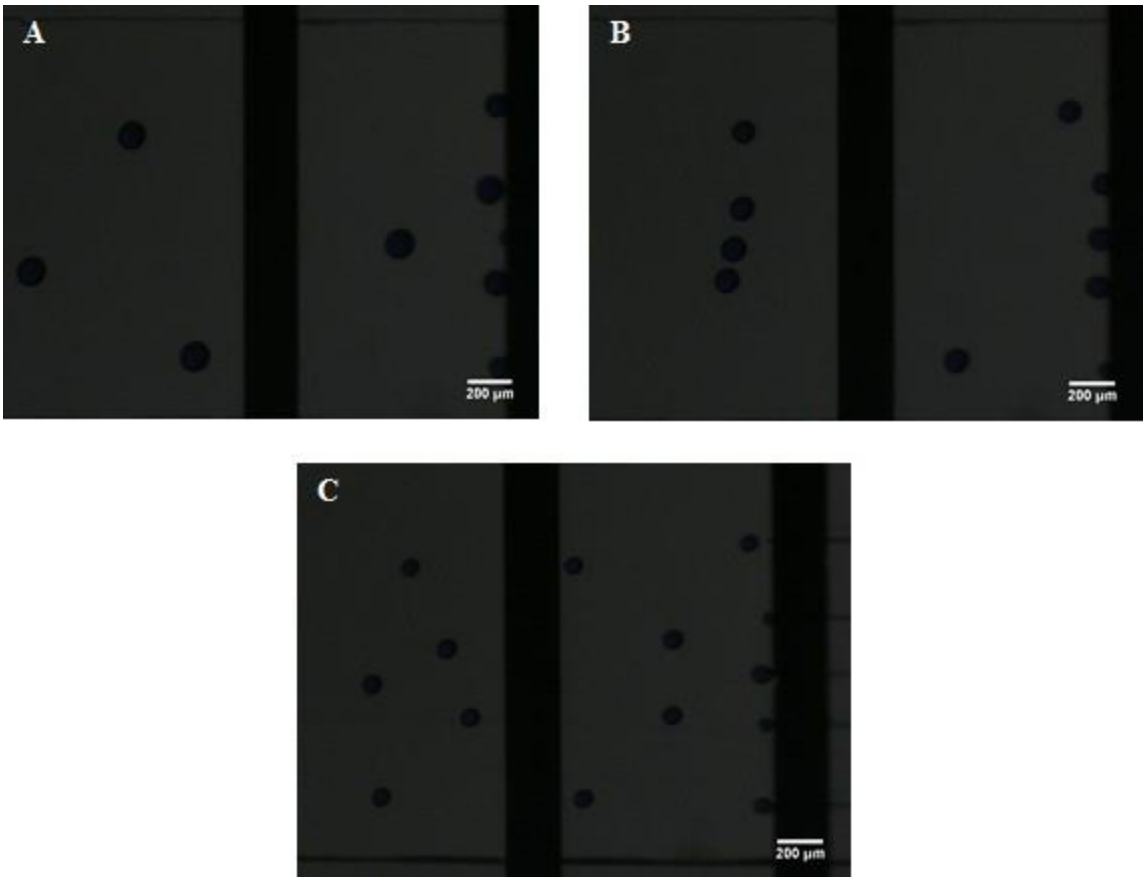

Figure 5.20: *Droplet generation under potential of: A) 400 V; B) 600 V; C) 800 V (0.05 mL/hour dispersed flow rate, 10 mL/hour continues flow rate) in five- capillary device*

Applying the same analysis as in section 5.3, the relation between the potential and the electric field intensity at droplet surface (Equation 5-13) was obtained by multi-physics simulation and linear fitting:

$$\frac{E_n D}{U} = \frac{8.62*10^{-5}}{d} + 0.75 \quad R^2 = 0.995 \tag{5-15}$$

By substituting Equation 5-15 into Equation 3-6, Equation 5-16 was derived, from which the theoretical results were obtained.

$$\frac{\varepsilon\left[\left(\frac{8.62*10^{-5}}{d}+0.75\right)*\frac{U}{D}\right]^2}{8}\pi d^2 + 3\pi\mu V d = \gamma\pi d_c \tag{5-16}$$

The influence of the potential on droplet size is similar to the single and three-capillary device. Each data point is the average of 50 droplet samples in this case and the largest standard deviation is lower than 6%. The curve becomes less steep compared to the single-capillary device with the parallel electrode configuration as illustrated in **Figure 5.21**, which indicates to the decrease of the controllability of the electric field in the five-capillary device. To explain this, *Ev* number is calculated and illustrated in **Figure 5.22**. The *Ev* number at 900 V are 1.97 (10 mL/hour), 1.61 (12.5 mL/hour) and 1.36 (15 mL/hour), lower than those in the single-capillary device. The decrease of *Ev* number demonstrates the reduced dominance of electrostatic force at high potentials in the five-capillary device. The theoretical prediction, though still effective, becomes less precise with the largest difference of 50% compared to the single and the three-capillary devices. Several reasons could possibly cause the difference between the theoretical and experimental results: firstly, as more capillaries being inserted, the flow field changes. Secondly, as the distance between droplet streams become shorter, the influence of the repelling force between adjacent droplet streams becomes more important. These reasons remain to be further investigated in future research.

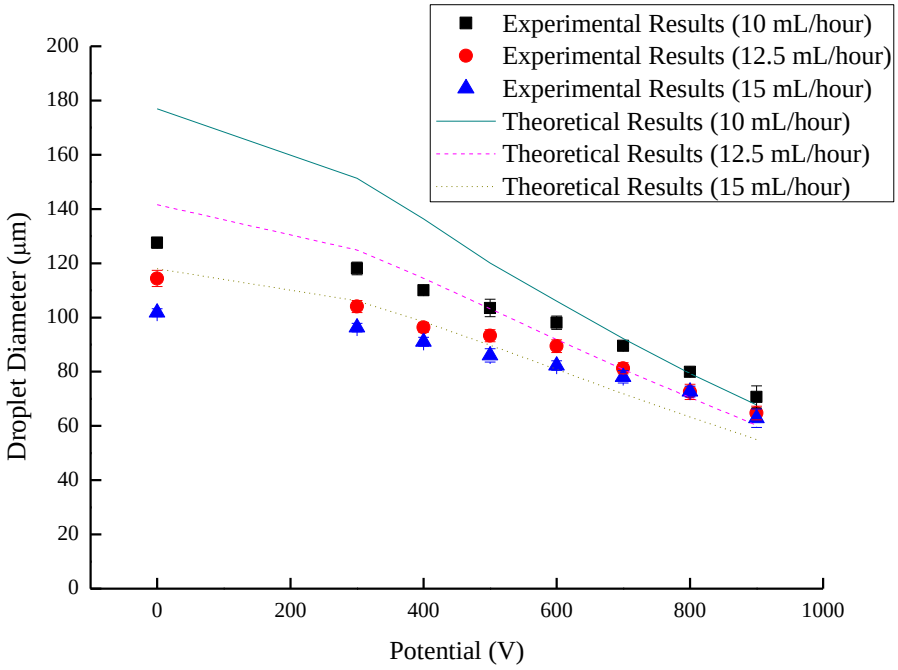

Figure 5.21: *Experimental and theoretical results of droplet size vs. potential (0.05 mL/hour dispersed flow rate) in the five-capillary device*

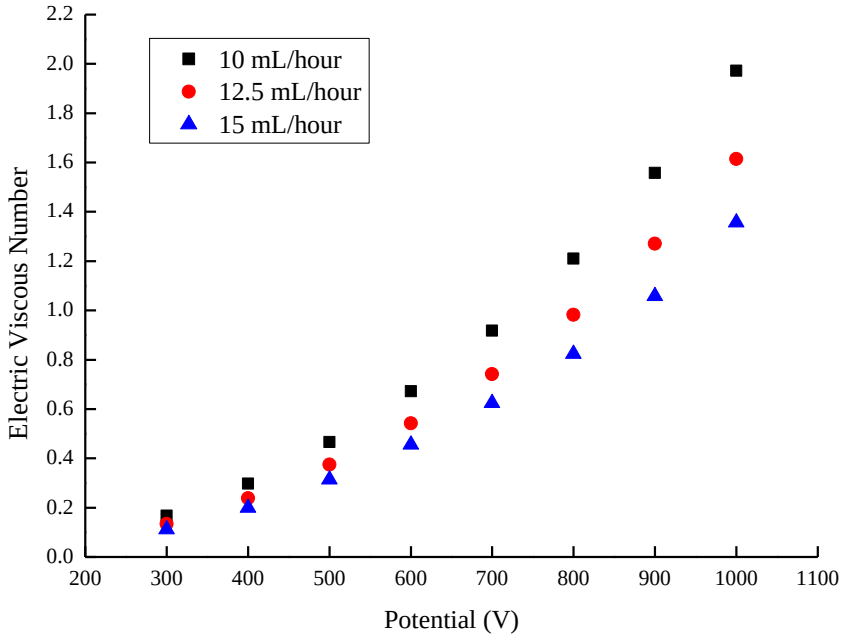

Figure 5.22: *Electric viscous number in the five-capillary device (0.05 mL/hour dispersed flow rate)*

The influence of continuous flow is illustrated in **Figure 5.23**. The results are similar to those observed in the single-capillary and the three-capillary devices. Slight decrease of droplet size with the increase of continuous flow rate is expected from the theoretical results. As explained in previous section, this could be attributed to the geometry of the tip of the capillary which reduces the change of flow field.

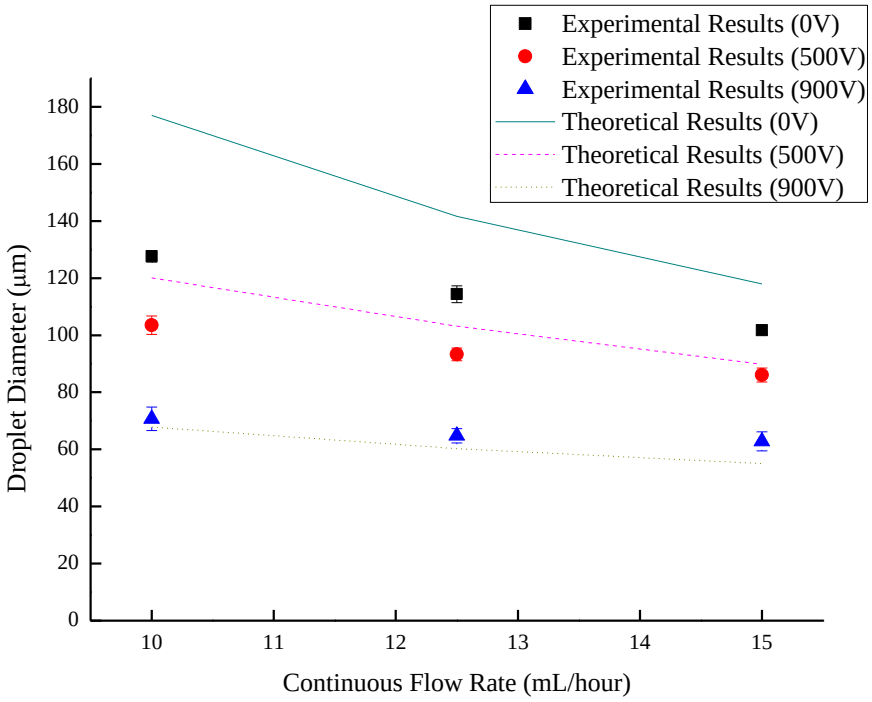

Figure 5.23: *Droplet size vs. continuous flow rate in the five-capillary device (0.05 mL/hour dispersed flow rate)*

To achieve a higher throughput of droplet generation, the dispersed flow rate were set as: 0.05 mL/hour (0.01 mL/hour per capillary); 0.25 mL/hour (0.05 mL/hour per capillary) and 0.75 mL/hour (0.15 mL/hour per capillary). **Figure 5.24** displays the graph of droplet size vs dispersed flow rate under different potentials. Each data point is the average of 50 droplet samples in this case and the largest standard deviation is lower than 6%. The droplet size increases from 101 μm to 126 μm as dispersed flow rate increases from 0.05 mL/hour to 0.75 mL/hour without applied potential and increases from 73 μm to 97 μm with 800 V potential. This clearly indicates that the flow rate of the dispersed phase becomes important determinant of the droplet size as it becomes comparable to the flow rate of the continuous phase. This can be explained by the tangible reduction in the relative velocity between the continuous and the dispersed phases with the increase of the dispersed phase velocity. However, since the flow field

within the droplet is complex, it is not easy to obtain the actual velocity at the surface of the droplet and make a theoretical prediction of the influence of dispersed phases, thus remaining the further investigation of this aspect.

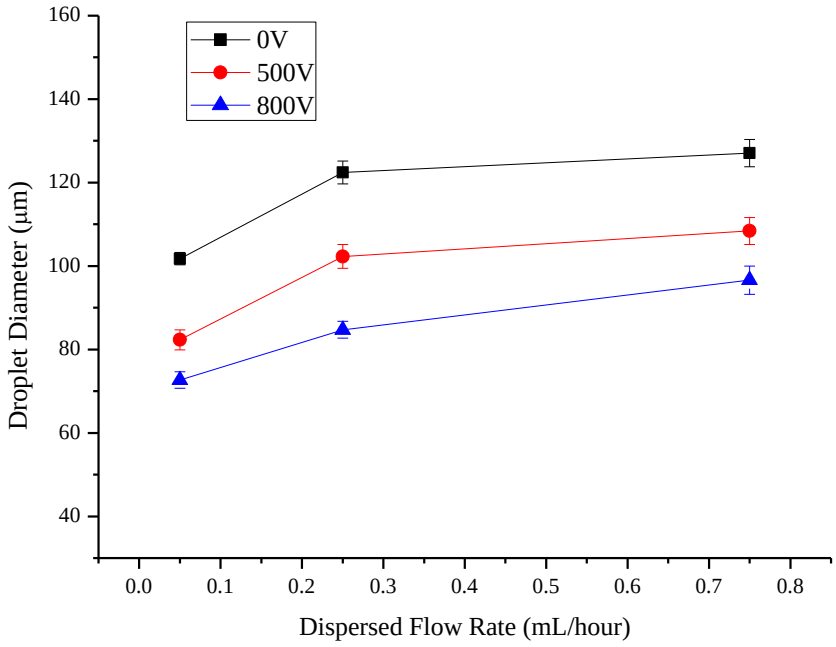

Figure 5.24: *Droplet size vs. dispersed flow rate in the five-capillary device (15 mL/hour continuous flow rate)*

The largest difference between the droplet sizes in different capillaries is lower than 20%, and the standard deviation of the droplet size is lower than 6% in the five-capillary device, demonstrating the success of parallelization.

5.5 Summary

In this chapter, the designed device proved to be reusable (can be used for 2 to 3 times) and repeatable (the largest difference of droplet size between different devices for all the situations is ~20%) for electrically controlled droplet generation. The influences of the potential,

the flow rate of the continuous flow, the flow rate of the dispersed flow and the difference electrode configuration on the device were characterized in detail. The experimental results were in good agreement with the theoretical solutions. Moreover, the parallelization of droplet generation in this device was demonstrated. The standard deviation of droplet size is lower than 4% for the three-capillary device and lower than 6% in the five-capillary device, showing the reliability and scalability of parallelization.

Chapter 6 Contributions &Future Work

6.1 Contributions

The contribution of this research can be categorized into three parts: First, the device is able to achieve the fast and dynamic control of droplet size by adjusting the DC potentials. A theory was proposed to predict the droplet size with different potentials as well as flow rates. Secondly, the parallelization of droplet generation is realized such that the difference between droplet sizes at different capillaries is fairly low. Thirdly, the low cost fabrication process was developed for this device.

6.1.1 Electrically Control of Droplet Size

One of the key features of this device is the ability to control the size of the droplets dynamically. By varying the potential from 0 V to 1000 V, it is possible to change the droplet size from 150 μm to 40 μm. Compared to the control methods by changing the flow rate, this device demonstrates its ability to change the droplet size far more quickly. The transition of droplet size only takes few seconds in this method while takes more than half an hour in the traditional method [61]. Moreover, the theoretical analysis of electrically controlled droplet generating process was presented and the theoretical results show a good agreement with experimental results.

6.1.2 Parallelization

Another notable contribution of this device is that the parallelization of droplet generation is achieved along with the electrically control. By placing three and five

microcapillaries into the channel for oil phase, the flow rate can be increased 3-5 times as compared to a single-capillary device. Throughput of 0.75 mL/hour rate of droplet generation has been actually achieved. It has achieved better or similar performance with existing PDMS based parallel droplet generating devices [35][56][66]. The droplet sizes are uniform at different applied potentials and flow rates. The standard deviation of droplet size is lower than 4% in the three-capillary device and it is lower than 6% in the five-capillary device, showing the capability of generating monodispersed droplet.

6.1.3 Low Cost Fabrication

Simple operation and low cost of making the devices are the keys to successful commercial uptake of this technology. By using microcapillaries and embedding them in cast microchannels, the cost of manufacture is reduced while the precision needed is maintained. Compared with the working done by van Dijke et al. [3] and Nisisako et al. [34] in which precise machining and DRIE technology were used, the fabrication of this device is low cost. Moreover, the device is fabricated by low cost materials such as PDMS, glass slide and microcapillaries which further decreases the cost of the device.

6.2 Future Work

In addition to the work have done in this research, there are still some aspects remaining to be further developed and investigated.

Characterization of AC potential

The influence of DC potential has been fully investigated in this research, while remaining the AC electric field to be investigated. One possible way is to accurately control both the size

and frequency of droplet generation by varying the AC potential and frequency. However, revisions in the design might be needed due to the instability of AC field.

Higher throughput of droplet generation

Although the largest droplet production rate of 0.75 mL/hour has been achieved in this device, improvement still needs to be made to realize the industrial production rate (~ 10 mL/hour). By enlarging the channel for oil phase as well as changing the placement of the capillaries, more capillaries can be placed into the channel and higher productivity will be therefore achieved.

Application of the device

In this research, DI water and paraffin oil were applied to characterize the device, proved the repeatability and robust working of the device. Beyond that, a demonstration of the use of this device in an actual application such as chemical synthesis, biology analysis can be performed. The adaptability of the chemicals to the device as well as the electric field should be carefully considered. The re-characterization of the device might be needed.

List of References

[1] S. L. Anna, N. Bontoux, and H. A. Stone, "Formation of dispersions using 'flow focusing' in microchannels," *Applied Physics Letters*, vol. 82, no. 3, p. 364, Jan. 2003.

[2] T. Nisisako, T. Torii, and T. Higuchi, "Droplet formation in a microchannel network," *Lab on a chip*, vol. 2, no. 1, pp. 24–6, Mar. 2002.

[3] K. van Dijke, R. de Ruiter, K. Schrö en, and R. Boom, "The mechanism of droplet formation in microfluidic EDGE systems," *Soft Matter*, vol. 6, no. 2, p. 321, Jan. 2010.

[4] A. Huebner, S. Sharma, M. Srisa-Art, F. Hollfelder, J. B. Edel, and A. J. Demello, "Microdroplets: a sea of applications?," *Lab on a chip*, vol. 8, no. 8, pp. 1244–54, Aug. 2008.

[5] R. Zengerle, S. Kluge, M. Richter, and A. Richter, "A bidirectional silicon micropump," in *Proceedings IEEE Micro Electro Mechanical Systems*, 1995, p. 19.

[6] H. T. G. van Lintel, F. C. M. van De Pol, and S. Bouwstra, "A piezoelectric micropump based on micromachining of silicon," *Sensors and Actuators*, vol. 15, no. 2, pp. 153–167, Oct. 1988.

[7] D. Mark, S. Haeberle, G. Roth, F. von Stetten, and R. Zengerle, "Microfluidic lab-on-a-chip platforms: requirements, characteristics and applications," *Chemical Society reviews*, vol. 39, no. 3, pp. 1153–82, Mar. 2010.

[8] H. A. Stone, A. D. Stroock, and A. Ajdari, "ENGINEERING FLOWS IN SMALL DEVICES," *Annual Review of Fluid Mechanics*, vol. 36, no. 1, pp. 381–411, Jan. 2004.

[9] H. Song, D. L. Chen, and R. F. Ismagilov, "Reactions in droplets in microfluidic channels," *Angewandte Chemie (International ed. in English)*, vol. 45, no. 44, pp. 7336–56, Nov. 2006.

[10] H. Gu, M. H. G. Duits, and F. Mugele, "Droplets formation and merging in two-phase flow microfluidics," *International journal of molecular sciences*, vol. 12, no. 4, pp. 2572–97, Jan. 2011.

[11] B. Vogelstein, "Digital PCR," *Proceedings of the National Academy of Sciences*, vol. 96, no. 16, pp. 9236–9241, Aug. 1999.

[12] M. Baker, "Clever PCR: more genotyping, smaller volumes," *Nature Methods*, vol. 7, no. 5, pp. 351–356, May 2010.

[13] V. Taly, D. Pekin, A. El Abed, and P. Laurent-Puig, "Detecting biomarkers with microdroplet technology," *Trends in molecular medicine*, vol. 18, no. 7, pp. 405–16, Jul. 2012.

[14] C. Martino, M. Zagnoni, M. E. Sandison, M. Chanasakulniyom, A. R. Pitt, and J. M. Cooper, "Intracellular protein determination using droplet-based immunoassays," *Analytical chemistry*, vol. 83, no. 13, pp. 5361–8, Jul. 2011.

[15] R. Seemann, M. Brinkmann, T. Pfohl, and S. Herminghaus, "Droplet based microfluidics," *Reports on progress in physics. Physical Society (Great Britain)*, vol. 75, no. 1, p. 016601, Jan. 2012.

[16] H. Song, J. D. Tice, and R. F. Ismagilov, "A microfluidic system for controlling reaction networks in time," *Angewandte Chemie (International ed. in English)*, vol. 42, no. 7, pp. 768–72, Mar. 2003.

[17] L. R. B. Kesselman, S. Shinwary, P. R. Selvaganapathy, and T. Hoare, "Synthesis of monodisperse, covalently cross-linked, degradable 'smart' microgels using microfluidics," *Small (Weinheim an der Bergstrasse, Germany)*, vol. 8, no. 7, pp. 1092–8, Apr. 2012.

[18] B. Zheng, J. D. Tice, and R. F. Ismagilov, "Formation of droplets of alternating composition in microfluidic channels and applications to indexing of concentrations in droplet-based assays," *Analytical chemistry*, vol. 76, no. 17, pp. 4977–82, Sep. 2004.

[19] M. K. Yadav, C. J. Gerdts, R. Sanishvili, W. W. Smith, L. S. Roach, R. F. Ismagilov, P. Kuhn, and R. C. Stevens, "In situ data collection and structure refinement from microcapillary protein crystallization," *Journal of applied crystallography*, vol. 38, no. 6, pp. 900–905, Dec. 2005.

[20] B. Zheng, L. S. Roach, and R. F. Ismagilov, "Screening of protein crystallization conditions on a microfluidic chip using nanoliter-size droplets," *Journal of the American Chemical Society*, vol. 125, no. 37, pp. 11170–1, Sep. 2003.

[21] L. Rayleigh, "On the instability of jets," *Proc. London Math. Soc*, pp. 1873–1878, 1873.

[22] T. R. A. (MIT), "MIT 1.63 Lecture Notes on Fluid Jets," in *MIT Lecture Notes*, 2011, pp. 1–8.

[23] T. Squires and S. Quake, "Microfluidics: Fluid physics at the nanoliter scale," *Reviews of Modern Physics*, vol. 77, no. 3, pp. 977–1026, Oct. 2005.

[24] H. A. Stone, "Dynamics of Drop Deformation and Breakup in Viscous Fluids," *Annual Review of Fluid Mechanics*, vol. 26, no. 1, pp. 65–102, Jan. 1994.

[25] P. Guillot, A. Colin, A. S. Utada, and A. Ajdari, "Stability of a jet in confined pressure-driven biphasic flows at low reynolds numbers," *Physical review letters*, vol. 99, no. 10, p. 104502, Sep. 2007.

[26] L. Shui, J. C. T. Eijkel, and A. van den Berg, "Multiphase flow in microfluidic systems -- control and applications of droplets and interfaces," *Advances in colloid and interface science*, vol. 133, no. 1, pp. 35–49, May 2007.

[27] W. Lee, L. M. Walker, and S. L. Anna, "Role of geometry and fluid properties in droplet and thread formation processes in planar flow focusing," *Physics of Fluids*, vol. 21, no. 3, p. 032103, Mar. 2009.

[28] A. Utada, A. Fernandez-Nieves, H. Stone, and D. Weitz, "Dripping to Jetting Transitions in Coflowing Liquid Streams," *Physical Review Letters*, vol. 99, no. 9, p. 094502, Aug. 2007.

[29] W. Li, Z. Nie, H. Zhang, C. Paquet, M. Seo, P. Garstecki, and E. Kumacheva, "Screening of the effect of surface energy of microchannels on microfluidic emulsification," *Langmuir : the ACS journal of surfaces and colloids*, vol. 23, no. 15, pp. 8010–4, Jul. 2007.

[30] Z. Nie, M. Seo, S. Xu, P. C. Lewis, M. Mok, E. Kumacheva, G. M. Whitesides, P. Garstecki, and H. A. Stone, "Emulsification in a microfluidic flow-focusing device: effect of the viscosities of the liquids," *Microfluidics and Nanofluidics*, vol. 5, no. 5, pp. 585–594, Mar. 2008.

[31] T. Ward, M. Faivre, M. Abkarian, and H. A. Stone, "Microfluidic flow focusing: drop size and scaling in pressure versus flow-rate-driven pumping," *Electrophoresis*, vol. 26, no. 19, pp. 3716–24, Oct. 2005.

[32] L. Yobas, S. Martens, W.-L. Ong, and N. Ranganathan, "High-performance flow-focusing geometry for spontaneous generation of monodispersed droplets," *Lab on a chip*, vol. 6, no. 8, pp. 1073–9, Aug. 2006.

[33] W.-L. Ong, J. Hua, B. Zhang, T.-Y. Teo, J. Zhuo, N.-T. Nguyen, N. Ranganathan, and L. Yobas, "Experimental and computational analysis of droplet formation in a high-performance flow-focusing geometry," *Sensors and Actuators A: Physical*, vol. 138, no. 1, pp. 203–212, Jul. 2007.

[34] T. Nisisako and T. Torii, "Microfluidic large-scale integration on a chip for mass production of monodisperse droplets and particles," *Lab on a chip*, vol. 8, no. 2, pp. 287–93, Mar. 2008.

[35] W. Li, E. W. K. Young, M. Seo, Z. Nie, P. Garstecki, C. A. Simmons, and E. Kumacheva, "Simultaneous generation of droplets with different dimensions in parallel integrated microfluidic droplet generators," *Soft Matter*, vol. 4, no. 2, p. 258, Jan. 2008.

[36] M. Hashimoto, S. S. Shevkoplyas, B. Zasońska, T. Szymborski, P. Garstecki, and G. M. Whitesides, "Formation of bubbles and droplets in parallel, coupled flow-focusing geometries," *Small (Weinheim an der Bergstrasse, Germany)*, vol. 4, no. 10, pp. 1795–805, Oct. 2008.

[37] T. Thorsen, R. W. Roberts, F. H. Arnold, and S. R. Quake, "Dynamic Pattern Formation in a Vesicle-Generating Microfluidic Device," *Physical Review Letters*, vol. 86, no. 18, pp. 4163–4166, Apr. 2001.

[38] P. Guillot and A. Colin, "Stability of parallel flows in a microchannel after a T junction," *Physical review. E, Statistical, nonlinear, and soft matter physics*, vol. 72, no. 6 Pt 2, p. 066301, Dec. 2005.

[39] R. B. Fair, "Digital microfluidics: is a true lab-on-a-chip possible?," *Microfluidics and Nanofluidics*, vol. 3, no. 3, pp. 245–281, Mar. 2007.

[40] A. R. Abate, D. Lee, T. Do, C. Holtze, and D. A. Weitz, "Glass coating for PDMS microfluidic channels by sol-gel methods," *Lab on a chip*, vol. 8, no. 4, pp. 516–8, Apr. 2008.

[41] J. Boyd, C. Parkinson, and P. Sherman, "Factors affecting emulsion stability, and the HLB concept," *Journal of Colloid and Interface Science*, vol. 41, no. 2, pp. 359–370, Nov. 1972.

[42] J. H. Xu, G. S. Luo, S. W. Li, and G. G. Chen, "Shear force induced monodisperse droplet formation in a microfluidic device by controlling wetting properties," *Lab on a chip*, vol. 6, no. 1, pp. 131–6, Jan. 2006.

[43] Y. Zhao, G. Chen, and Q. Yuan, "Liquid-liquid two-phase flow patterns in a rectangular microchannel," *AIChE Journal*, vol. 52, no. 12, pp. 4052–4060, Dec. 2006.

[44] K. Wang, Y. C. Lu, J. H. Xu, and G. S. Luo, "Determination of dynamic interfacial tension and its effect on droplet formation in the T-shaped microdispersion process," *Langmuir : the ACS journal of surfaces and colloids*, vol. 25, no. 4, pp. 2153–8, Mar. 2009.

[45] J. H. Xu, S. W. Li, J. Tan, Y. J. Wang, and G. S. Luo, "Preparation of highly monodisperse droplet in a T-junction microfluidic device," *AIChE Journal*, vol. 52, no. 9, pp. 3005–3010, Sep. 2006.

[46] Y. Zeng, R. Novak, J. Shuga, M. T. Smith, and R. A. Mathies, "High-performance single cell genetic analysis using microfluidic emulsion generator arrays," *Analytical chemistry*, vol. 82, no. 8, pp. 3183–90, Apr. 2010.

[47] K. C. van Dijke, G. Veldhuis, K. Schroën, and R. M. Boom, "Simultaneous formation of many droplets in a single microfluidic droplet formation unit," *AIChE Journal*, vol. 56, no. 3, pp. 833–836.

[48] K. C. van Dijke, K. Schroën, A. van der Padt, and R. Boom, "EDGE emulsification for food-grade dispersions," *Journal of Food Engineering*, vol. 97, no. 3, pp. 348–354, Apr. 2010.

[49] H. Gu, M. H. G. Duits, and F. Mugele, "A hybrid microfluidic chip with electrowetting functionality using ultraviolet (UV)-curable polymer," *Lab on a chip*, vol. 10, no. 12, pp. 1550–6, Jun. 2010.

[50] H. Gu, F. Malloggi, S. A. Vanapalli, and F. Mugele, "Electrowetting-enhanced microfluidic device for drop generation," *Applied Physics Letters*, vol. 93, no. 18, p. 183507, Nov. 2008.

[51] H. Kim, D. Luo, D. Link, D. A. Weitz, M. Marquez, and Z. Cheng, "Controlled production of emulsion drops using an electric field in a flow-focusing microfluidic device," *Applied Physics Letters*, vol. 91, no. 13, p. 133106, Sep. 2007.

[52] S. H. Tan, B. Semin, F. Maes, and J. Baret, "ELECTRIC CONTROL IN DROPLET-BASED MICROFLUIDICS," in *MicroTAS*, 2012, pp. 1486–1488.

[53] S. Shinwary, C. Y. Ching, and P. R. Selvaganapathy, "MONODISPERSE DROPLET GENERATION USING ELECTRICAL PULSES," in *MicroTAS*, 2012, pp. 1522–1524.

[54] A. R. Abate, M. B. Romanowsky, J. J. Agresti, and D. A. Weitz, "Valve-based flow focusing for drop formation," *Applied Physics Letters*, vol. 94, no. 2, p. 023503, Jan. 2009.

[55] S. M. S. Murshed, S. H. Tan, N. T. Nguyen, T. N. Wong, and L. Yobas, "Microdroplet formation of water and nanofluids in heat-induced microfluidic T-junction," *Microfluidics and Nanofluidics*, vol. 6, no. 2, pp. 253–259, Jul. 2008.

[56] P. Garstecki, M. J. Fuerstman, H. A. Stone, and G. M. Whitesides, "Formation of droplets and bubbles in a microfluidic T-junction-scaling and mechanism of break-up," *Lab on a chip*, vol. 6, no. 3, pp. 437–46, Mar. 2006.

[57] K. van Dijke, G. Veldhuis, K. Schroën, and R. Boom, "Parallelized edge-based droplet generation (EDGE) devices," *Lab on a chip*, vol. 9, no. 19, pp. 2824–30, Oct. 2009.

[58] G. K. Youngren and A. Acrivos, "Stokes flow past a particle of arbitrary shape: a numerical method of solution," *Journal of Fluid Mechanics*, vol. 69, no. 02, p. 377, Mar. 2006.

[59] G. S. Wright, P. T. Krein, and J. C. Chato, "Self-consistent modeling of the electrohydrodynamics of a conductive meniscus," *IEEE Transactions on Industry Applications*, vol. 31, no. 4, pp. 768–777, 1995.

[60] R.-Y. Chen, "Flow in the Entrance Region at Low Reynolds Numbers," *Journal of Fluids Engineering*, vol. 95, no. 1, p. 153, Mar. 1973.

[61] S. S. Syed, "Design & Analysis of Microfluidic Systems for Droplet Generation via Flow Focusing & Electrogeneration," McMaster University, 2012.

[62] A. Bazylak, J. Heinrich, N. Djilali, and D. Sinton, "Liquid water transport between graphite paper and a solid surface," *Journal of Power Sources*, vol. 185, no. 2, pp. 1147–1153, 2008.

[63] Y. Xia and G. M. Whitesides, "SOFT LITHOGRAPHY," *Annual review of materials science*, vol. 16, no. 12, pp. 2772–8.

[64] L. Pawlowski, *The Science and Engineering of Thermal Spray Coatings*, 2nd ed. Sussex，England: John Wiley & Sons Ltd, 2008, pp. 67–106.

[65] Y. Kim and H. S. Ko, "Journal of the Korean Physical Society," *Journal of the Korean Physical Society*, vol. 51, pp. 42–46.

[66] M. K. Mulligan and J. P. Rothstein, "Scale-up and control of droplet production in coupled microfluidic flow-focusing geometries," *Microfluidics and Nanofluidics*, vol. 13, no. 1, pp. 65–73, Feb. 2012.

Appendix A: Device Fabrication

1. SU-8 Mold Fabrication

1. Wash silicon wafer in acetone solution for one minute
2. Methanol wash and blow dry with nitrogen
3. Place wafer in plasma etcher at 50Watt for 1 minute
4. Spin Su8-2075 photoresist on the wafer at 500 rpm for 20 second
5. Ramp up the speed to 1500 rpm at an acceleration of 100 rpm/s and spin at final speed for 30 second
6. Prebake the wafer at 65 ℃ for 15 minutes
7. Increase the pre-baking temperature to 95 ℃ in 3 minutes
8. Bake the wafer at 95 ℃ for the period of 30 minutes
9. Align the wafer and mask on mask aligner
10. Expose the wafer to UV light for a total exposure energy of 260 mJ/cm^2
11. Post bake at 65 ℃ for 1 minute
12. Increase post bake temperature to 95 ℃ and maintain the temperature for 12 minutes
13. Submerge wafer into developer solution and slowly stir until the features are clear
14. Isopropyl alcohol check for complete removal of unexposed photoresist
15. Re-submerge wafer back in developer solution if white residual appears
16. DI water rinse and blow dry with nitrogen
17. Hard bake at 120 ℃ for 10 minutes

2. Channel Replica

1. Manually mix base to curing agent of PDMS at ratio 10:1 for 10 minutes
2. Degas PDMS liquid in vacuum chamber for 10 minutes
3. Cut 1 cm segment of silicone tubing (ID = 1.6 mm) and place that onto SU8 mold
4. Pour PDMS liquid onto SU8 mold
5. Bake at 80 ℃ on hotplate for 2 hours
6. Peel PDMS channel off and use 1.5 mm hole puncher (Harris Inc.) to clean the PDMS pieces in the silicone tubing

3. Electrode Fabrication

1. Wash glass slide in acetone solution for one minute
2. Methanol wash and blow dry with nitrogen
3. Spin S1808 photoresist on the glass slide at 3000 rpm for 30 seconds
4. Prebake the glass slide at 95 ℃ for 3 minutes
5. Align the glass slide and mask on mask aligner
6. Expose the glass slide to UV light for a total exposure energy of 150 mJ/cm^2
7. Submerge glass slide into toluene solution for 6 minutes
8. Prebake the glass slide at 95 ℃ for 45 seconds
9. Submerge glass slide into MF-319 solution and slowly stir until the features are clear
10. Wash glass slide in DI water
11. Hard bake the glass slide at 120 ℃
12. Put the glass slide into sputtering machine
13. Deposit 5 nm Cr onto the glass slide
14. Deposit 200 nm Au onto the glass slide

15. Submerge glass slide into acetone solution to lift off the photoresist

4. Capillary Process

1. Use SGT cutter to cut 4.5cm long capillary
2. Use lighter to burn and remove the polymer coating of capillary on both ends
3. Examine the capillaries under microscope and select capillary with smooth surfaces
4. Submerge capillary into Rain-X for 30 minutes

5. Device Assembly

1. Place glass slide and PDMS channel in plasma etcher for 2 minutes to bond them
2. Insert the capillaries into the grooves on PDMS channel and align them under microscope
3. Use liquid PDMS to seal the grooves
4. Insert the other end of microcapillaries into glass-tubing with 0.2 mm ID and seal them use epoxy glue
5. Inject Rain-X into the channel and leave the device overnight for coating Rain-X

Appendix B: Modelling Process of Comsol Simulation

1. Simulation Steps for Model in Chapter 3

Initiation:

Select 3D space, Electrostatics model of AC/DC Module and Stationary Studies

Modelling:

- **Geometry:**

Set dimension as "μm"

Channel: Set a large solid block with dimensions of $1650\ \mu m\ (W) \times 1500\ \mu m\ (L) \times 150 \mu m\ (H)$ with the corner at the position X = 0, Y = 0, Z = 0. The direction is (x, y, z) = (0, 0, 1). This mimics the oil channel.

Capillaries: Set three (five) cylinders with dimensions of $50 \mu m$ in radius and $250\ \mu m$ in length. The positions are: 1. X = 225 μm, Y = 0, Z = 75 μm. 2. X = 825 μm, Y = 0, Z = 75 μm. 3. X = 1425 μm, Y = 0, Z = 75 μm. (4. X = 525 μm, Y = 0, Z = 75 μm. 5. X = 1125 μm, Y = 0, Z = 75 μm.). All the directions are the same, which is (x, y, z) = (0, 1, 0).

Electrodes: Set an X-Y work plane at Z = 0. Draw two rectangles with $1650\ \mu m\ (L) \times 250\ \mu m\ (W)$ at X = 0, Y = 0 and X = 0, Y = 1250 μm to mimic two planar electrodes.

Set geometry as block minus cylinders then form a union.

- **Materials:**

Define material "paraffin oil" with density of 845 kg/m^3 and relative permittivity $\varepsilon = 2.2$. Fill the material in the domain.

- **Electrostatic:**

Assumptions: Charge conservation is set for the entire domain.

Boundary Conditions:

For simulating the point to plane electrode configuration: the Dirichlet boundary conditions are applied to the cross-section of the capillaries and the rectangle E2 (**Figure A. 1A**). The potential at E2 is set to 0 V. Three potentials (300 V, 600 V and 900 V) are applied to the cross-section of the capillaries and the results of these three situations are evaluated.

For simulating the parallel electrode configuration: the Dirichlet boundary conditions are applied to the cross-section of the capillaries, the rectangle E1 and the rectangle E2 (**Figure A. 1B**). The potential at E2 is set to 0 V. Three potentials (300 V, 600 V and 900 V) are applied to the cross-section of the capillaries as well as the rectangle E1 and the results of these three situations are evaluated.

The Neumann boundary condition is applied to all other surfaces and the potential gradient is set to zero.

Initial Values: Set V = 0 for the domain

Meshing: Choose free tetrahedral and set the size as extremely fine

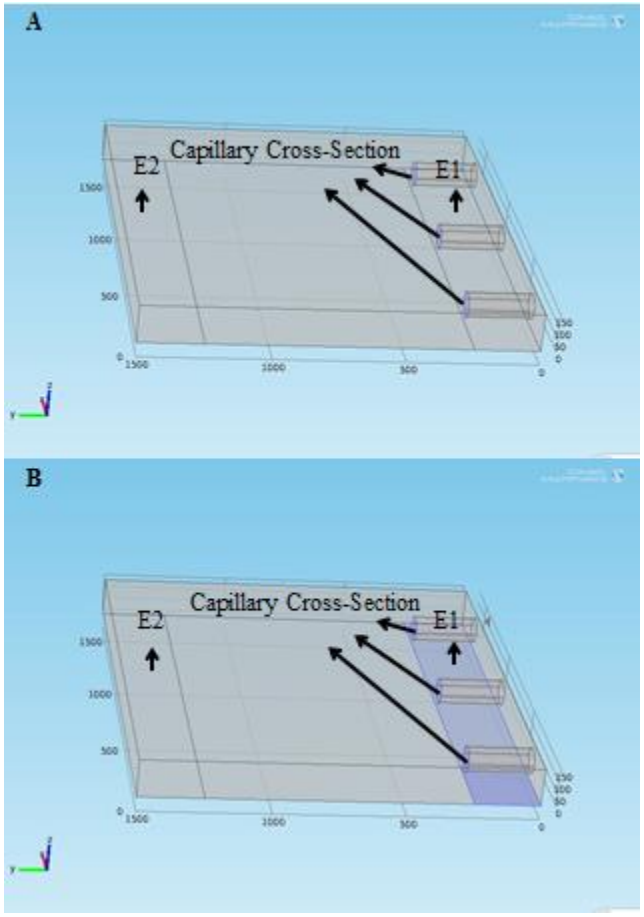

Figure A. 1: *A) Potential boundary condition for the point to plane electrode configuration; B) Potential boundary condition for the parallel electrode configuration*

Post-Processing:

Cut a plane at Z = 75 μm and plot electric field arrow surface.

Select the central point of the capillaries cross-section and plot the electric field intensity.

2. Simulation Steps for Model in Chapter 5

The simulation for chapter 5 is similar to chapter 3 except in the following aspects:

- **Geometry:**

In this part, besides all the geometries set in the previous simulation, the spheres are added to mimic the droplet.

Droplets:

Spheres with diameters R (ranging from 10 μm to 50 μm) are set at the positions of: 1. X = 225 μm, Y = 250 + R μm, Z = 75 μm. 2. X = 825 μm, Y = 250 + R μm, Z = 75 μm. 3. X = 1425 μm, Y = 250 + R μm, Z = 75 μm. (4. X = 525 μm, Y = 250 + R μm, Z = 75 μm. 5. X = 1125 μm, Y = 250 + R μm, Z = 75 μm.)

The Y position is set as 250 + R μm to mimic the detaching moment of the droplet.

- **Electrostatic:**

Boundary Conditions:

For simulating the parallel electrode configuration: the Dirichlet boundary conditions are applied to the surface of the spheres, the rectangle E1 and the rectangle E2. The potential at E2 is set to 0 V (**Figure A. 2)**.

The Neumann boundary condition is applied to all other surfaces and the potential gradient is set to zero.

Post-Processing:

Select the tip point of the spheres and obtain the electric field intensity.

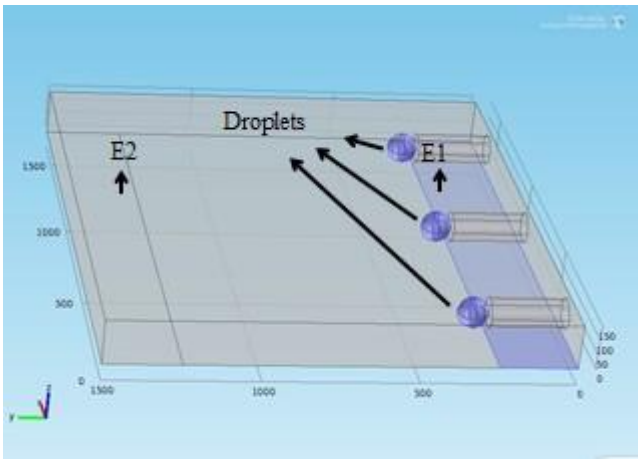

Figure A. 2: *Potential boundary condition of the model in chapter 5*

Appendix C: Test of Mesh Dependence of Comsol Simulation

When simulating the physics model in this research, it is important to ensure that the solution does not depend on the mesh size. In this appendix, three sizes of mesh are applied in the simulation model to investigate their influence to the simulation results.

Due to the similarity of the models in chapter 3 and chapter 5, test either one model should be enough to demonstrate the influence of mesh size. The device with parallel electrode configuration and five-capillary in chapter 3 is selected to do the mesh size dependence test.

The coarsest mesh size is with maximum element size of 33 μm and the minimum element size of 0.33 μm. The number of elements is 296929. The finer mesh size is with maximum element size of 26.5 μm and the minimum element size of 0.33 μm. The number of elements is 408438. The finest mesh size is with maximum element size of 20 μm and the minimum element size of 0.33 μm. The number of elements is 812808. The electric field intensity at the central point of each capillary at three mesh sizes is plotted in **Figure A. 3.** As the number of mesh element increases (mesh size decreases), the electric field intensity remains constant. To further investigate the mesh dependence of the simulation, the electric field distribution at central plane of the device at three mesh sizes is plotted in **Figure A. 4**. The electric field distributions under three mesh sizes are the same, which further demonstrate the mesh independence of our simulation.

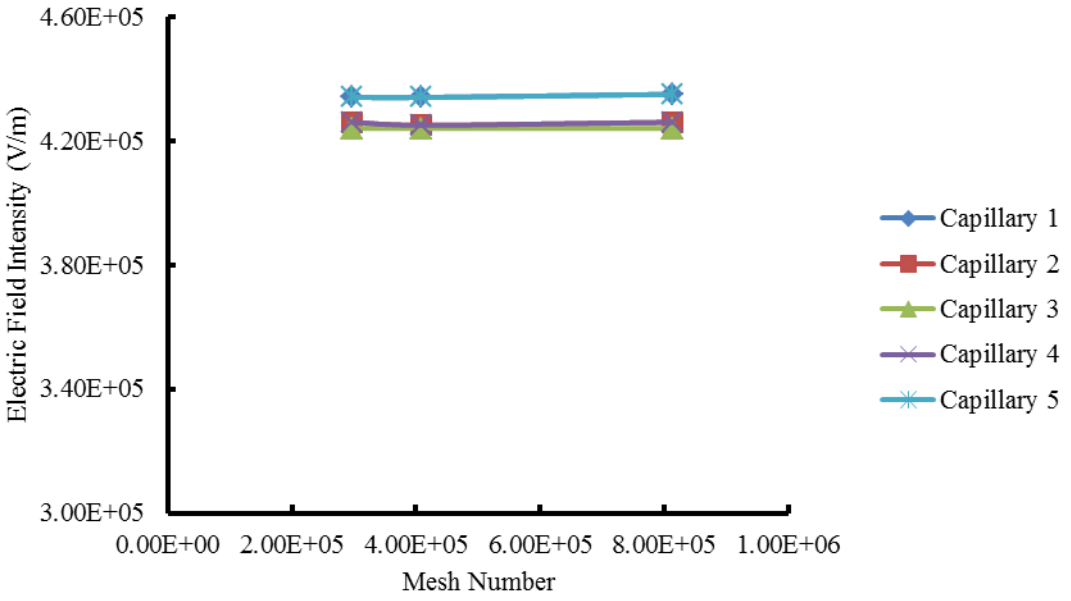

Figure A. 3: *Electric field intensity at the center of the capillary vs. mesh number at 300 V*

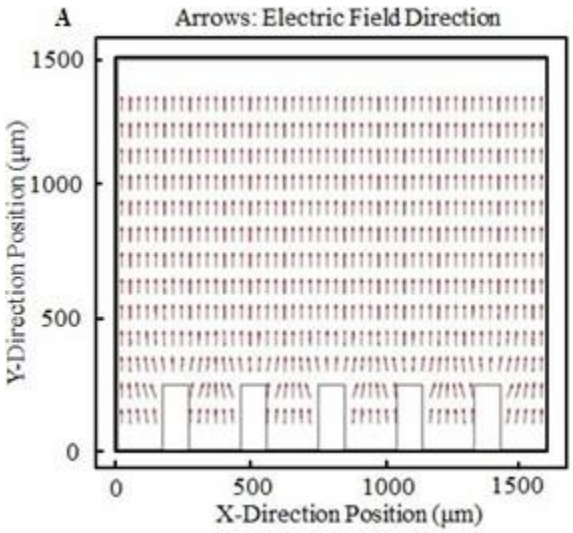

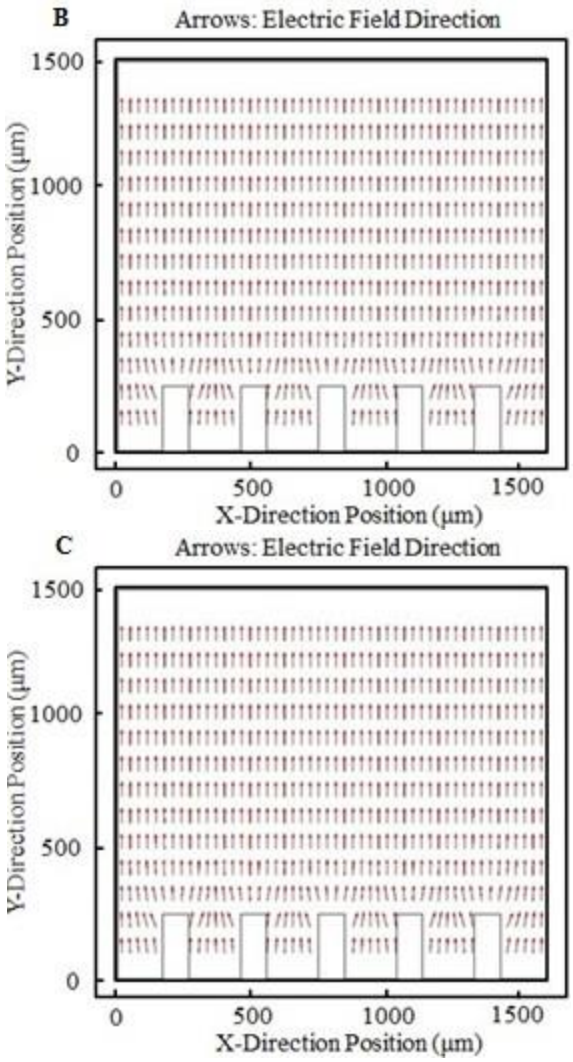

Figure A. 4: *Electric field distribution at central plane of the device at: A) Coarsest mesh; B) Finer mesh; C) Finest mesh*

Appendix D: Test of Geometry Dependence of Comsol Simulation

In the simulation of our research, the simulating geometries length is set to 1500 µm. However, is the length of the simulating geometry affect the simulation results? To address this question, the simulations were done on the three lengths of geometry (1500 µm, 2000 µm and 3000 µm). The device with three capillaries was simulated at point to plane electrode configuration with the potential of 300 V.

Figure A. 5 shows the simulation results of electric field intensity at three capillaries in three different channel lengths. It shows that there are almost no differences in electric field intensities at different capillaries in different channel lengths.

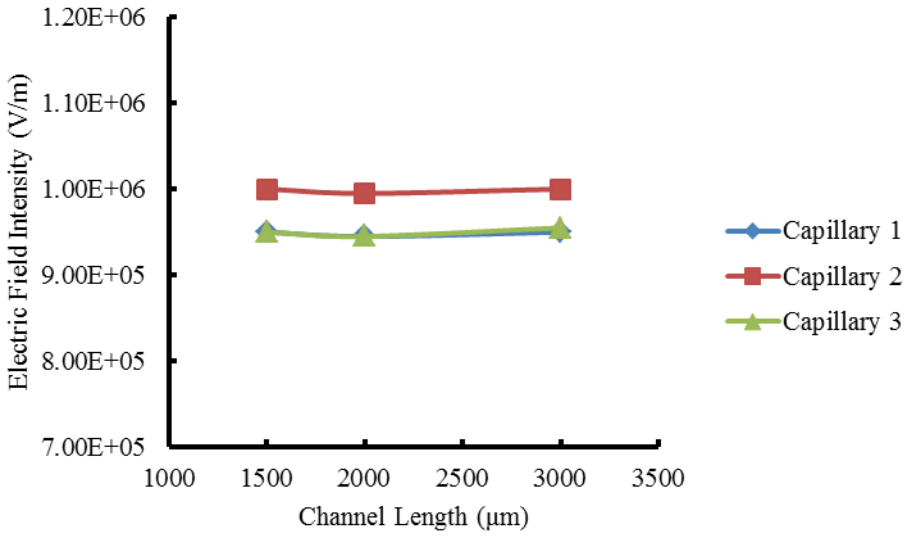

Figure A. 5: *Electric field intensity at the center of the capillary of three capillaries under different channel length*

To further demonstrate the geometry independence, the electric field distributions are illustrated in **Figure A. 6**. **Figure A. 6A** shows the electric field distribution in the simulating geometry with the length of 1500 μm, **Figure A. 6B** shows the simulation result of the 2000 μm long device and **Figure A. 6C** shows the simulation results of the 2000 μm long device. The similarity of the electric field distributions in three geometries further justifies that the simulating results do not depend on the length of the geometry, further validating our simulation

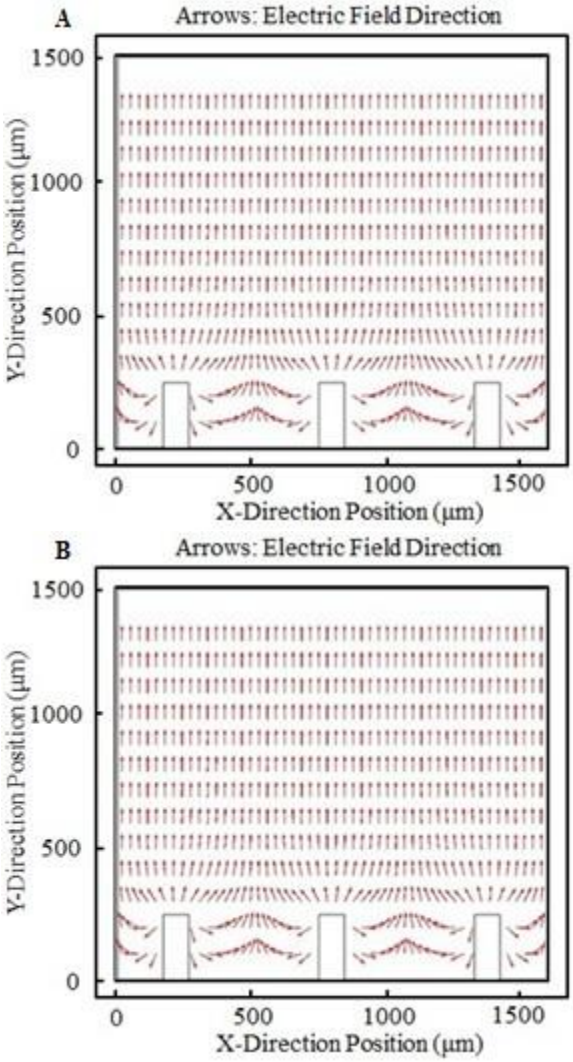

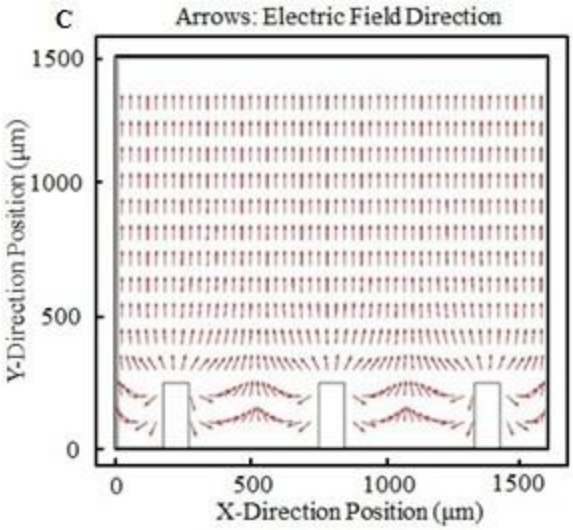

Figure A. 6: *Electric field distribution in: A) the 1500* ***µm*** *device; B) the 2000* ***µm*** *device; C) the 3000* ***µm*** *device*